The Fundamental Electrochemical Characteristics of Rare-Earth Cluster-Based Metal–Organic Frameworks

Lars Miller

A Thesis in

The Department of

Chemistry and Biochemistry

Presented in Partial Fulfillment of the Requirements for

The Degree of Master of Science (Chemistry) at

Concordia University

Montréal, Quebec, Canada

December 2022

CONCORDIA UNIVERSITY

School of Graduate Studies

This is to certify that the thesis prepared

By: Lars Miller

Entitled: The Fundamental Electrochemical Characteristics of Rare-Earth Cluster-Based Metal–Organic Frameworks

And submitted in partial fulfillment of the requirements for the degree of

Master of Science (Chemistry)

complies with the regulations of the University and meets the accepted standards with respect to originality and quality.

Signed by the Final Examining Committee:

Dr. Rafik Naccache	_____	Chair
Dr. Marek Majewski	_____	Examiner
Dr. Xavier Ottenwaelder	_____	Examiner
Dr. Ashlee Howarth	_____	Supervisor

Approved by _____

Dr. Paul Joyce, Chair, Department of Chemistry and Biochemistry

14 December 2022 _____

Dr. Pascale Sicotte, Dean, Faculty of Arts and Sciences

Abstract

The Fundamental Electrochemical Characteristics of Rare-Earth Cluster-Based Metal–Organic Frameworks

Lars Miller

This work explores the synthesis and characterization of redox active rare-earth (RE) metal–organic frameworks (MOFs). MOFs are of interest due to their unique properties including permanent porosity, high surface area, and stability. Redox active MOFs have shown promise in a variety of applications including catalysis and molecular electronics.

The second chapter will explore materials composed of Ce(IV) clusters bridged by ditopic carboxylate-based linkers. The synthesis of a series of UiO-66 analogues using the redox active metal Ce(IV) is completed with the original linker benzene-1,4-dicarboxylic acid as well as with various functionalized linkers including: 2-aminobenzene-1,4-dicarboxylic acid, 2-fluorobenzene-1,4-dicarboxylic acid, 2-bromobenzene-1,4-dicarboxylic acid, 2,5-dihydroxybenzene-1,4-dicarboxylic acid, and 2,3,5,6-tetrafluorobenzene-1,4-dicarboxylic acid. The electrochemical differences between the analogues is explored via cyclic voltammetry.

The third chapter delves into the synthesis of a series of redox active MOFs using the tetratopic tetrathiaflvalene-3,4,5,6-tetrakis(4-benzoic acid) (TTFTBA) redox active linker. Synthesis of a 3D cluster based MOF is attempted using Ce(III/IV), Yb(III), and Lu(III). Two new MOFs with **shp** topology are synthesized using TTFTBA and Yb(III) or Lu(III). The materials are characterized, and their redox properties are explored.

Acknowledgements

Firstly, I would like to thank my parents for their financial support, due to low wages, international tuition, and a crumbling global capitalist system without this support my research would not be completed. I would also like to thank them, my grandparents, and my brother and sister for their moral and emotional support. It is with their support and my friends abroad and that I have made in Montréal my mental health has remained as stable and healthy as possible. I want to thank the chaotic series of roommates I have had here, most notably the last one Yehuda who opened his home to me when I truly was lost for options.

I would also like to thank my lab colleagues for the friendships that I have built throughout my degree and the support they have offered me. My mentor Paola for teaching me enough about MOFs to enjoy a running start in my research and for explaining and walking me through the Concordia bureaucracy and showing to me all that Montréal has to offer. Zvart for what I am sure will be a lifelong friendship no matter where we end up and I know that if I am up to no-good I know Zvart will always be down to join. Amna I would like to thank for being my first friend at Concordia, for always joining me on adventures, whether boring or eventful and for listening to endless rants. I will always remember when we ate 6 $1 croissants in one day, and how I enjoy leading her around. Her support of me has been truly moving and my self-esteem would be significantly lower were she not around. Not only has she been a friend outside the lab, but her support for me in the lab has been incredible, from running DRIFTS samples and PXRD to sending me soo many NMRs because I was too lazy to use the VPN, for all this I thank her and wish that she receives the world. Hudson I would like to thank for showing me the gay side of Montréal and always offering an open ear to discuss my research. Rafa, I want to thank for his constant support, even from thousands of kilometers away, spending late nights on Zoom, helping me understand a software that neither of us could understand, and for always offering a knowledgeable response to every random question I could throw at him. Victor, I crown the king of RE MOFs, your support is truly unbounded and relentless, I know that wherever I go he will have my back and he should know that wherever he ends up I will have his too. His queries and interest in my work has always forced me to think more than I wanted, and for that I owe so much. Samantha for her help I am so grateful, the witty banter we shared and all the laughter always brings me joy, and her support with

my research will not be underwritten. Ximena and I, we learned to have more patience together, the difficulty we shared shall not be forgotten, and I will always enjoy the candor in our friendship. Chris has MacGyver skills and for that I owe him a lot, for rescuing my BET and DRIFTS and even helping with my passport problems. He really is a man with a plan. Rehmat I want to thank her for her caring words, her support with my research and the pain that electrochemistry causes is always lessened by you. Zujhar taught me echem and for that I will never forgive him. With his support and infuriating knowledge, I will always be grateful and jealous. Joey too, without his support in the past few months and our shared fury at the potentiostat I will remember and thank him for the help. To whomever is reading this I also would like to say that without these last two I would have no electrochemical data, electrochemistry is not for the fainthearted and with these twos support on painful days I maintained sane, also thank you for reading. Laure-Anne my newest friend, our similarities are uncanny and her support has made me a happier person every time I have seen her. Lavinia I knew for the shortest length of time, but her impact on my research and the friendship is huge. I will always remember the joy we had discussing literally anything. The penultimate thank you I give to Hatem, without his instruments, and hands-on support my resume would be much weaker. Not only that but he offered me a new perspective on reality and a friendship I hope to never let die. My final thank you is to my advisor, Ashlee. She always offered me lively and interesting discussion, offering a pragmatic perspective and optimistic solution to my difficulties.

Contribution of Authors

In all chapters, Ashlee J. Howarth acted in a supervisory role. In Chapter 2 Dr. Marek Majewski and Dr. Xavier Ottenwaelder acted in an advisory role with regards to performing and understanding the electrochemistry measurements.

In Chapter 2, thermogravimetric analysis was performed by Lavinia A. Trifoi and P. Rafael Donnarumma, scanning electron microscopy micrographs were collected by Samantha Prelaz, and some diffuse reflectance infrared Fourier transform spectroscopy were collected by Amna Muhammad. Powder X-ray diffraction diffractograms were collected at the McGill Chemistry Characterization Facility with the help of Dr. Hatem M. Titi.

In Chapter 3, diffuse reflectance infrared Fourier transform spectroscopy was performed by Amna Muhammad and inductively coupled plasma mass spectrometry was performed by Dr. Heng Jiang at the Concordia University Center for Biological Applications of Mass Spectrometry. Some powder X-ray diffraction diffractograms were collected at the McGill Chemistry Characterization Facility with the help of Dr. Hatem M. Titi.

Table of Contents

List of Figures

List of Tables

List of Schemes

List of Equations

List of Abbreviations

1D	one-dimensional
2D	two-dimensional
BDC	benzene-1,4-dicarboxylic acid
BET	Brunauer-Emmett-Teller
BPDC	biphenyl-4,4'-dicarboxylic acid
BPyDC	2,5'-bipyridine-5,5'-dicarboxylic acid
BrBDC	2-bromo-1,4-dicarboxylic acid
CV	cyclic voltammetry
d	diameter
DCM	dichloromethane
DFBA	2,6-difluorobenzoic acid
DMF	N-N'-dimethylformamide
DMSO	dimethyl sulfoxide
DMSO-d6	deuterated dimethyl sulfoxide
DOBDC	2,5-dihydroxybenzene-1,4-dicarbocylic acid
DRIFTS	diffuse reflectance infrared Fourier transform spectroscopy
F_4BDC	2,3,5,6-tetrafluorobenzene-1,4-dicarboxylic acid
FBA	2-fluorobenzoic acid
FBDC	2-fluorobenzene-1,4-dicarboxylic acid
fcu	face centered cubic
FTO	fluorine doped tin oxide
IR	infrared
IUPAC	International Union of Pure and Applied Chemistry
Me-TTFTBA	tetrathiafulvalene-3,4,5,6-tetrakis(2-methly-4-benzoic acid)
MOFs	metal–organic frameworks
NH_2BDC	2-aminobenzene-1,4-dicarboxylic acid
NMR	nuclear magnetic resonance

PXRD	powder X-ray diffraction
RCSR	Reticular Chemistry Structure Resource
SALE	solvent assisted linker exchange
SALI	solvent assisted linker incorporation
SBU	secondary building unit
SCE	saturated calomel electrode
SCXRD	single crystal X-ray diffraction
SHE	standard hydrogen electrode
$TBAPF_6$	tetrabutylammonium hexafluorophosphate
TEMPO	(2,2,6,6-tetramethylpiperidin-1-yl)oxyl
TFA	trifluoroacetic acid
THF	tetrahydrofuran
TTF	tetrathiafulvalene
TTFTB	tetrathiafulvalene-3,4,5,6-tetrakis(4-benzoate)
TTFTBA	tetrathiafulvalene-3,4,5,6-tetrakis(4-benzoic acid)

Chapter 1

Introduction

1.1. Metal–Organic Frameworks

The use of chemistry to increase the quality of life for humans has been occurring for thousands of years. Modern archaeologists and anthropologists in South Africa have uncovered evidence of humans from the African Stone Age processing earth containing iron oxides for apparently symbolic uses.[1] This 75,000-100,000-year-old evidence of chemical processing provides evidence to the statement that human development and chemical evolution have grown together.[1,2] In fact, modern human civilization and nearly all the associated luxuries of it (when compared to the middle stone age) are a byproduct of humans' long history in manipulating things we find on our planet through chemical means.[3] As chemistry developed with humans, the field itself grew from simply grinding and heating rocks for dye to studies of modern solid state electrolytes.[2,4] Throughout this massive growth, chemistry has continuously been expanding and eventually began compartmentalizing into fields. The separation of chemistry into varying and often overlapping fields has more recently grown to include metal–organic frameworks (MOFs).[5] As the name suggests, MOF research occurs in the overlap between inorganic chemistry and organic chemistry. The study of MOFs is a relatively new field when compared to the chemistry timeline, and is growing rapidly.[5,6]

The idea of synthesizing MOFs was first described by Kinoshita *et al.* in 1959 who published the crystal structures of a coordination polymer with polyacrylonitrile and Cu(I).[7] Though this material was not treated with particularly large notoriety, it is the first published evidence of what would later be described as a MOF, and the field that has been created since. The next publication in MOF history was by E.A. Tomic in 1965, where coordination polymers composed of three different organic compounds each with multiple carboxylic acid functional groups were coordinated to metal ions: Zn(II), Ni(II), Al(III), Fe(III), and Th(IV)).[8] The thermal stability of coordination polymers with these various metal valences and coordination numbers showed the possibility for a huge variety of coordination polymers that could be synthesized in what would later be defined as the MOF field.[8] The first study that would establish MOFs as a

field and call MOFs by that name was by O.M. Yaghi in 1995 when they published the single crystal X-ray diffraction (SCXRD) structure of a copper and 4,4'-bipyrdine MOF.[9] Through these studies the field of MOFs was established, but the structures themselves were not immediately defined.

The International Union of Pure and Applied Chemistry (IUPAC) has defined in 2013 MOFs as a "coordination network of organic ligands containing potential voids", while this definition is decidedly open ended it allows for huge variety in the porosity of the structures depending on conditions and external stimuli.[10] Although this is the official definition of MOFs, the materials themselves can be defined by what they are constructed of; metal nodes, either metal clusters, chains, or ions, and organic linkers, as shown in Figure 1.1. Even without considering the number of potential metal nodes, the infinite number of organic linkers indicates the immense variety of MOFs possible.[5] Accordingly, the Cambridge Crystallographic Data Center MOF data set contains 12 000 MOF structures.[11] This mass quantity of MOFs has further opened the field beyond the synthesis of new MOFs and their applications, and towards computational studies with the application of data science and machine learning.[12,13]

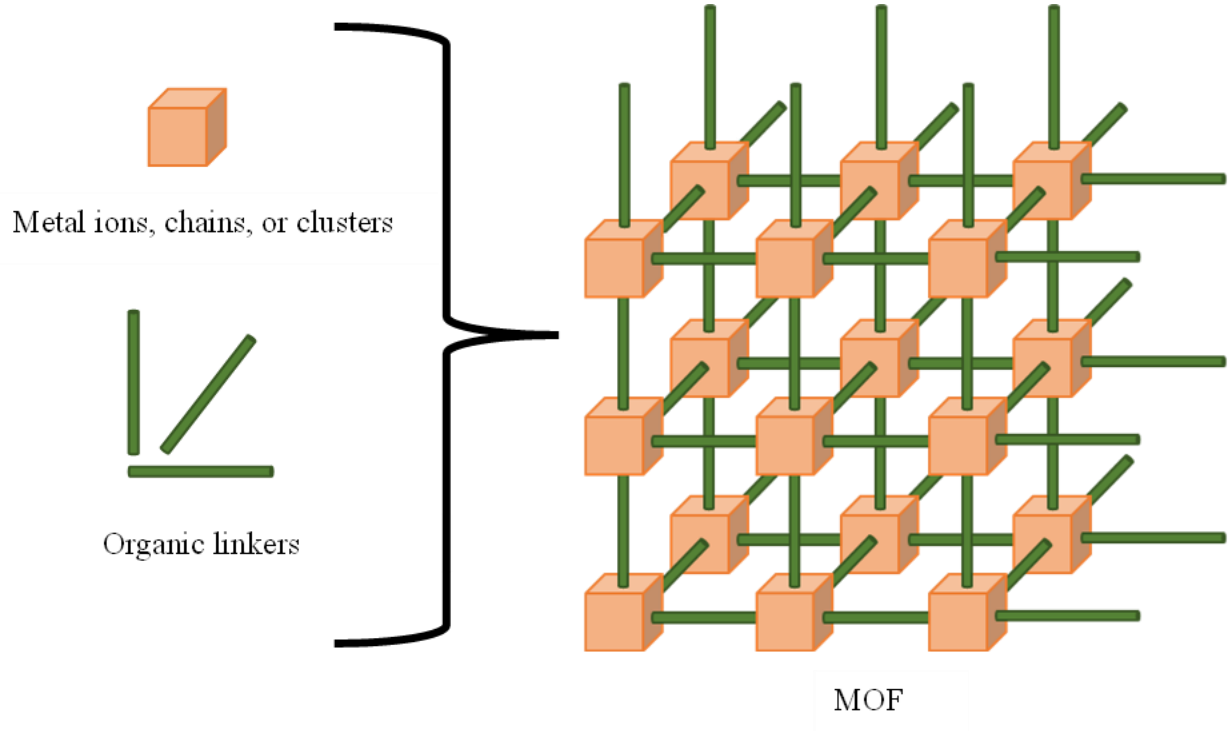

Figure 1.1: Schematic representation of a MOF structure assembly.

It is convenient to think of MOFs from a building block approach, where there are two building blocks, the metal cluster, chains, or ions, and the organic linkers (Figure 1.1). The variety of metal nodes has been envisioned since the original publication by E.A Tomic.[8] MOF synthesis has been explored using *s*-block metal ions from Li(I)[14] to Ba(II);[15] *p*-block metal ions including Al(III)[16] and Bi(III);[17] *d*-block metal ions such as Ti(IV),[18] Zr(IV)[19], and more;[20–23] while *f*-block metal ion MOFs include Ce(III),[24] Ce(IV),[25] and Tm(III)[22] among others.[22,23,26,27] Similarly, E.A. Tomic studied a variety of linkers, this too has been vastly expanded from the initial 3 linkers to a countless number of linkers.[8] Of this expanded catalogue of linkers, one characteristic is consistent for them all, having more than one site for coordination to the metal node. The molecular characteristics for these coordinating groups are varied and include organic anions like carboxylates, sulfonates, phosphonates, and heterocyclic compounds.[28]

1.2. Reticular Chemistry

Reticular chemistry is a synthetic approach for MOFs that is based on the logical design of network structures. The selection of an organic linker and inorganic moiety are determined based on the desired characteristics of the final MOF including the stability, structure, and surface area.[29] Fortunately, a fundamental aspect to reticular chemistry is that you can use different organic linkers and different inorganic units to achieve the same predetermined net.[30] This allows the building of extended crystalline structures using strong bonds.[29,31]

1.3. Topology

Due to the periodic framework structure of MOFs, it is necessary to define the structure of MOFs based on the connectivity of the nodes and the linkers. Practically, to determine the topology of a MOF, the net structure of the MOF is first determined. The connectivity and symmetry of the linkers and the inorganic SBUs form a net architecture.[32,33] Each net can be defined by a specific topology, see Figure 1.2. The name of the topology for a given net is defined and collected by the Reticular Chemistry Structure Resource (RCSR).[32] The topology of a MOF is denoted by a bolded three letter code and is static and does not change based on physical changes to the MOF such as stretching or bending. Only chemical changes or symmetry changes to the metal cluster and/or linker would cause a change in topology.[34] The topological assignments of a MOF could best be

compared to stereochemical assignments in other fields of chemistry. The primary advantage to organizing MOFs by topology is that it allows for a systematic naming/sorting system, and for ease of exploration of new structures through reticular chemistry. Most notable in this thesis are MOFs with the face centered cubic or **fcu,** topology (Figure 1.2) such as UiO-66 and UiO-67 (University of Oslo). While these two MOFs have the same **fcu** topology, they do not have the same linkers. Since they have the same topology, the MOFs are isoreticular and isostructural to each other but with different unit cell sizes.[19]

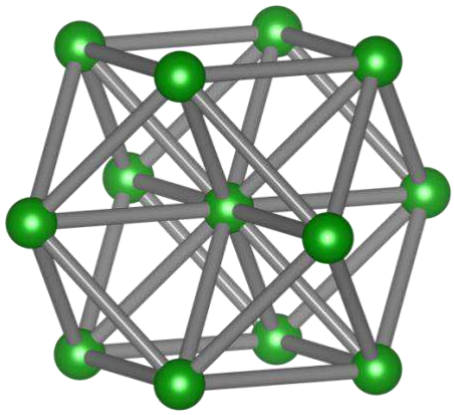

Figure 1.2: Representation of the 12-connected **fcu** net.

1.4. Characteristic Properties

The most noteworthy characteristic of MOFs is their permanent porosity.[5] Depending on the size of the linkers and the metal nodes, as well as the topology, MOF surface areas can vary over a large range and be as high as 7800 m^2/g.[35] MOFs also generally have quite low densities, which have been reported as low as 0.124 g/cm^3.[36] MOFs have wide-ranging thermal, physical, and mechanical stability that can be tuned for a given application and is dictated by a variety of factors including topology, density, and void fraction.[37] Studying MOF stability in general is difficult due to the huge variety of MOFs present and usually yields specific rather than generalized results. For example Moghadam *et al.* compared MOF stability based on linker length vs topology and coordination number, they concluded that longer linkers reduce stability in high coordination environments.[38] In some isostructural MOFs the strength of the metal-oxygen bond has been found to affect the stability of MOF.[39] The stronger metal oxygen bond in Zr(IV)-UiO-66 increases

stability when compared to Y(III)-UiO-66.[22,40] The stability coupled with porosity is the standout characteristic of MOFs and often a key point to their use in various applications.[5]

1.5. Electrochemical Properties

The vast majority of MOFs are insulators because the structure of most MOFs is not favourable for electron transport.[41–44]In 3D MOFs there is no stacking of linkers or metals directly (like in 2D MOFs). Stacking structures increase conductivity by allowing electron transfer between the layers of the molecule through π-π stacking.[43] Since the stacking structure does not typically exist in 3D MOFs, electron transfer would need to easily occur between the metals and the linkers.[43] Thus, the energy levels of the HOMO and LUMO orbitals and the valence band of the metal must be considered. Since the HOMO-LUMO gap of the organic linker is usually larger than 3 eV this decreases the possibility of a metal with valence energy levels that aligns with the linker. If overlap occurs then electrons can travel between the metal and the linker, which would make the material a conductor.[44] Furthermore, typically the symmetry of the valence orbitals is mismatched with that of the linkers.[44] Nonetheless, by varying the different SBUs, MOFs can be tuned in a way that increases the mobility of electrons throughout the structure, increasing the conductivity of the material.[42]

Electronic materials are divided into three general categories: insulators, semiconductors, and conductors. The differences between these are best explained using band theory. A band is defined as a collection of molecular orbitals of very similar energy, which is no longer described as a collection of quantized molecular orbitals but rather as a continuous band of electrons of similar energy.[45,46] This occurs for each collection of molecular orbitals formed between each interacting pair of atomic orbitals, the highest occupied band is described as the valence band.[45,46] The next notable energy level is the Fermi level, the Fermi level is the highest energy level that an electron can occupy at 0 K, and the relationship between electrons and the Fermi level is used to describe the electronic characteristics of a given material and is used very commonly in the study of semiconductors.[45] The distribution of electrons is described by the Fermi-Dirac distribution.[45] Conductive materials have a Fermi level lower than the highest occupied band, while insulators have a Fermi level higher than the highest possible occupied band.[45] The next highest and unoccupied band is referred to as the conduction band.[45,46] The energy required to go from the

valence to conduction band (band gap) and the occupation of the valence band is what determines the electronic characteristics of the material.[45,46] A material with a fully occupied valence band and a large bandgap is defined as an insulator; a partially filled valence band or overlap between the valence band and the conduction band characterizes the material as a conductor.[45,46] The third category, semiconductors, is defined by a small band gap, either small enough that electrons can enter the conduction bond through simply the application of thermal energy or through the doping of heteroatoms into a material to decrease the bandgap.[45,46] MOFs are typically insulators but, due to their intrinsic porosity may be more easily doped then other materials to have more semiconducting or conducting characteristics.[47,48]

To improve the conductivity of a MOF, it is useful to analyze the ways that an electron may move through the material. Five potential pathways for electrons exist in a MOF: *through-bond*¸ *through-space*, *extended conjugation*, *redox hopping*, and *guest-promoted*.[43] The through-bond pathways occur only when the bonding orbital energy of the linker is close to the bonding orbital energy of the metal. The linker and metal then allow for charge mobility through the metal-linker bond, and the geometry of the MOF allows for a long continuous pathways of linker and metal bonds.[43,49] Typically MOFs that exhibit this kind of conductivity are one-dimensional (1D), and have electropositive linkers, with N or S coordinating to the metals.[43,49–51] Through-space pathways occur when the MOF geometry allows for stacking between conjugated linkers. In this π -π stacking motif electrons can then be transferred from one conjugated system to another.[43,52] The most notable MOFs that exhibit this kind of stacking interaction are often two-dimensional (2D) and most relevantly for this thesis contain linkers with the tetrathiafulvalene (TTF) motif, as well as other electron rich linkers such as 7,7',8,8'-tetracyanoquinodimethane.[43,52,53] Extended conjugation pathways allow for electrons to be transferred through an extended conjugated system, the delocalization of electrons in a π-d conjugated system allow for electrons to be transported easily through the organic and inorganic parts of the framework. These electrons are observed to be travelling through the conjugated plane.[43] Conductivity via this pathway can best be compared to electron transport in graphene sheets.[43,54] For a MOF to have electron transport properties via this pathway, the organic linkers need to be bound to the metal by chelating groups such as ortho-diol, diamine, and dithiol which help to create a larger organic-inorganic conjugated system.[43] Commonly found linker and metal combinations in MOFs that use this pathway are period 4

transition metals with dihydroxybenzoquinate joined by alkoxy groups, and period 4 metals and lanthanoids with 2,3,6,7,10,11-hexaoxytriphenylene joined by alkoxy groups.[43,55–58] The redox hopping pathway is generally used to describe electron transport that does not involve guest species, band electron transport as is present in the above pathways, or to explain conductivity in one of the above pathways that continues regardless of defects in the crystalline structure.[43] Physically, redox hopping is described by electrons being transported spatially though small gaps in the structure of the framework. This transport is amplified by the presence of redox active groups or metals present in the framework. This pathway can thus be categorized into three categories: metal-based often containing Cu or mixed metals,[43,59,60] linker-based, and mixed metal-linker based with Cd and trans-4,4'-azobispyridine.[43,61] Most notably for the results presented further in this thesis, the presence of the redox active TTF functional groups and Ce(IV) ions thus increase the ability for redox hopping to occur in the MOF.[62,63] The final electron transport pathway that is possible in MOF materials is via guest promoted transport.[43] This pathway involves the post-synthetic introduction of electroactive guests to the pores and space present inside the MOF. Electrons can travel through these electroactive species by guest-guest interactions or guest-framework interactions.[43] Common guest materials introduced include iodine or polyiodides,[43,64,65] organic and organometallic molecules such as tetracyanoquinodimethane,[43,66,67] and conductive polymers and oxides including polypyrrole and SnO.[43,48,68] Thus, through structural design and/or the introduction of guests into a MOF, these materials have been observed to transport electrons between 2.71 and 2 500 S/cm with the introduction of guest materials.[43,69,70]

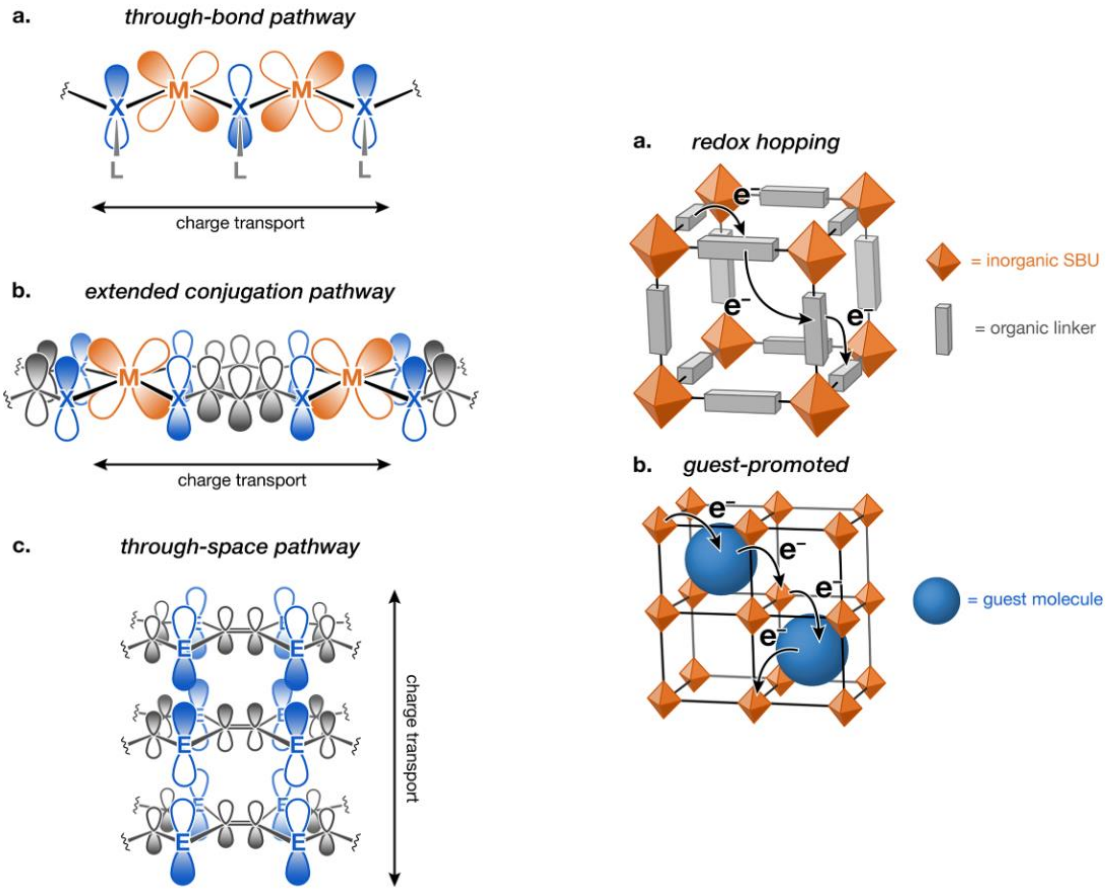

Figure 1.3: Illustrations of various electron conductivity pathways in MOFs. Arrows indicate direction of charge transport. Illustration from Xie *et al.*, with small modifications to maintain clarity.[43]

1.6. Applications

The permanent porosity of MOFs combined with their thermal, physical, and mechanical stability allows for a variety of potential applications for these unique materials.[5] These applications include catalysis,[23,71,72] sensing,[73,74] gas adsorption,[16,18,21] drug delivery,[17,75] energy storage,[14,25,42,70,76–89] bioimaging,[90–92] and wastewater remediation[93,94] among many others.[95–97] Of these various applications the most relevant to this thesis are those of energy storage and catalysis specifically the potential utilization of redox active MOFs.[98,99] Commercial use of MOFs is starting to develop, companies including NuMat Technologies created gas cylinders containing MOFs to safely store dangerous gases, and MOF Technologies developed a product for the controlled

release of anti-ripening agents on fruits transported long distances.[100,101] In addition to companies that are already producing specialized MOF products commercially there are countless start-ups both large and small that have numerous patents for various MOFs and MOF applications.[101]

1.7. Hexanuclear Cluster-Based MOFs

Hexanuclear cluster-based MOFs are a subclass of MOFs that contain an SBU with six metal ions. These metal ions create an octahedral cluster that is bound to the linkers of the framework, which in turn are bound to other hexanuclear clusters to create a MOF. While discrete hexanuclear clusters have been studied and characterized previously,[102] it was not until 2008 when Cavka *et al.* used these clusters to create MOFs.[19] In this case hexanuclear clusters composed of Zr(IV) coordinated to bridging –O and –OH ligands create an SBU of the formula $(Zr_6O_4(OH)_4)^{12+}$. Each Zr(IV) ion is 8 coordinated in a square-antiprismatic geometry to μ_3–O and μ_3–OH groups via an alternating pattern and to the oxygens of 12 CO_2^- groups that are the carboxylates of the linkers.[19] The cluster is shown with the 12 CO_2^- groups in Figure 1.4. In addition to the 12 connected hexanuclear cluster MOFs presented by Cavka *et al.*, which include UiO-66, UiO-67, and UiO-68, other MOFs have been discovered that contain 8-, 6-, and 4-connected hexanuclear clusters as well.[19,103–106] The lower connectivity of the hexanuclear clusters in certain MOFs and the ability to maintain structural stability allows for the presence and utilization of open metal sites in the frameworks, a property of interest for catalysis and ion adsorption.[107,108] In addition to the variation in cluster connectivity when using hexanuclear clusters as MOF building blocks, these clusters can also be obtained with different metals including Y(III), Ce(IV), Tm(III) and more.[22,109]

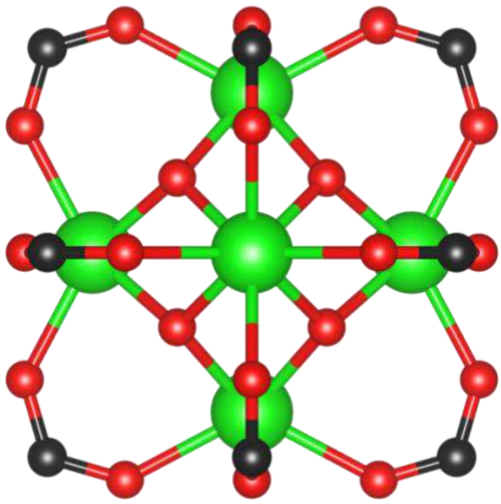

Figure 1.4: Zr(IV) hexanuclear cluster including the bridging CO_2^- groups indicating where carboxylate containing linkers could bond.

1.7.1. UiO-66 and UiO-67

In 2008, researchers at the University of Oslo published evidence of two new MOFs, UiO-66 (Figure 1.5) and UiO-67.[19] These MOFs are composed of hexanuclear Zr(IV)-clusters that are 12 connected by benzene-1,4-dicarboxylic acid (BDC) and biphenyl-4,4'-dicarboxylic acid (BPDC) respectively.[19] Over the last 10 years, these MOFs have become archetypal. Presently a search on Google Scholar for UiO-66 will yield 48 000 results, and more than 7 000 results from 2022 alone. This number and variation in studies is no doubt a result of the high mechanical, thermal, and aqueous stability of the original structure, which has led to incredible diversity in the design of isostructural and isoreticular MOFs with varying linkers and metals, as well as composite materials.[40] The stability of the original UiO-66 and UiO-67 is due to the strength of the Zr(IV)-O bond.[40]

Zr-UiO-66 and UiO-67 are typically synthesized with a solvothermal method in N,N'-dimethylformamide (DMF) using a Zr(IV) salt and the linker.[19] UiO-66 has an **fcu** topology with a surface area of 1 160 m^2/g and containing two different sizes of pores, a tetrahedral pore of 7.5 Å diameter and a 12 Å octahedral pore with a 6 Å aperture, see Figure 1.5.[40,110] While UiO-67 has

a surface area of 2 500 m^2/g with **fcu** topology and two pores, an octahedral pore with a diameter of 23 Å with 7 Å aperture and a tetrahedral pore with a diameter of 11.5 Å.[111,112]

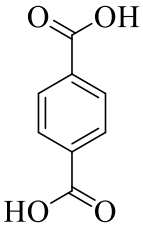

benzene-1,4-dicarboyxlic acid

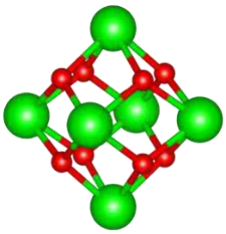

Zr(IV) hexanuclear Cluster

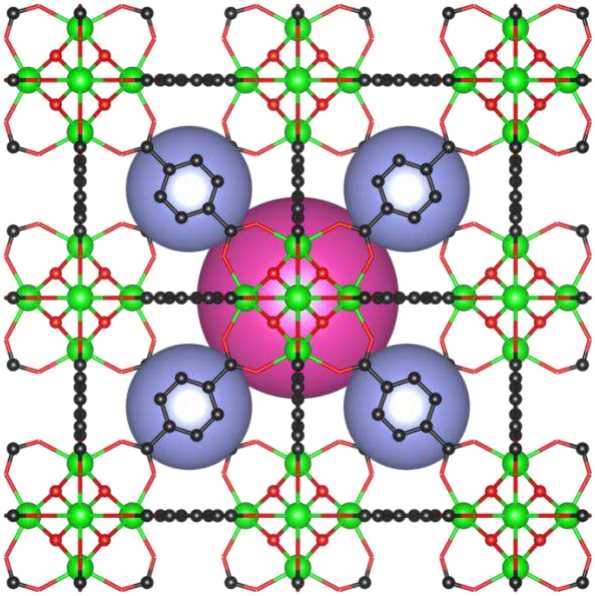

UiO-66

Figure 1.5: The two constituents of UiO-66 and the framework with the pores filled by magenta (octahedral) and lilac (tetrahedral) spheres. Zr is represented by lime spheres, red is O and black is C.

1.7.2. Rare-Earth UiO-66

Rare-earth (RE) metals include the lanthanoids plus yttrium and scandium. These metals, despite their name, are quite commonly found in the earth's crust.[113] Of these RE ions Ce(IV), Y(III), Eu(III), Gd(III), Tb(III), Ho(III), Er(III), Tm(III), and Yb(III) have been used to synthesize MOFs isostructural to UiO-66.[22,109] These metals are commonly found in the +3 oxidation state, and thus the hexanuclear clusters formed by these metals are slightly different from the archetypal Zr(IV)-MOF. While the clusters of Zr(IV)-UiO-66 have the formula $Zr_6O_4(OH)_4(CO_2)_{12}$ the formula for the RE(III) clusters are $[RE_6(OH)_8(CO_2)_{12}]^{2-}$ indicating the increase in hydroxylated oxygens in the cluster and yielding an anionic MOF, thus requiring cations to maintain charge neutrality.[19,22] The exception among the rare-earth series is Ce(IV), which forms Ce(IV) clusters of the same base formula as Zr(IV) and thus not requiring cations to maintain charge neutrality of the resulting MOF.[109] Ce is of particular interest in MOF synthesis and potential applications due

to its redox properties that allow it to exist as Ce(III) or Ce(IV).[109] Furthermore, Ce is also the most abundant of the RE metals making up 0.0046% of the earth's crust by weight, higher then commonly used and studied elements like copper.[114] The redox activity of Ce(IV)/(III) has the potential to be useful in a variety of applications including catalysis and sensing. As one example, Ce(IV) MOFs have been used as catalysts for reactions including the hydroboration of pyridine by Ji *et al.*[115] In this reaction Ce(IV) in Ce(IV)-MOF-808 clusters is reduced using pinacolborane. The reduced Ce(III)-MOF-808 is then oxidized back to Ce(IV) by catalyzing the 1,4 hydroboration of pyridine.[115,116] Generally, the redox catalytic activity of the material can be increased by the increased amount of defects in the material, which increases the amount of open metal sites.[116]

1.7.3. Functionalized UiO-66/67

In addition to modifying the metals in the hexanuclear clusters of UiO-66 and UiO-67, it is also possible to modify the organic linkers present in these archetypal MOFs. Primarily these variations include the functionalization of the phenyl ring, adding heteroatoms to the ring, or expanding the length of the linker. These functional group substitutions of BDC include: 1 and 2 amino groups;[117,118] 1 and 2 bromine atoms;[117] 1 nitro group;[117] 2 hydroxyl groups;[118] 4 fluorine atoms;[118] 1 iodine atom;[119] 2 methyl groups;[117] 1 sodium sulfate group;[119] 2 ethoxy groups;[119] and 1, 2, and 4 carboxylic acid groups among others (Figure 1.6).[118,119] Compared to Zr(IV)-UiO-66, there are far fewer functionalized analogues of RE(III)-UiO-66 reported in the literature. For example, RE(III)-UiO-66 has been synthesized with 2,5-dihydroxybenzene-1,4-carboxylic acid, which has been studied thus far with the metals Y(III), Tb(III), Yb(III), and Eu(III);[120,121] another linker used to synthesize RE UiO-66 is 2-aminobenzene-1,4-dicarboxylic acid.[122] For Ce(IV)-UiO-66 the following linkers have been used: 2-bromobenzene-1,4-dicarboxylic acid (BrBDC),[123] 2-aminobenzene-1,4-dicarboxylic acid (NH_2BDC),[124] 2-fluorobenzene-1,4-dicarboxylic acid (FBDC),[109] 2-methylbenzene-1,4-dicarboxylic acid,[109] 2-chlorobenzene-1,4-dicarboxylic acid,[109] 2-nitrobenzene-1,4-dicarboxylic acid,[109] 2-azidobenzene-1,4-dicarboxylic acid,[125] 2,5-dimethylbenzene-1,4-dicarboxylic acid,[126] 2-hydroxybenzene-1,4-dicarboxylic acid,[124] 2,5-dihydroxybenzene-1,4-dicarboxylic acid (DOBDC),[124] pyridine,-2,5-dicarboxylic acid,[127] and 2,3,5,6-tetrafluorobenzene-1,4-dicarboxylic acid (F_4BDC).[128] Notably, the variations in organic

linkers leads to variations in surface area, stability, synthesis conditions required, and catalytic activity.[123,124]

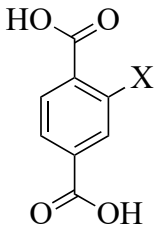

X = NH_2, Br, NO_2, I, $NaSO_3$, and CO_2H

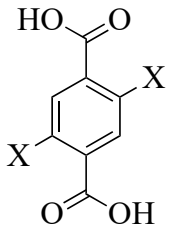

X = NH_2, Br, OH, CH_3, OCH_2CH_3, and CO_2H

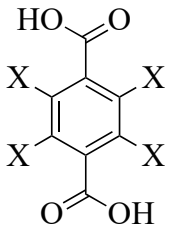

X = F and CO_2H

Figure 1.6: Various functionalized derivatives of BDC used for the synthesis of UiO-66 analogues.

In addition to functionalized analogues of UiO-66, various analogues of UiO-67 have also been studied. For Zr(IV)-UiO-67 this includes the linkers 2,2'-bipyridine-5,5'-dicarboxylic acid (BPyDC) and 2-phenylpyridine-5,4'-dicarboxylic acid.[129] For RE(III)-UiO-67 analogues minimal tuning of the BPDC linker has been reported as RE(III)-UiO-67 was reported only with Dy(III) and Yb(III).[130] Similar is true for the Ce(IV)-UiO-67 which has only been reported with two linkers, BpyDC and BPDCs.[109,116,131]

1.8. Tetrathiafulvalene

In addition to the introduction of redox active metals into MOF clusters like Ce(III)/(IV), redox active linkers have also been introduced.[42] The most notable of these linkers contain the functional group tetrathiafulvalene (TTF), see Figure 1.7.[43] TTF itself is not an aromatic group, it is a 14 π electron system that is oxidized at 0.37 V to give a radical cation, which is aromatic.[62,132] This radical cation can further be oxidized at 0.67 V to a dication aromatic structure.[132] This unique property has made TTF one of the most widely studied electron donor molecules.[132] Soon after the first reported synthesis of TTF, $TTF^{+\bullet}$ Cl^- was discovered as one of the first organic conductors leading to the further development of TTF-based systems for molecular electronics.[132,133] The initial use of TTF in the 1970s yielded excitement and research into the synthesis of derivatives of TTF, including modification of the TTF group itself with other chalcogens which has yielded super conductive materials, as well as the extension of the central TTF group to synthesize

tetrathiafulvalene-3,4,5,6-tetrakis(4-benzoic acid) (TTFTBA), see Figure 1.8, which has been used to synthesize MOFs.[43,53,132,134]

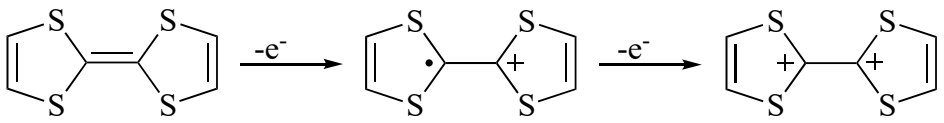

Figure 1.7: Oxidation half reaction of TTF, forming the cation radical, and the dication.

1.8.1. Tetrathiafulvalene in MOFs

Tetrathiafulvalene-based linkers have been used to synthesize several MOFs with a variety of metals and resulting topologies.[135] Zr(IV) was used to synthesize two different MOFs using TTFTBA and the functionalized tetrathiafulvalene-3,4,5,6-tetrakis(2-methyl-4-benzoic acid) (Me-TTFTBA), see Figure 1.8.[135] Su *et. Al.* obtained two different 3D MOFs with the **scu** and **she** topologies using the TTFTBA and Me-TTFTBA linkers, respectively.[135] See Figure 1.9 of the **scu** TTFTBA MOF. These MOFs were used to generate Ag, Pd, and Au nanoparticles *in situ* and the MOF@NP composites were used for aerobic oxidation of alcohols.[135] Narayan *et. Al.* reported a TTFTBA MOF using Zn(II).[134] This MOF is 2D and has infinite 1D channels with a structure that has an optimal arrangement of stacked TTF motifs. Due to this stacking arrangement, the MOF exhibits high charge mobility and high conductivity.[134] These Zn(II)-TTFTBA MOFs have been studied for numerous applications such as catalysis and electrical conductivity.[134,135] MOFs using TTF-containing linkers have been shown to have useful electrochemical properties as well as high conductivity when structures allow for TTF π-π stacking, facilitating electron movement via a through space pathway.

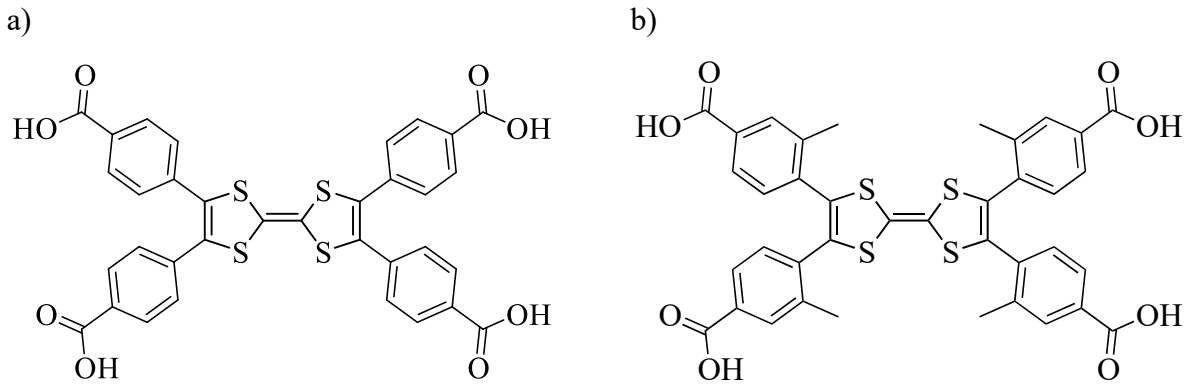

Figure 1.8: Tetracarboxylate linkers with tetrathiafulvalene motif, tetrathiafulvalene-3,4,5,6-tetrakis(4-benzoic acid) (TTFTBA) (a) and tetrathiafulvalene-3,4,5,6-tetrakis(2-methylbenzene-4-carboxylic acid) (Me-TTFTBA) (b).

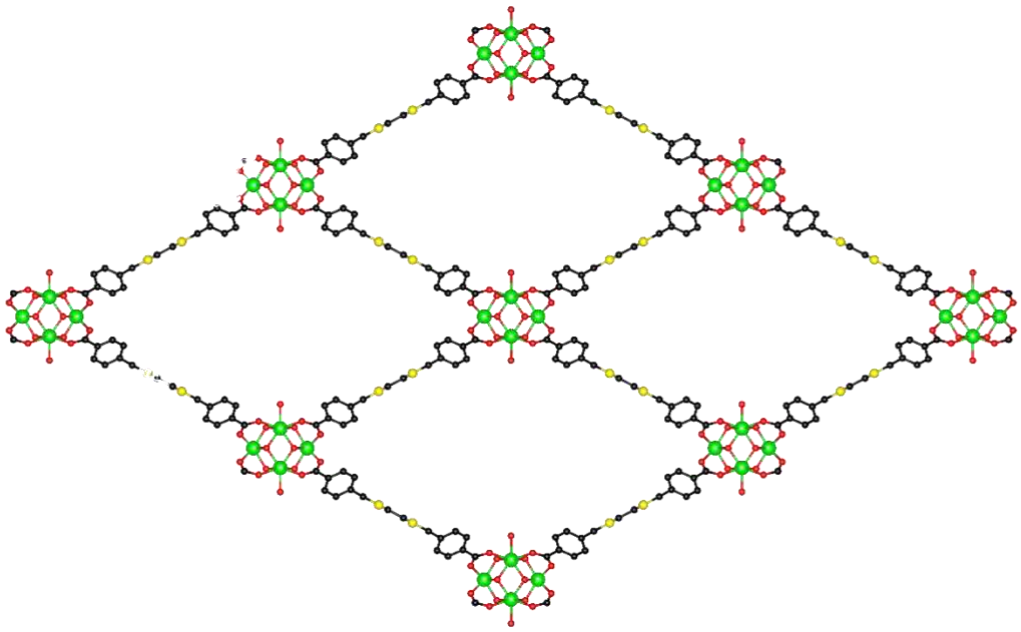

Figure 1.9: TTFTBA **scu** MOF synthesized with Zr(IV) hexanuclear clusters by Su *et al*. Black represents C, yellow is S, lime is Zr, red is O, H omitted for clarity.

1.8.2. Rare-Earth TTFTBA MOFs

Rare-earth metals have also been used to synthesize MOFs with the TTFTBA linker. La(III) was used by Xie *et. Al.* in 2019 to create three different MOFs with a 1D chain SBU.[136]

The MOFs were designed to optimize the π-π stacking between TTF motifs, and the structure can be described as a π-π interacting stack of linkers bonded to a chain of La(III) coordinating to the carboxylates, see Figure 1.10.[136] Three different MOFs were synthesized by varying the ratio of reaction solvents: N,N'-dimethylformamide (DMF), water, and ethanol. Each MOF has a different distance between the S atoms of the stacking linkers varying from 3.6 – 7.1 Å with higher conductivities associated with shorter distances, attributed to the through space pathway. Interestingly when analyzed topologically by two different methods, two of the three MOFs have previously undescribed topologies, while one is of the **tfo** topology, which has not yet been observed in MOFs with chain-based nodes.[136]

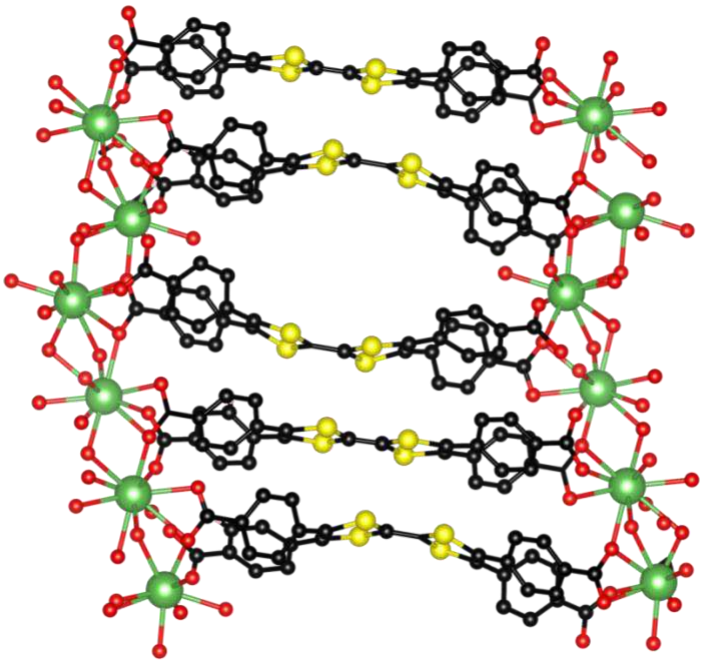

Figure 1.10: Illustration of the La(III) chain and the coordinating oxygens and the carboxylates of the TTFTBA linkers synthesized by Xie *et al.*[136] La(III) is represented by green spheres, C is black, O is red, S is yellow, the H are omitted for clarity.

Xie *et. Al.* also used the RE metals Tm(III), Yb(III), and Lu(III) to synthesize 2D sheet MOFs with TTFTBA.[136] These three isostructural frameworks contain an SBU with two metal atoms coordinated by carboxylates from six linkers. Each tetratopic linker is

connected to four different metal clusters with the connectivity creating a 2D sheet structure with π-π stacking in the layer and between the layers. The Tm(III)-based MOF has an S-S stacking distance as short as 3.7 Å.[137] Similar to the previous study discussed, these three MOFs yielded a new topology **lsx**, this indicates that the π interactions possibly yield new modes of MOF self-assembly.[136,137]

The synthesis of 3D MOFs with TTFTBA and Y(III), Sm(III), Gd(III), Tb(III), Dy(III), Ho(III), and Er(III) was reported in 2020 by Su *et. Al*.[138] These MOF have the **shp** topology and a nonanuclear RE(III)-cluster node connected to 12 carboxylates (Figure 1.11). Of the 7 MOFs synthesized, three were characterized by single crystal X-ray diffraction: Tb(III), Er(III), and Dy(III) and the structure determined. The cluster contains 9 RE(III) metal ions, each of which is coordinated to 9 oxygen atoms of three different types: bridging μ_3-O/OH atoms between the RE(III) metal ions, carboxylate oxygens from the linker, and oxygen atoms from terminal H_2O molecules. Thus the chemical formula is $RE_9(\mu_3\text{-}OH)_{13}(\mu_3\text{-}O)(H_2O)_9(CO_2)_{12}$, giving rise to a neutral framework. The redox activity of these materials was characterized by solid-state cyclic voltammetry, and the magnetic properties of the materials were also characterized to determine the MOFs use as a "redox-switchable potential single-molecule-magnet".[138] These RE(III)-based TTFTBA frameworks demonstrate the variety in structure and potential applications that the TTF motif brings to MOFs.

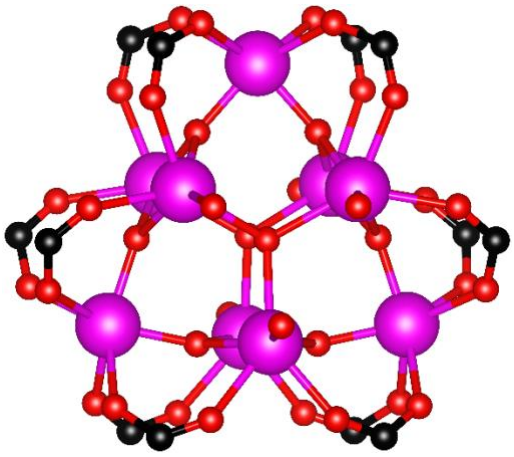

Figure 1.11: Illustration of rare-earth nonanuclear cluster, pink spheres represent RE(III) ions, black is C, and red is O.

1.8.3. Redox Properties in MOFs

Redox activity in MOFs has been shown to be possible due to innate properties of the metals and the linkers used in the framework.[139] Additionally, it is possible to introduce guest materials into the framework to add redox activity that is not innate to the framework itself.[139–142] Meilikhov *et. al.* incorporated ferrocene, cobaltocene, and ferrocene derivatives into the channels of MIL-47(V) and MIL-53(Al) (Figure 1.12a and 1.12b). These redox active guests formed stabilizing hydrogen bonding interactions within the channels of the MOF showing significant differences in redox activity depending on the functionalization of the metallocene (Figure 1.12c).[139] The redox properties of these composite materials were characterized by differential pulse voltammetry which indicates a lower current from the materials incorporated into the MOF then the free molecules due to the rigid position of the molecules in the framework decreasing diffusion. A shift of 100 mV was also observed in the potential when compared to the free molecule, due to hydrogen bonding of the molecule to the framework. This study highlights the possibility of tuning the redox activity of molecules when incorporated into a MOF. [139,140]

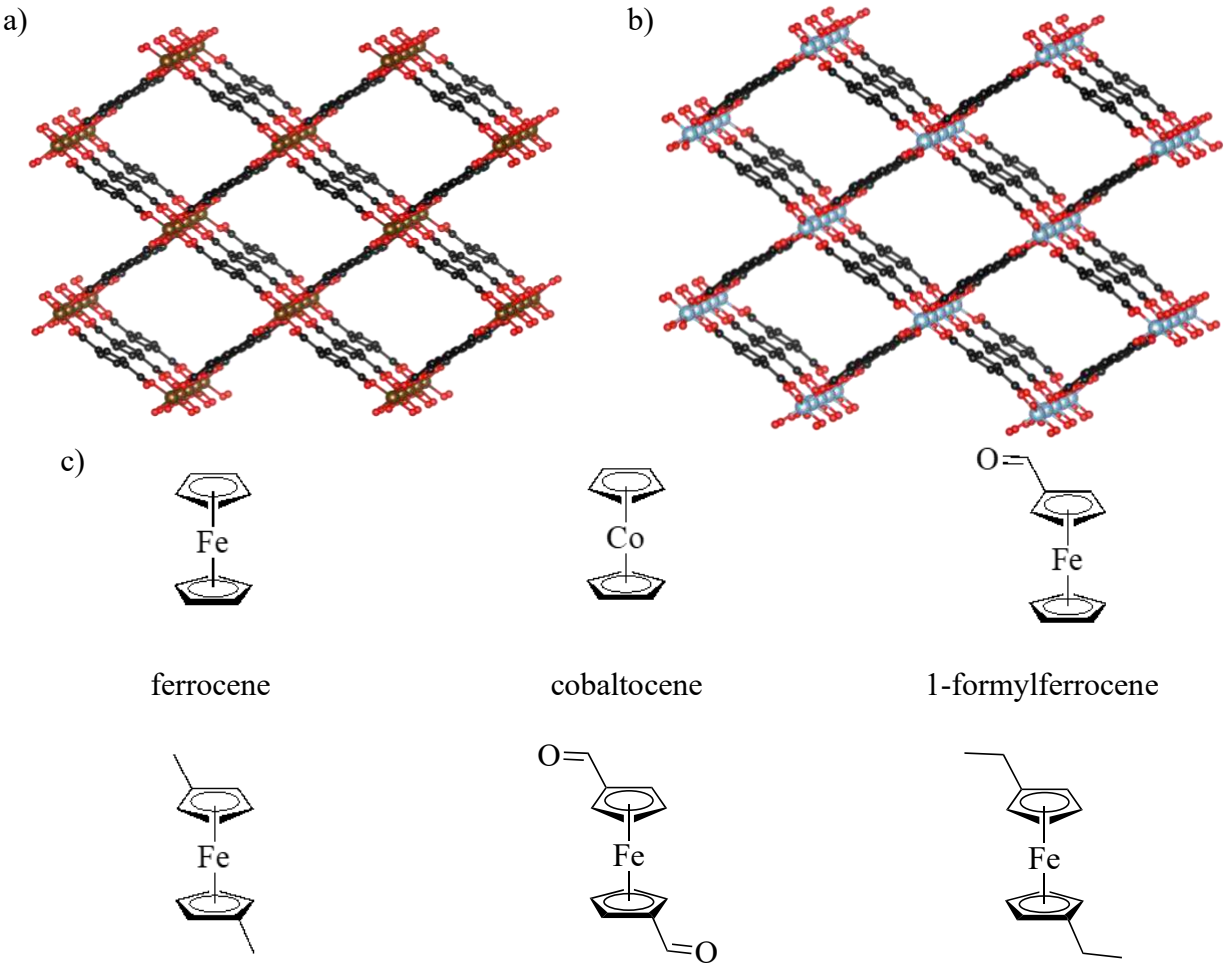

Figure 1.12: Structures of MIL-47(V) (a) and MIL-53(Al) (b) showing metal/metalloid-oxygen chains and channels in the framework. Black spheres represent C, red are O, brown are V, and light blue are Al, H atoms are not shown for clarity. The metallocenes Meilikhov *et al.* introduced into the pores of the MOF to introduce redox activity (c).

Another guest material introduced to a MOF was reported by Halls *et. Al.,* who incorporated alizarin red S molecules into the Zn based UMCM-1, see Figure 1.13a and 1.13b.[141] These materials were analyzed by cyclic voltammetry using a variety of electrolytes and solvents; though the materials were concluded to not be a robust redox system due to the consistent dissolution of the guest material into the electrolyte.[140,141] Further studies by the same group

integrating methylene blue (Figure 1.13c) into the same UMCM-1 framework were more successful using custom electrodes specifically designed to measure charge transport processes in the material, allowing the group to proceed further toward the end goal of electrochemical reduction of CO_2.[140–142]

a)

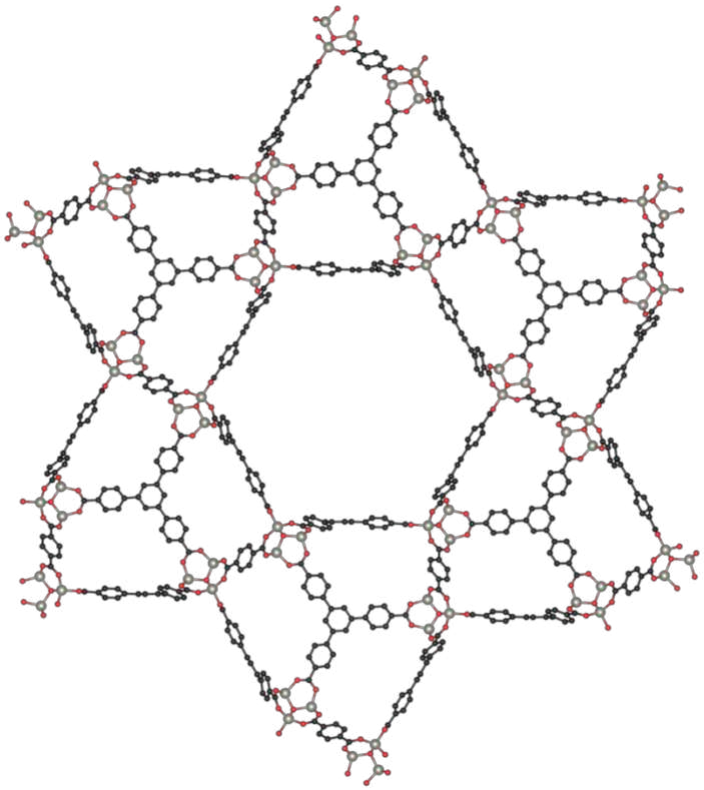

b)

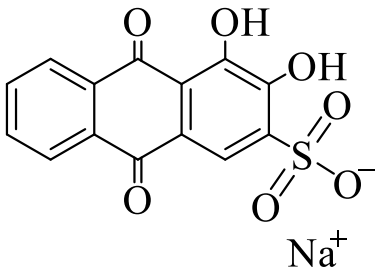

c)

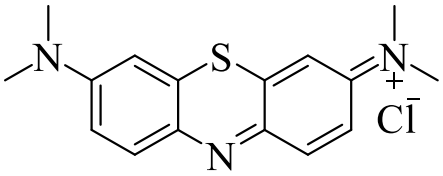

Figure 1.13: UMCM-1 (a), alizarin red S (b), and methylene blue (c). Red spheres represent O, black for C, and silver for Zn, H are omitted for clarity.

Redox active MOFs are potentially useful for a variety of applications including catalysis where redox hopping has been a focus of research on artificial photosynthesis such as water oxidation reactions.[140,143,144] In addition, gas separations using reduced redox active MOFs have shown improved uptakes of H_2, CH_4, and CO_2 when using alkali counter ions with uptake directly related to both the ion and the number of reduced atoms in the material.[140,145–147] Molecular electronics can take advantage of redox switchable absorbance properties for use in chemical sensors and molecular electronics, while numerous other switchable properties including electrochemiluminescence and electrochromism have been explored for electroanalytical and

optoelectronic uses.[140,148–150] The properties of redox active MOFs are diverse and can create a large impact on a variety of commercial sectors from biotechnology to catalysis.

1.9. Synthetic Methods

MOFs have been reported to be synthesized by numerous methods. These include solvthermal,[22,23,109,138] hydrothermal,[9,118,151,152] microwave assisted,[151,153] mechanochemical,[152,154,155] and electrochemical syntheses.[156,157]

1.9.1. Solvothermal Methods

The most common synthesis method for MOFs is *de novo* solvothermal synthesis.[5] This method includes mixing the metal salt and the linker in a high boiling point solvent such as N,N'-dimethylformamide (DMF), N,N'-diethylformamide (DEF), and N,N'-dimethylacetamide inside a vessel. These mixtures are then heated typically with a sand bath and hotplate or convectively using an oven for a set amount of time. All parameters including molar ratios, temperature, and time can be optimized to dictate the crystallite size, quality, purity, and topology of the resulting MOF. As part of the solvothermal synthesis, a modulator can be used for the formation of MOFs that are particularly difficult to obtain and to minimize the production of undesired products, as well as minimize production of mixed phase products.[158,159]

A modulator is a monotopic ligand which is used to form dynamic bonds with the metal precursor. These interactions slow down the formation of the framework by competing with the linker for access to metal coordination sites.[5,160] Modulators commonly have a functional group that is the same as the functional groups on the linker (i.e., carboxylate), though other modulators have been used such as HCl.[161] Notably, in the synthesis of RE-MOFs with multinuclear cluster nodes, fluorinated modulators have been found to be particularly effective, see Figure 1.14. In RE-MOF synthesis commonly used modulators are trifluoroacetic acid (TFA), 2,6-difluorobenzoic acid (DFBA), and 2-fluorobenzoic acid (FBA).[22,23,158] It is thought that these hydrophobic groups protect the RE cluster during assembly and evidence has been presented that the oxocluster itself may be composed of some bridging fluoro ligands.[162]

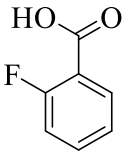

2-fluorobenzoic acid

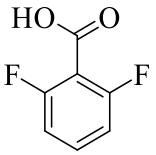

2,6-difluorobenzoic acid

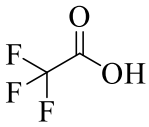

trifluoroacetic acid

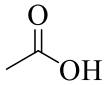

acetic acid

Figure 1.14: Various modulators used for the synthesis of MOFs.

1.9.2. Hydrothermal Methods

Hydrothermal synthetic methods are very similar to the above described solvothermal methods (1.9.1) though the metal and linker are not reacted in a high boiling point solvent they are simply reacted in water. Hydrothermal methods present multiple advantages to MOF synthesis, these include, increasing the safety of the MOF synthesis as the most used solvents are not as safe as water, decreasing the cost of the synthesis, and minimizing the amount of hazardous solvents produced as waste.

1.9.3. Post-synthetic Modifications

When attempting to synthesis some MOFs, *de novo* synthesis can be challenging or even impossible. In these cases, post-synthetic strategies can be used. Post-synthetic modification methods include transmetalation, solvent assisted ligand incorporation (SALI), and solvent assisted linker exchange (SALE).[22,124,163] These three methods are used to replace either the metals in the MOF, append ligands to a MOF node, or exchange the linkers in a MOF, thus often creating mixed metal and mixed linker MOFs. SALE has been shown to be effective in a large variety of MOFs, including materials that are extremely stable such as MIL-53(Al) which has shown to be stable against water and phosgene reagents, but is still able to undergo SALE.[164,165] SALE can occur regardless of the external stability of the framework due to the small energy differences between the incoming and outgoing linkers.[164] Multiple mechanisms have been proposed for SALE and are dependent on the identity of the MOF used. The most notable is a single-crystal-to-single-crystal mechanism, where the initial crystallite of a MOF is maintained throughout the experiment and linkers are introduced in a solvent and exchange occurs with no noticeable change in the morphology of the crystallite.[164,166] Another mechanism by which SALE can proceed is one

where the morphology is not maintained throughout the exchange, and this is referred to as dissolution-reassembly processes. Further studies on the thermodynamics and kinetics of SALE are being conducted, though the foremost and well established revelation with regards to SALE is that the solvent and its interactions with the MOF are the most important factor for the successful application of this post-synthetic modification technique.[164,165,167,168]

1.10. Activation

During the synthesis of porous materials, like MOFs, significant amounts of solvent, reagents, and side products can be trapped in the materials after synthesis. These guests must then be removed to access the pores of the MOF. There are multiple procedures for activation of MOF materials, which include vacuum drying,[109,169] solvent exchange,[5,109,170] super critical CO_2 exchange,[171,172] freeze-drying,[171] and chemical treatment.[171]

1.10.1. Solvent-Exchange for Activation

A crucial step in the removal of guest materials from MOF pores is a solvent exchange process. This procedure involves the use of a series of solvents in order of decreasing boiling point to solvate the guests trapped in the pores. The goal of solvent exchange is to the replace the high boiling point solvents trapped in the material with a lower boiling point solvent as well as to remove other guests (i.e., starting materials, byproducts) from the pores.[5] These guests must be removed before further activation as heating (with vacuum activation) or cooling (super critical CO_2 activation) the MOF with guests can lead to framework collapse.[171] Solvent exchange procedures can be optimized for soaking time, number of washes, as well as the solvent itself to maximize removal of guests.

Solvent-exchange is commonly followed by vacuum activation. Vacuum activation is simply heating the material under vacuum to remove any remaining (ideally low boiling point) solvent molecules, typically using a vacuum below 0.66 Pa. This lower pressure decreases the boiling point of the guest solvent molecules allowing for them to be removed from the MOF pores. The temperature and length of time can then be tailored to the MOF to optimize the complete activation procedure.

1.11. Characterization

Characterization techniques for the analysis of MOFs can vary greatly depending on the application of interest for the material. The most essential characterization is powder X-ray diffraction (PXRD), which determines the purity and the crystallinity of the material; single crystal X-ray diffraction (SCXRD) which determines the crystal structure of a large enough crystallite; nitrogen (N_2) adsorption/desorption isotherms, to determine the porosity and surface area of the MOF; nuclear magnetic resonance (NMR) spectroscopy; thermal gravimetric analysis (TGA); scanning electron microscopy (SEM); inductively coupled plasma mass spectrometry (ICP-MS); cyclic voltammetry (CV) for redox active MOFs; and diffuse reflectance infrared Fourier transform spectroscopy (DRIFTS).

1.11.1. Powder X-ray Diffraction

Powder X-ray diffraction is the most fundamental characterization method for MOFs. PXRD allows for the determination of crystallinity of the bulk material.[5] Fundamentally PXRD is used as a fingerprinting technique and the crystalline structure of a material is confirmed based on a simulated diffraction pattern that is calculated using either collected or literature analysis via SCXRD, see Figure 1.15. The diffractogram for a given material can be used to determine information on the phase composition, unit cell dimensions, and crystallite size. Upon analysis of a diffractogram the reflections indicate the d spacings present in the MOF using Bragg's law, which correlates the angle of diffraction of X-ray radiation with the distance between crystallographic planes in the MOF. The width of a reflection indicates the size of the diffracting crystallite and the intensity of the reflection indicates electron density within the diffracting planes.

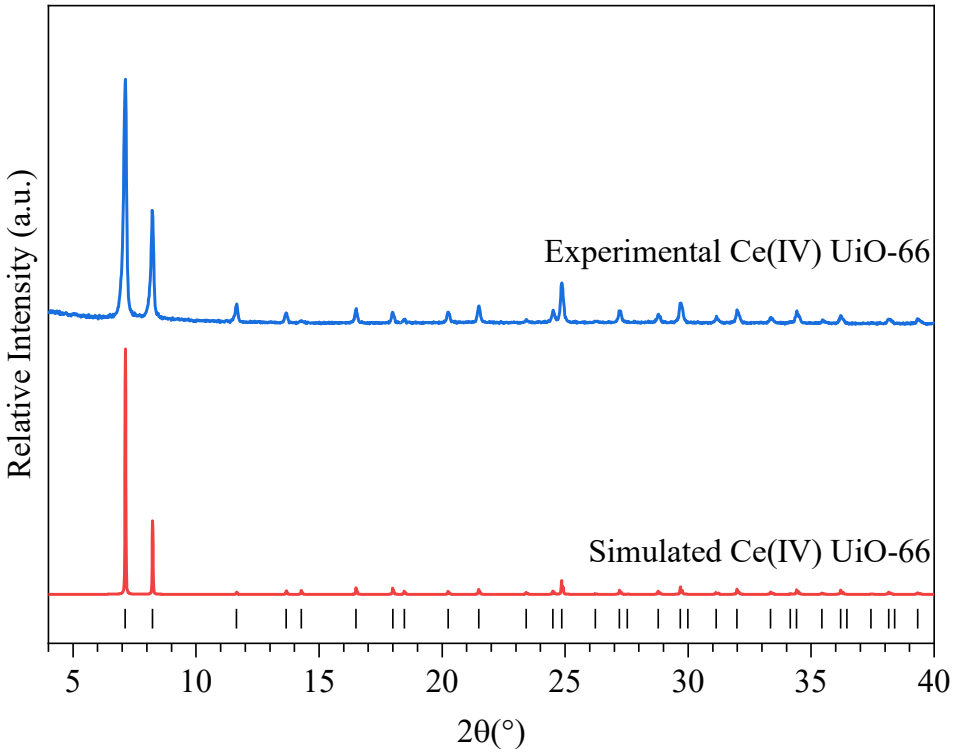

Figure 1.15: Stacked PXRD patterns used for fingerprinting of PXRD to compare the blue experimental PXRD pattern with the red simulated pattern. The black lines indicate the allowed reflections of the material.

1.11.2. Nitrogen (N_2) Adsorption and Desorption Isotherms

To determine porosity and surface area of a MOF material, N_2 adsorption and desorption analysis can be used. After samples are processed by solvent-exchange and vacuum activation an N_2 isotherm is collected. This isotherm is measured at the boiling point of liquid N_2, 77 K, as at this temperature the N_2 gas will enter the MOF and condense in the pores. The N_2 condensing in the material allows for the quantification of the amount of N_2 that is interacting with the MOF surfaces and filling the MOF pores. This condensation will first form a monolayer of N_2 in the MOF and then continue to condense to form a multilayer. The relative pressure of N_2 and the amount of N_2 adsorbed on the MOF are plotted yielding the isotherm.

The shape of a gas adsorption isotherm is characteristic of the type of material and related to the size of pores. Gas adsorption isotherms are classified into 6 categories, Type I-VI, see Figure 1.16. Type I isotherms are characteristic of materials with micropores (diameter (d) < 2 nm) and are subcategorized: Type I(a) indicate narrow micropores with a diameter of less than 1 nm and Type I(b) which contain larger micropores. Type II and III isotherms indicate a microporous (d > 50 nm) or nonporous material, with Type II showing where monolayer formation occurs, while Type III does not. Type IV isotherms are the result of mesoporous (2 nm < d < 50 nm) materials and are further subcategorized: Type IV(a) with cylindrical pores with a diameter larger than 4 nm and Type IV(b) with mesopores smaller than 4 nm. Type V isotherms are similar to Type III materials though the pores do not fill until there is a larger pressure of adsorbent present, and Type VI which only occurs in nonporous materials that adsorb layer by layer.[173]

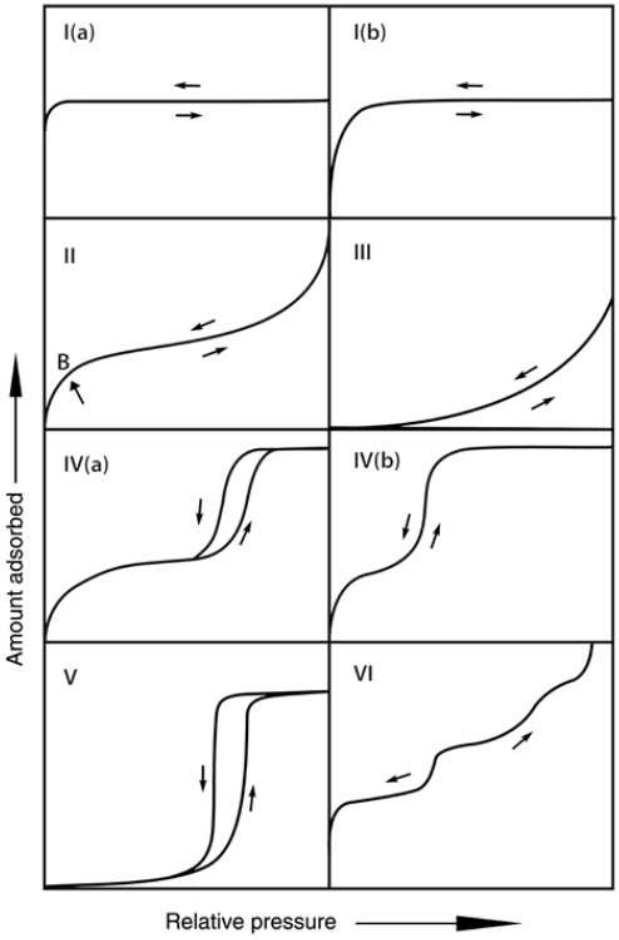

Figure 1.16: Representation of each type of isotherm from Type I-VI possible for nonporous and porous materials. Figure obtained from Thommes *et. Al.*[173]

In addition to the qualitative results indicated by a N_2 isotherm, the surface area of a material can be calculated. For MOFs, this is typically calculated using Brunauer-Emmet-Teller (BET) theory to mathematically describe physisorption.[174] In contrast to Langmuir theory which is limited to only Type I isotherms and assumes only monolayer adsorption,[175] BET theory is used to predict the number of atoms used to create a monolayer even if no perfect monolayer ever exists throughout collecting the isotherm. BET theory uses mathematical methods to model the adsorption of N_2 on a MOF and thus to determine the BET area of the material.[174] Further analysis of the isotherm can be done using non-local density functional theory (NLDFT). NLDFT matches

the experimental isotherm to a series of theoretical isotherms of materials with a variety of pore sizes to determine the pore volume and pore size distribution of the material.[176,177]

1.11.3. Thermogravimetric Analysis (TGA)

Thermogravimetric analysis is used to analyze the thermal decomposition of a MOF as well as to observe the relative amount of mass related to solvent, linker, and inorganic components of the material. These measurements occur by measuring the mass of a material as the temperature is increased under a flow of gas typically (N_2, Ar, or air), and can be combined with inductively coupled plasma mass spectrometry to determine the chemical formula of a MOF. Further thermal analysis of MOFs includes variable temperature PXRD (VT-PXRD) which can be used to observe the phase of a MOF at a variety of temperatures.[5]

1.11.4. Scanning Electron Microscopy (SEM)

While optical microscopy of MOFs is possible for particularly large crystallites, scanning electron microscopy (SEM) is the most common technique used to observe the size and morphology of MOF crystallites as magnification of up 3 000 000x can occur.[178] Due to the insulating nature of most MOFs when exposed to an electron beam, they undergo charging. Charging is the buildup of electrons in the surface of the MOF and it can be avoided by sputtering samples with a layer of highly conductive metal such as Au or Os.[5]

1.11.5. Proton Nuclear Magnetic Resonance (^{1}H-NMR) Spectroscopy

Analyzing linker incorporation as well as the presence of remaining modulators and solvents can be achieved using proton nuclear magnetic resonance (^{1}H-NMR) spectroscopy. Nuclear magnetic resonance uses electromagnetic radiation to change the direction of an atom's nuclear magnetic moment.[179] At a defined frequency the nuclear magnetic moment will flip direction, the frequency of the flip is characteristic of the chemical environment of a given nucleus.[179] ^{1}H-NMR spectroscopy is the analysis of the chemical conditions around a hydrogen nucleus. MOF samples must be digested in an acid such as D_2SO_4 and are often heated before dissolving the sample in a deuterated solvent such a DMSO-d_6.[5] Further analysis of MOFs via ^{1}H-NMR spectroscopy is used to determine the success of SALE and SALI procedures.[180]

1.11.5.1. SALE Quantification

The use of ^{1}H-NMR spectroscopy for the quantification of SALE is achieved by comparing the relative integration of peaks representing different protons. Since the chemical conditions around each proton present in two different linkers are different, multiple peaks will appear in an ^{1}H-NMR spectrum. The area of each of these peaks corresponds to the abundance of each type of proton, and thus the abundance of each linker within the MOF. These measurements require the analysis of the initial MOF as a control sample, and complications such as peak overlap between the original linker and the newly incorporated linker can occur, nevertheless these complications can be resolved if there are additional non-convoluted peaks.[124,180]

1.11.6. Inductively Coupled Plasma Mass Spectrometry (ICP-MS)

Inductively coupled plasma mass spectrometry (ICP-MS) can be used to determine the concentration or ratios of various elements present in a MOF. ICP-MS uses plasma to ionize atoms and a quadrupole and/or octupole to separate the ions by mass. The quantity of various masses present can then be determined.[181] Some ICP-MS quantification for RE metals has shown limits of quantification between 120 ppt and 52 ppb, though these values vary by instrument.[182] Nevertheless, these extremely low quantitative limits have made ICP-MS the go-to analytical method for elemental analysis of RE materials. To analyze MOFs by ICP-MS the samples must be digested in a strong acid such as H_2SO_4 or HNO_3 under heating or microwave conditions and then dissolved and diluted in water to an acid concentration of 3-5%.[5]

1.11.7. Cyclic Voltammetry (CV)

Cyclic voltammetry (CV) is a fundamental electrochemical technique, used to investigate the oxidation and reduction behavior for a given compound.[183,184] Voltammograms can be collected using a one cell, three electrode setup (Figure 1.17), a working electrode, a counter electrode, and a reference electrode.[183] The working electrode will be swept over a range of potentials and this changing potential will create a current between the working and counter electrode, while the reference electrode is used to measure the potential relative to a reference. In order to perform CV, the electrodes must be placed in an electrolyte solution and the movement

of dissolved ions creates current observed in the voltammogram.[183,184] Supporting electrolytes commonly used in MOF CV include 0.1 M tetrabutylammonium hexafluorophosphate ($TBAPF_6$) in DMF,[185] 0.1 M Na_2SO_4 in water,[186] and 3 M KOH in water.[187]

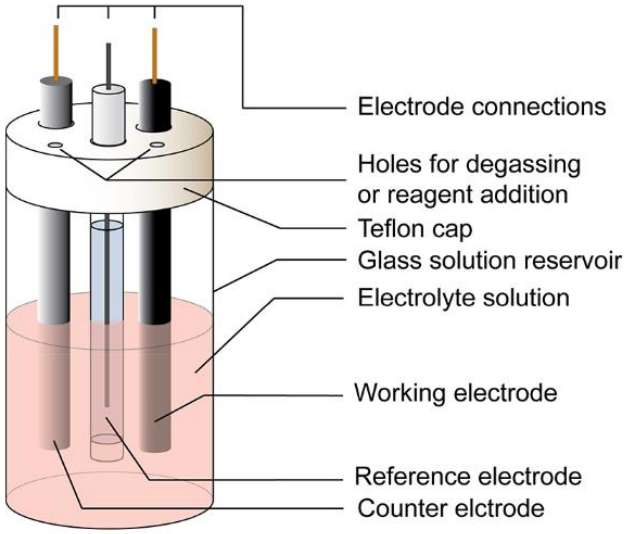

Figure 1.17: Diagram of the one cell three electrode apparatus. Indicating the working, reference, and counter electrode; the electrolyte solution, as well as the connection between the apparatus and the potentiostat. This diagram obtained from Elgrishi *et. Al.*[183]

In addition to the electrolyte selection, CV allows for further customization of analysis including the potential scan rate, the starting potential, the final potential, the number of cycles or segments, the maximum and minimum potential, as well as the composition of the three electrodes, and the direction of the scan. The voltammogram of ferrocene using the IUPAC convention is collected in 0.1 M tetrabutylammonium hexafluorophosphate ($TBAPF_6$) in dichloromethane (DCM) at 100 mV/s from 0-1 V and presented in Figure 1.18. This voltammogram serves as a standard representation for voltammograms presented in this thesis, with the oxidation, reduction, and direction of scan indicated. This voltammogram indicates the single electron redox reaction between ferrocene and ferrocenium. While this ferrocene CV is relative to the pseudoreference using silver wire, further CVs presented will be calculated relative to Ag/AgCl or the standard hydrogen electrode (SHE).

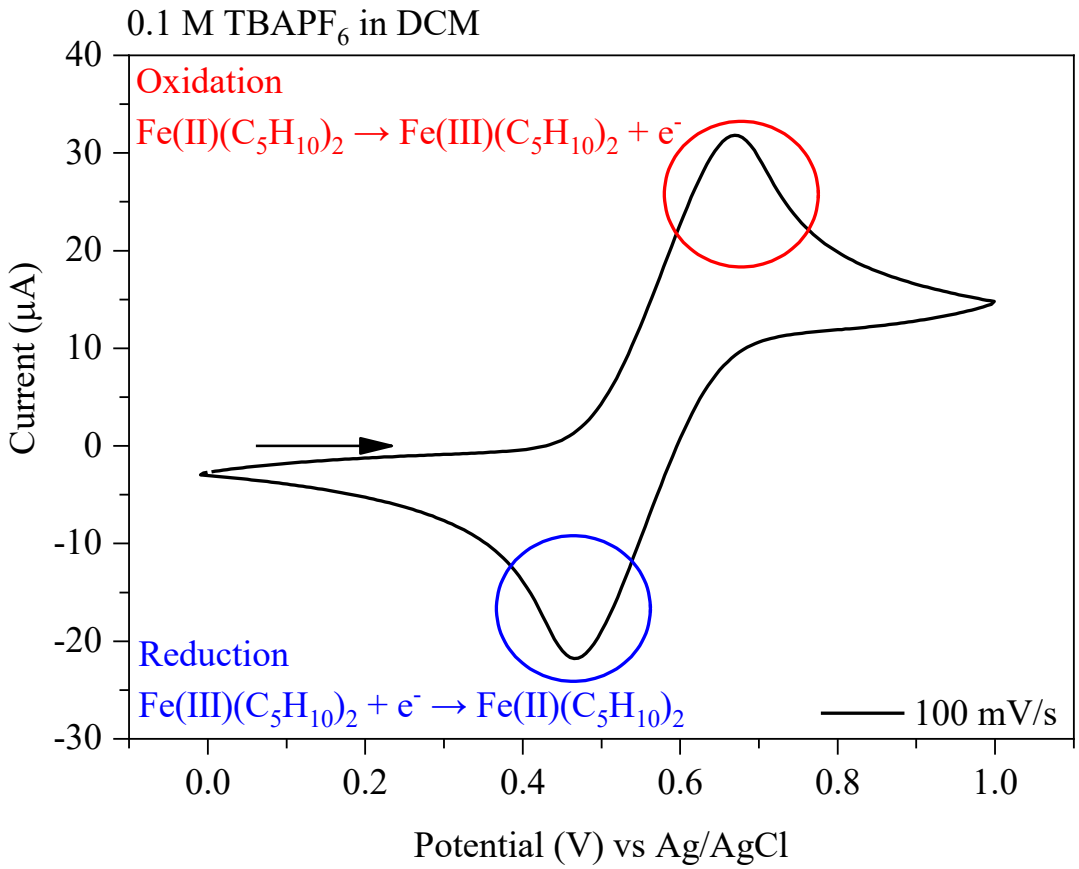

Figure 1.18: Cyclic voltammogram of ferrocene collected in 0.1 M $TBAPF_6$ in DCM at 100 mV/s from -0.01-1 V relative to the pseudoreference Ag/AgCl. The direction of scan is indicated as well as the oxidation and reduction curves and reactions indicating the one electron transitions. The oxidation reaction of ferrocene to ferrocenium occurs at 0.67 V and the reduction from ferrocenium to ferrocene occurs at 0.47 V.

Analysis of MOF materials by cyclic voltammetry is fundamentally different to the analysis of other solid materials or soluble materials. Not only do the insulating materials decrease the amount of current that can be detected by the instrument and indicate an electron transfer, the voltammogram peaks can possibly appear comparably to solid state electron transitions or in-solution electron transfers.[144] The CV discussed previously and shown in Figure 1.18 is indicative of in solution electron transfers as the ferrocene was dissolved in the dichloromethane electrolyte. The increase in current to a maximum and the slow decrease in current after the electron transfer

are described by the Nernst equation (Equation 1.1) and the Randles-Sevcik equation (Equation 1.2), which describe the equilibrium of ions in solution when the applied potential is changed, and the continued but slowing diffusion of ions throughout the solution to maintain charge balance.[183,188]

$$E_{cell} = E_{cell}^{\ominus} - \frac{RT}{zF} \ln Q_r$$

Equation 1.1: The Nernst equation where E_{cell} is the cell potential at the temperature T, $E_{cell}^{\ominus}$ is the standard cell potential, R is the gas constant, F is the Faraday constant, z is the number electrons transferred in the half reaction, and Q_r is the reaction quotient of the cell reaction.

$$i_p = 0.4463nFAC\sqrt{\frac{nF\nu D}{RT}}$$

Equation 1.2: The Randles-Sevcik equation where i_p is the maximum current, n is the number of electrons transferred in the half reaction, F is the Faraday constant, A is the electrode area, C is the concentration, ν is the scan rate, D is the diffusion coefficient, R is the gas constant, and T is the temperature.

Voltammetry of samples in the solid state and of adsorbed materials can be more challenging and requires that generally a solid material is operating as the electrolyte and the electroactive material.[189] Solid state CV techniques have notably been observed to be dependent on the scan rate (Figure 1.19), it is possible that at too low of a scan rate, the diffusion layer from the increasing current becomes larger than the electrode, and the resulting voltammogram (Figure 1.19A) does not indicate the characteristic diffusion peaks, while that analyzed at a faster scan rate does (Figure 1.19B). For these fundamental analyses the most relevant aspect of solid-state voltammetry is the difference in peak shape from solution-based CV. The peak shape in these solid-state analyses are described by the Randles-Sevcik dependence, with more gaussian peak shapes that depend on the scan rate.[189] In general the electrochemistry of MOFs can be described as a hybrid between solid state and solution state CV and qualitatively the shape of the peak can be used to approximate if the peak is characteristic of a solid-state or solution based voltammogram; this allows for further mechanistic insight into the structure of the MOF during

electron transfer. In the case of adsorbed electrochemically active materials, major differences in maximum current intensity between the oxidative and reductive peak are observed.[188] These differences are dependent on the strength of the interaction between the electrode and the oxidized or reduced material. In an example where the reactant is being reduced and interacts more strongly with the substrate then the reduced product, the oxidative peak will appear as expected for a solution based material, while the reductive sweep will yield a lower absolute change in current and appear more bell shaped.[188] Overall, due to the preparation methods of the working electrode and the unique porous nature of MOFs, it is likely that the voltammograms indicate a variety of these characteristics depending on the strength of the interactions with the substrate, the scan rate, the electrolyte used, and the amount of material deposited on the substate.

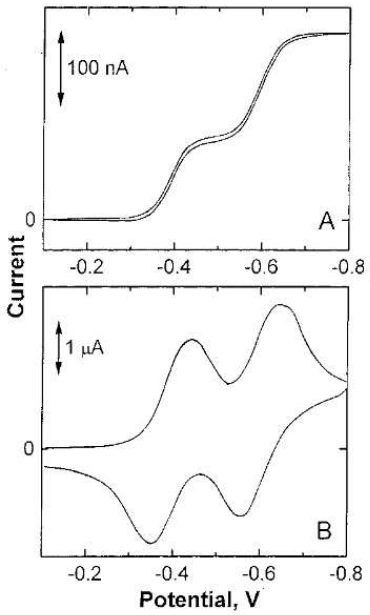

Figure 1.19: Solid state voltammetry of a mixed-valence ionically conducting material. Voltammograms were collected at 1 mv/s (A) and 51 V/s (B).

1.11.8. Diffuse Reflectance Infrared Fourier Transform Spectroscopy (DRIFTS)

Diffuse reflectance infrared Fourier transform spectroscopy (DRIFTS) is used to determine the presence of infrared (IR) active species in a MOF including monitoring the success of SALE procedures. DRIFTS procedures work through irradiating the sample with IR radiation and

monitoring the energy of the light that is reflected.[190] The energy of the light that is reflected can be compared to a control non-IR active material, KBr, to determine the energy of light that is absorbed by the material. These energies are characteristic of the functional groups present in the material. DRIFTS specifically uses reflectance as opposed to transmission IR allowing the analysis of powders and other bulk materials. MOF samples should be activated before DRIFTS analysis and can be run directly or diluted in a non-IR active material, commonly KBr.[5]

1.12. Scope of Thesis

This thesis focuses on the synthesis and characterization of redox active MOFs where the redox active component is either the metal cluster or the organic linker.

Chapter 2 describes the synthesis and characterization of Ce(IV)-UiO-66 with the linkers: benzene-1,4-dicarboxlic acid, 2-aminobenzene-1,4-dicarboxylic acid, 2-bromo-1,4-dicarboxylic acid, 2,5-dihydroxybenzene-1,4-dicarbocylic acid, 2-fluorobenzene-1,4-dicarboxylic acid, 2,3,5,6-tetrafluorobenzene-1,4-dicarboxylic acid, and Ce(IV) UiO-67 with 2,5'-bipyridine-5,5'-dicarboxylic acid. The materials are fully characterized and their fundamental electrochemical properties are analyzed by CV.

Chapter 3 involves the synthesis of the redox active TTFTBA linker, as well as selected examples of MOF synthesis attempts with Ce(III/IV), as well as synthesis of novel 3D MOFs using TTFTBA and RE(III) metals, with redox characterization by CV included for each material.

Chapter 2

The Fundamental Redox Characteristics of a Series of Ce(IV)-MOFs

2.1. Introduction

There is large variation in the potential applications of redox active MOFs. The primary avenue of study has been in redox catalysis, including the use of Ce(IV)-UiO-66 and the co-catalyst (2,2,6,6-tetramethylpiperidin-1-yl)oxyl for the oxidation of benzyl alcohol.[109] Another interesting example of redox catalysis with MOFs uses Ce(IV)-UiO-66-$(CH_3)_2$ in the oxidation of styrene and cyclohexene, with tert-butlyhydroperoxide as co-catalyst.[126] Both of these catalytic studies use the redox active Ce(IV) in the cluster of the MOF, and a co-catalyst as a terminal oxidant to oxidize the reduced Ce(III) back to Ce(IV). Additional studies on redox active MOFs include increasing the conductivity of MOFs via the redox hopping pathway (section 1.5).[43] The application of Ce(IV) as a redox active metal ion in cluster-based MOFs will be presented herein.

Ce(IV) is a well-known RE ion due to its oxidation properties.[116] It is also the most common of the RE metals, with an abundance similar to Cu.[116] The oxidative potential of Ce(IV) has been well-studied in coordination complexes and studies have indicated unique characteristics. Different from many other metal ions, Ce(IV) has shown a large range in oxidation potential depending on the coordination environment and the electrolytic conditions at which it was analyzed.[63] Redox potentials varying by more than 2 V have been observed under aqueous conditions, with the highest being $Ce(ClO_4)_3$ at 1.63 V vs SCE and the lowest being $Ce(C_6H_4O_2)_4^{4-}$ at -0.69 V vs SCE.[63,191,192] Similarly large variation between the redox potentials has been noted under non-aqueous conditions.[63] These large variations in the redox potential of the Ce ions indicates a large effect of the ligand on the coordination sphere of the Ce(III/IV). These unique effects from the coordinating ligands in conjunction with the ability to perform redox catalysis suggests that MOFs can be tuned through varying the organic linker for a wide range of catalytic oxidation reactions. Therefore, the effect of the MOF linker on the electrochemical potential of Ce(III/IV) in Ce-based MOFs is of interest from a fundamental perspective as well as an application-based one where minor molecular modification to the linker can change the redox behaviour of the MOF.

a) b)

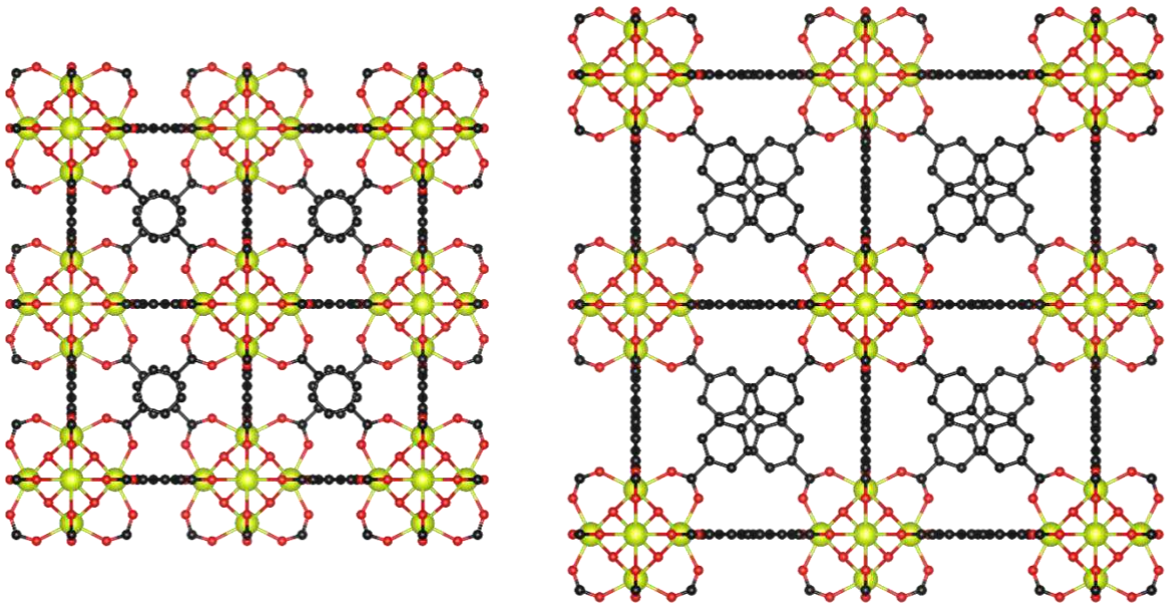

Figure 2.1: Ce(IV)-UiO-66 (a) and Ce(IV)-UiO-67 (b). Ce is represented by yellow spheres, C is black, and O is red; H atoms are omitted for clarity.

The electrochemical properties of Ce(IV) containing MOFs has been studied previously for Ce(IV)-MOF-808 with carbon nanotubes,[186] Ce(IV)-UiO-66 with Ni foam,[193] Ce(IV)-MOF with carbon nanotubes or graphene oxide,[187] and Ce(IV)-UiO-66 with nafion.[185] All of these studies involve creating a composite material containing the MOF, while none of them explored variations in functional groups on the MOF linker and the associated effects on the redox potential of the MOF. An interesting platform for studying the electrochemical changes of Ce(III/IV)-MOFs based on systematic changes to MOF linkers is the **fcu** platform, including Ce(IV)-UiO-66 and Ce(IV)-UiO-67 (Figure 2.1), which are isostructural to the archetypal Zr(IV)-UiO-66 and Zr(IV)-UiO-67. Ce(IV)-UiO-66 has been synthesized with a variety of linkers (section 1.7.3) and herein the electrochemical characteristics of some of these MOFs is presented. The linkers chosen for this study, shown in Figure 2.2, include BrBDC, FBDC, F_4BDC, NH_2BDC, DOBDC, and for the longer UiO-67 linker: BPyDC. Various challenges arise during the synthesis of these materials including the insolubility of many of these linkers in the solvents used for solvothermal synthesis, most notably BPyDC, which is not soluble in DMF, and requires extensive washing of the final MOF product using DMSO. In order to ensure the study of only the redox potential of Ce(IV), the

linkers must not undergo a redox event in the range of study. Of the linkers selected only NH_2BDC was hypothesized to possibly have redox activity, due to the molecular similarity to the electrochemically active aniline.[194] Upon analysis by solution CV, (Figure S.2.3) no redox events were observed in the range analyzed for Ce(IV)-UiO-66-NH_2. The absence of electrochemical activity from the linker ensures that the voltammetry performed to characterize the redox potentials of the series of Ce(IV)-UiO-66/67 analogues, is from the redox activity of Ce(IV) in the MOF cluster.

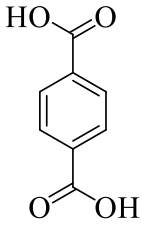

benzene-1,4-dicarboxylic acid (BDC)

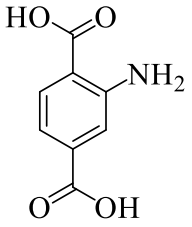

2-aminobenzene-1,4-dicarboxylic acid (NH_2BDC)

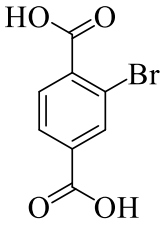

2-bromobenzene-1,4-dicarboxylic acid (BrBDC)

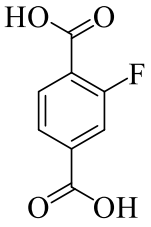

2-fluorobenzene-1,4-dicarboxylic acid (FBDC)

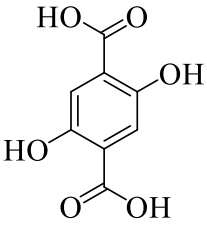

2,5-dihydroxybenzene-1,4-dicarboxylic acid (DOBDC)

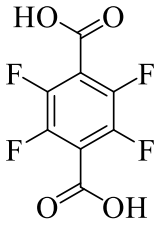

2,3,5,6-tetrafluorobenzene-1,4-dicarboxylic acid (F_4BDC)

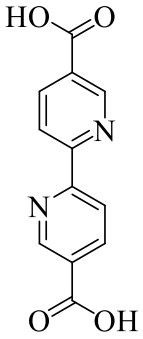

2,2'-bipyridine-5,5'-dicarboxylic acid (BPyDC)

Figure 2.2: The series of linkers used to synthesize Ce(IV) UiO-66 and Ce(IV) UiO-67 analogues.

2.2. Experimental Procedures

2.2.1. General Materials and Methods

All solvents and reagents were used without additional purification: N,N-dimethylformamide (DMF; C_3H_7NO, Fisher Chemical, ≥99.8%), acetone (C_3H_6O, Fisher Chemical, 99.5%), dimethyl sulfoxide (DMSO; C_2H_6OS, Fisher Chemical, 99.9%), methanol (CH_4O, Fisher Chemical, 99.8%), ethanol (C_2H_6O, Greenfield Global, 99%), deuterated sulfuric acid (D_2SO_4, Sigma Aldrich, 96-98%), deuterated dimethyl sulfoxide (DMSO-d_6; C_2H_6OS, Cambridge Isotope Laboratories, 99.9%), acetic acid ($C_2H_4O_2$, Fisher Chemical, 99.7%), diammonium Ce(IV) nitrate ($(NH_4)_2Ce(NO_3)_6$, Fisher Chemical, 99.5%), benzene-1,4-dicarboxylic acid (BDC; $C_8H_6O_4$, Acros Organics, >99%), 2-aminobenzene-1,4-dicarboxylic acid (NH_2BDC; $C_8H_7NO_4$, Acros Organics, 99%), 2-bromobenzene-1,4-dicarboxylic acid (BrBDC; $C_8H_5BrO_4$, AmBeed, 98%), 2,5-dihydroxybenzene-1,4-dicarboxylic acid (DOBDC; $C_8H_6O_6$, AmBeed, 98%), 2-fluorobenzene-1,4-dicarboxylic acid (FBDC; $C_8H_5FO_4$, AmBeed, 95%); 2,3,5,6-tetrafluorobenzene-1,4-dicarboxylic acid (F_4BDC; $C_8H_2F_4O_4$, AmBeed, 95%), 2,2'-bipyridine-5,5'-dicarboxylic acid (BPyDC; $C_{12}H_8N_2O_4$, TCI America, >98%), tetrabutylammonium hexafluorophosphate (TBAPF_6; $C_{16}H_{36}F_6NP$, Fisher Chemical, 98%), sodium sulfate (Na_2SO_4, Fisher Chemical, >99%).

PXRD were collected using a Bruker D2 Phaser, or a Bruker D8 Advance both equipped with a CuKα X-ray source (λ = 1.54 Å) and a nickel filter. Powder materials were prepared via drop casting in methanol or neat onto a silicon wafer with a low-zero background sample holder. Scans were made over the range 4-20° 2θ with a step of 0.02° and a scanning speed of 0.2 s.

Nitrogen adsorption-desorption isotherm data were collected at 77 K using a Micromeritics Tristar II Plus surface area and porosity analyzer. Samples were vacuum activated for the time and temperature specified in the experimental procedure (Sections 2.2.2, 2.2.3, 2.2.4, and 2.2.5) using a Micromeritics Smart VacPrep with a hybrid turbo vacuum pump.

DRIFTS spectra were collected using a Thermo Scientific Nicolet 6700 FT-IR with an MCT detector with a resolution of 1 cm^{-1} from 4000-800 cm^{-1}. Samples were diluted in the IR inactive KBr.

H^1 NMR spectra were recorded using a 300 MHz Bruker spectrometer with shifts referenced to the residual solvent peaks. MOFs were digested using approximately 4 drops of deuterated sulfuric acid in 0.4 mL of DMSO-d_6.

ICP-MS data was collected using an Agilent 7500 series by the Concordia Center for Biological Applications of Mass Spectrometry (CBAMS).

SEM micrographs were collected on a Phenom ProX desktop SEM at 12 kV using the secondary electron detector. Before analysis samples were sputtered with gold using a Cressington 108 Auto/SE Sputter Coater with MTM-20 high resolution film thickness controller.

Cyclic voltammetry was performed using a Pine research Instrumentation Inc. WaveDriver 20 with a Pt mesh counter electrode and an Ag wire (nonaqueous electrolytes) or Ag/AgCl (aqueous electrolyte) reference electrode.

2.2.2. Synthesis of Ce(IV)-UiO-66 using BDC, BrBDC, and FBDC

Ce(IV)-UiO-66 with BDC, BrBDC, or FBDC was synthesized according to a literature method with minor modifications.[109]

BDC, BrBDC, or FBDC (0.2 mmol; 33 mg BDC, 49 mg BrBDC, 37 mg FBDC) was added to DMF (15 mmol, 1.2 mL) in either a 1, 1.5, or 2 dram vial. To this, 400 µL (0.212 mmol) of a 0.533 M diammonium Ce(IV) nitrate solution in water was added to the vial. The vial was then immediately placed in a 100 °C preheated sand bath and stirred vigorously for 15 minutes. Over the course of 15 minutes the reaction changed from an orange solution to a solution containing a pastel yellow precipitate. The precipitate was separated by centrifugation and solvent exchange was performed with DMF (5 mL) 3x and acetone (5 mL) 3x before being air dried and characterized by PXRD. The material was then activated under vacuum at 130 °C for 16 hours for BDC, 120 °C for 20 hours for BrBDC, or 100 °C for 16 hours for FBDC before the N_2 gas adsorption-desorption isotherm was collected.

2.2.3. Synthesis of Ce(IV)-UiO-66 using F_4BDC

Ce(IV)-UiO-66 with the linker F_4BDC was synthesized according to a literature method with very minor modifications.[128]

F_4BDC (0.5 mmol, 120 mg), diammonium Ce(IV) nitrate (0.5 mmol, 270 mg), water (1.25 mol, 23 mL), and acetic acid (50 mmol, 3 mL) were added to a 50 mL round bottom flask. The flask was then refluxed at 110 °C with vigorous stirring for 16-24 hours. Over the reaction period a white precipitate formed in the reaction mixture. The precipitate was separated by centrifugation and solvent exchange was performed with water (10 mL) 2x and acetone (10 mL) 2x before being air dried and characterized by PXRD. The sample was then activated under vacuum at 80 °C for 20 hours before the N_2 gas adsorption-desorption isotherm was collected.

2.2.4. Synthesis of Ce(IV)-UiO-67 with BPyDC

Ce(IV)-UiO-67 with the BPyDC linker was synthesized according to a literature method with very minor modifications.[109]

BPyDC (0.2 mmol, 49 mg) was added to DMF (15 mmol, 1.2 mL) in a 1, 1.5, or 2 dram vial. To this mixture 400 µL (0.212 mmol) of 0.53 M diammonium Ce(IV) nitrate in water was added. The mixture was then immediately placed in a 100 °C preheated sand bath and reacted for 15 min with vigorous stirring. After 15 minutes a yellow precipitate was present in the vial. The precipitate was separated by centrifugation and solvent exchange was performed with DMSO (5 mL) 2x, DMF (5 mL) 3x, and acetone (5 mL) 3x before being air dried and characterized by PXRD. The sample was then soaked in ethanol for 48 hours and then activated under vacuum at 140 °C for 16 hours before the N_2 gas adsorption-desorption isotherm was collected.

2.2.5. SALE Synthesis of Ce(IV)-UiO-66 with NH_2BDC and DOBDC

Post-synthetic modification using SALE following a literature procedure was used to synthesize Ce(IV)-UiO-66 with the linkers NH_2BDC and DOBDC.[180] Calculation of the number of moles of MOF used in each synthesis assumes that the MOF is defect free.

Ce(IV)-UiO-66 (0.02 mmol, 39 mg) and NH_2BDC or DOBDC (0.4 mmol, 72 mg) were mixed with methanol (250 mmol, 10 mL). The mixture was vortexed and sonicated for 5 minutes. The precipitate was separated by centrifugation and solvent exchange was performed with DMF (5 mL) 3x, and acetone (5 mL) 3x before being air dried and characterized by PXRD. The sample was then activated under vacuum at 40 °C for 24 hours before the N_2 gas adsorption-desorption isotherm was collected.

2.2.6. Electrochemical Analysis Methods

The preparation of films for analysis by CV was performed via drop casting, based on the literature methods reported by Shen *et al*. who reported voltammograms of Ce-MOF-808.[186] About 8 mg of the activated or not activated MOF of interest was dispersed in 1 mL of acetone and sonicated until a homogenous mixture was reached, about 5 minutes. The mixture was pipetted and dropped onto the conductive substrate; fluorine doped tin oxide (FTO) glass slides. The acetone was then evaporated at room temperature and the sample was dropped onto the slide 4 more times. These slides were then used as the working electrode in a three-electrode set up in the biopotentiostat, similar to that used by Shen *et al*. for the study of other Ce based MOFs.[186] For all CV analysis, the counter electrode was platinum mesh, while the reference electrode was varied depending on the electrolyte used. The three electrolytes used were, 0.1 M $TBAPF_6$ in DCM, 0.1 M $TBAPF_6$ in DMF, and 0.1 M Na_2SO_4 in water. For both $TBAPF_6$ electrolytes a pseudoreference electrode of Ag wire was used as reference and for the water electrolyte Ag/AgCl in 3 M KCl was used as reference. Cyclic voltammograms are all reported relative to the standard hydrogen electrode (SHE) for accurate comparison. This was calculated for each CV using two different methods depending on the reference electrode being used. For those analyses where the electrolyte was DMF or DCM, a ferrocene CV was obtained (Figure S.2.1). The difference between the observed oxidation potential and the oxidation potential vs SHE reported in literature (0.64 V) was used to adjust the MOF voltammograms relative to the SHE references instead of the Ag wire pseudoreference.[195] For the analysis of samples in water, the voltammograms were adjusted so that the Ag/AgCl reference was at the literature oxidation potential (0.2223 V).[188]

2.3. Characterization Results

Solvothermal methods for the synthesis of Ce(IV)-UiO-66, Ce(IV)-UiO-66-F, Ce(IV)-UiO-66-Br, and Ce(IV)-UiO-67-BPyDC were performed by adding 400 µL of a 0.53 M diammonium Ce(IV) nitrate aqueous solution to a heterogenous mixture of linker and DMF.[109] Upon addition of the Ce(IV) solution the reaction turned orange and the temperature of the dram vial increased indicating an exothermic reaction. After stirring for 15 minutes at 100 °C in the sand bath, the reaction mixture contained a pale-yellow precipitate. Synthesis of Ce(IV)-UiO-66-Br had

previously only been reported by mechanochemical methods using liquid assisted grinding, thus this synthetic scheme for this MOF is novel.[123] Hydrothermal methods for the synthesis of Ce(IV)-UiO-66-F_4 were performed by adding linker and diammonium Ce(IV) nitrate to a solution of water using acetic acid as modulator. After refluxing the mixture for 24 hours the reaction mixture contained a pale-yellow precipitate. The precipitate was washed, separated, and air dried before the bulk crystallinity and phase purity of the material was confirmed by PXRD (Figures 2.3a, 2.4a, 2.5a, 2.6a, and 2.7a). By comparing the PXRD pattern of each material to the simulated PXRD pattern calculated from the published SCXRD structures, the MOFs can be observed to have been successfully synthesized. The narrower peaks of Ce(IV)-UiO-66, Ce(IV)-UiO-66-F, Ce(IV)-UiO-66-Br, and Ce(IV)-UiO-67-BPyDC when compared to Ce(IV)-UiO-66-F_4 indicates that the crystallite size of Ce(IV)-UiO-66-F_4 (Figure 2.6a) is smaller than that of the MOFs synthesized solvothermally. Furthermore, the presence of only peaks that appear in the simulated patterns confirms the phase purity of the synthesized materials as additional peaks would indicate the presence of a crystalline impurity.

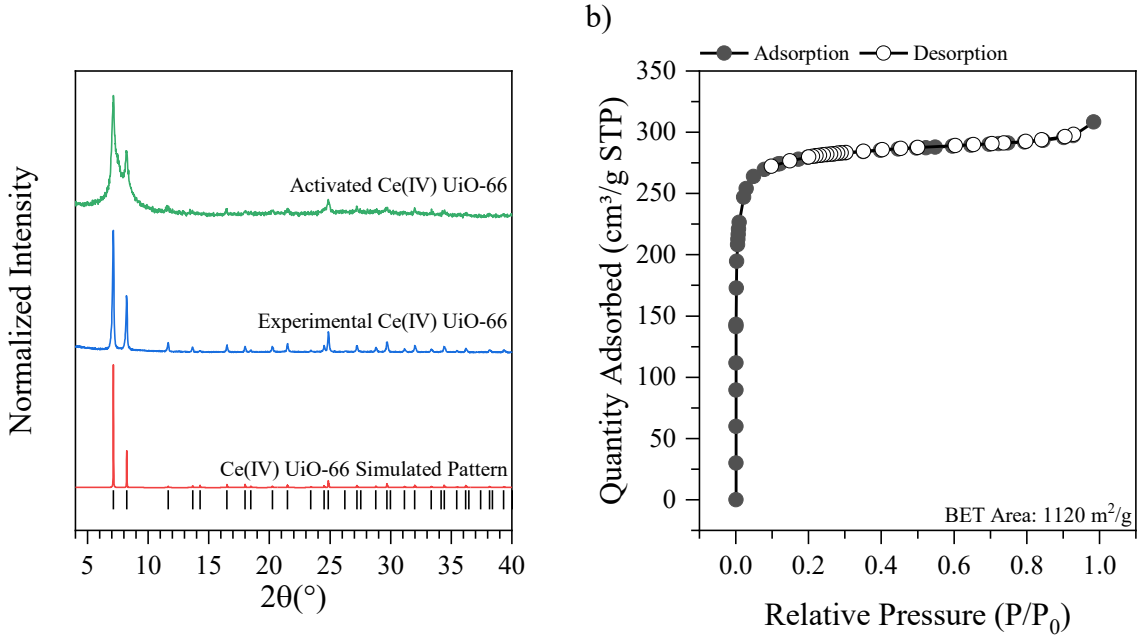

Figure 2.3: PXRD pattern of as-synthesized and activated Ce(IV)-UiO-66 (a) and N_2 gas adsorption-desorption isotherm and BET area of Ce(IV)-UiO-66 (b).

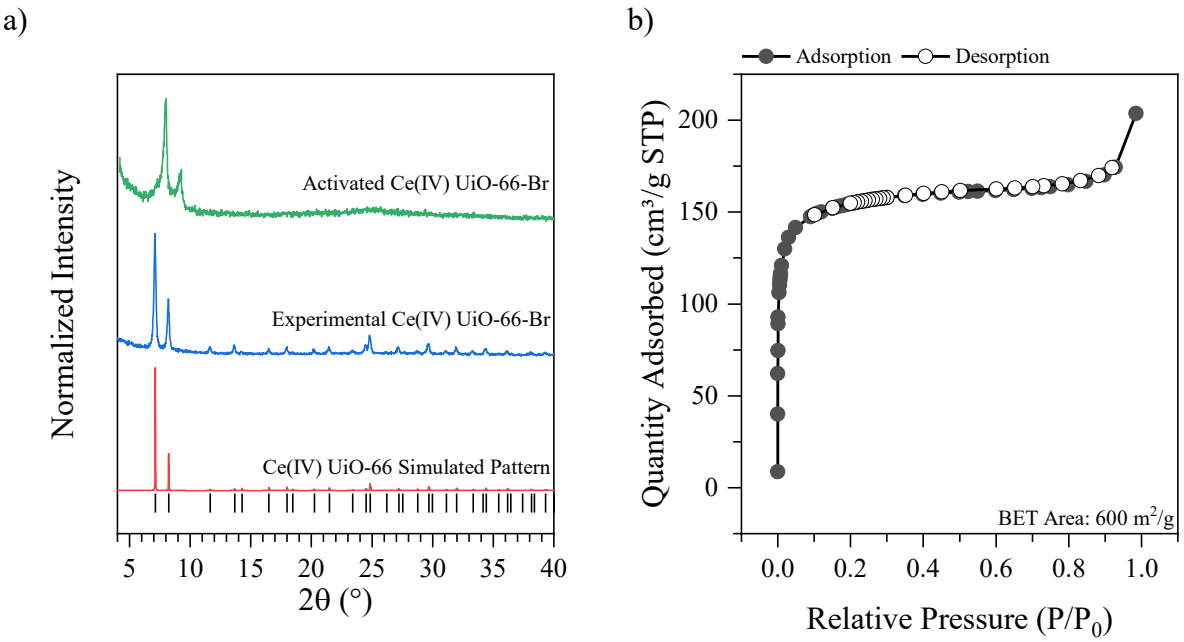

Figure 2.4: PXRD pattern of as-synthesized and activated Ce(IV)-UiO-66-Br (a) and N_2 gas adsorption-desorption isotherm and BET area of Ce(IV)-UiO-66-Br (b).

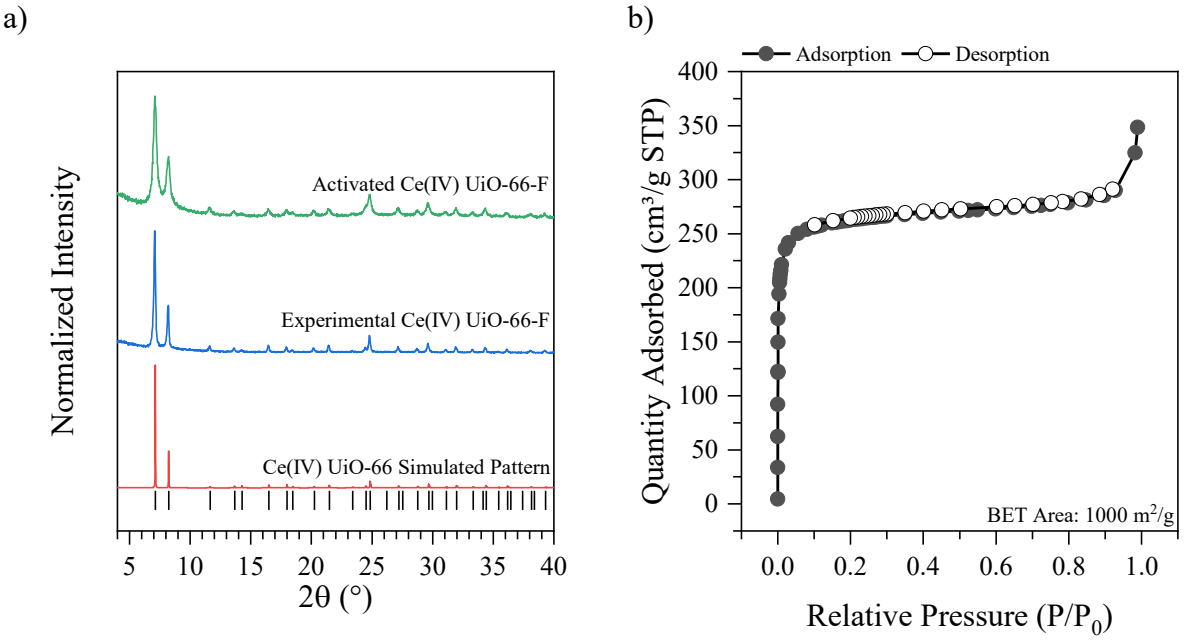

Figure 2.5: PXRD pattern of as-synthesized and activated Ce(IV)-UiO-66-F (a) and N_2 gas adsorption-desorption isotherm and BET area of Ce(IV)-UiO-66-F (b).

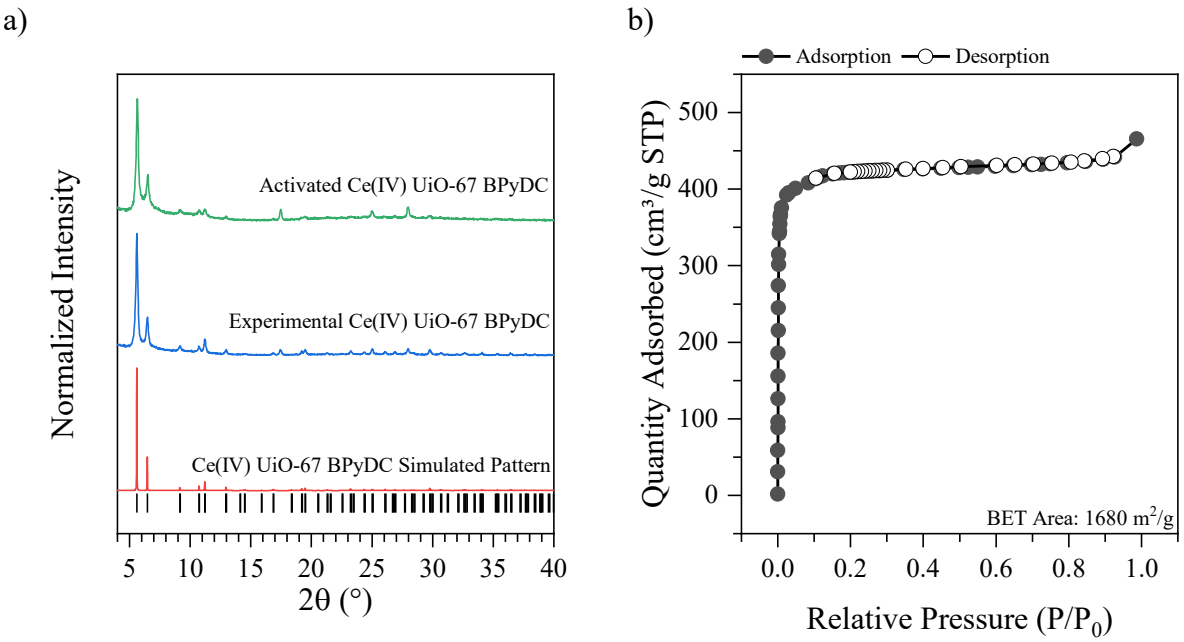

Figure 2.6: PXRD pattern of as-synthesized and activated Ce(IV)-UiO-67-BPyDC (a) and N_2 gas adsorption-desorption isotherm and BET area of Ce(IV)-UiO-67-BPyDC (b).

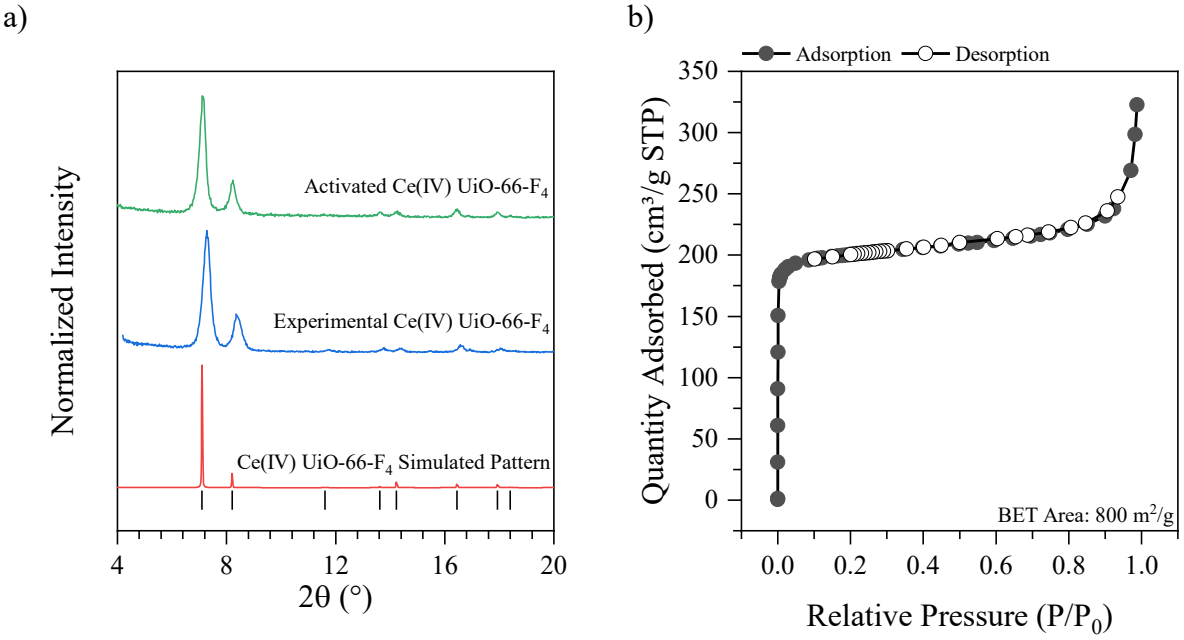

Figure 2.7: PXRD pattern of as-synthesized and activated Ce(IV)-UiO-66-F_4 (a) and N_2 gas adsorption-desorption isotherm and BET area of Ce(IV)-UiO-66-F_4 (b).

To measure the BET area and characterize the porosity of the materials, N_2 gas adsorption-desorption isotherms were measured after vacuum activation. Vacuum activation of the *de novo* synthesized MOFs was performed for 16 or 20 hours at 80, 100, 120, 130, or 140 °C depending on the material (see section 2.2.2 to 2.2.5 for details). The N_2 gas adsorption-desorption isotherms (Figures 2.3b, 2.4b, 2.5b, 2.6b, and 2.7b) are Type Ia isotherms characteristic of the low relative pressure adsorption of N_2 into micropores.[173] The BET areas of the MOFs are observed to decrease with the presence of heavy and bulkier functional groups present on the linker, with the highest BET area for the original Ce(IV)-UiO-66 of 1120 m^2/g (Figure 2.3b) and the lowest of 600 m^2/g for the functionalized Ce(IV)-UiO-66-Br (Figure 2.4b). The largest surface area, as expected due to the longer length of the linker and larger pores was confirmed for Ce(IV)-UiO-67-BPyDC (Figure 2.6b) at 1680 m^2/g.

Calculating the volumetric BET area of the materials allows for the observation of the effect that the large Br and four F atoms have on the BET area (Table 2.1). The difference in volumetric BET area for the functionalized MOFs and Ce(IV)-UiO-66 indicates that regardless of increased weight of material, the BET area of the material decreases with the introduction of functional groups that protrude into the pore of the framework, although the differences are less pronounced than when considering only the gravimetric surface area. The N_2 gas adsorption-desorption isotherms for Ce(IV)-UiO-67-BPyDC were collected after extensive optimization of the vacuum activation procedure (Figure S.2.4). Vacuum activation yielded BET areas (Table 2.2) varying from as low as 12 m^2/g to 1680 m^2/g, the best of these was determined to be the literature method of 140 °C for 16 hours after soaking the sample in ethanol for 48 hours. After removing all the solvent and remaining guests in the MOF by vacuum activation, to ensure that the MOF had not collapsed, the PXRD patterns of the MOFs were collected again (Figures 2.3a, 2.4a, 2.5a, 2.6a, and 2.7a). These analyses show that post activation and N_2 gas adsorption-desorption analysis, Ce(IV)-UiO-66, Ce(IV)-UiO-66-Br, Ce(IV)-UiO-66-F, Ce(IV)-UiO-67-BPyDC, and Ce(IV)-UiO-66-F_4 all maintain a phase pure and crystalline structure. Decreases in crystallinity are noticed however, for Ce(IV)-UiO-66 (Figure 2.3a) and Ce(IV)-UiO-66-Br (Figure 2.4a) as the clear separation between reflections at 7 and 8 decreases when compared to the sample before activation.

Table 2.1: BET areas for a series of functionalized Ce(IV)-UiO-66 analogues calculated gravimetrically from N_2 gas adsorption-desorption isotherms and calculated per mole of material.

MOF	**BET Area by mass (m^2/g)**	**BET Area (m^2/cm^3)**	**MOF Density (g/cm^3)**
Ce(IV)-UiO-66	1120	695	0.620
Ce(IV)-UiO-66-Br	600	445	0.741
Ce(IV)-UiO-66-F	1000	646	0.646
Ce(IV)-UiO-66-F_4	800	578	0.723
Ce(IV)-UiO-67-BPyDC	1680	671	0.399
Ce(IV)-UiO-66-NH_2*	890	571	0.641

Table 2.2: BET areas calculated from a series of vacuum activation procedures for Ce(IV)-UiO-67-BPyDC

Vacuum Activation Method	**BET Area (m^2/g)**
40 °C for 24 hours	12
80 °C for 24 hours	670
40-100 °C for 24 hours with 10 °C/4 hours ramp	1 140
100 °C for 24 hours	970
120 °C for 16 hours	1 060
140 °C for 16 hours	440
140 °C for 16 hours with 48-hour ethanol soak	1 680

By performing post-synthetic modification on Ce(IV)-UiO-66, synthesis of Ce(IV)-UiO-66-NH_2 and Ce(IV)-UiO-66-$(OH)_2$ is possible. Solvent assisted linker exchange (SALE) starting from Ce(IV)-UiO-66 was performed in methanol with the addition of the incoming linker followed by vortexing and sonication.[124] The crystallinity and phase purity of the MOFs are maintained upon the analysis of the materials by PXRD when compared to the simulated patterns (Figure 2.8). Only N_2 gas adsorption-desorption of Ce(IV)-UiO-66-NH_2 was collected after vacuum activation as Ce(IV)-UiO-66-$(OH)_2$ was found to collapse upon vacuum activation.[124] Though further

exploration of alternate activation methods including supercritical CO_2 has not been documented for Ce(IV)-UiO-66-$(OH)_2$. The N_2 gas adsorption-desorption isotherm for Ce(IV)-UiO-66-NH_2 (Figure 2.9) was observed to be Type Ia, as expected for the microporous UiO-66 analogues. The BET area of Ce(IV)-UiO-66-NH_2 when calculated from the N_2 gas adsorption-desorption isotherms is 890 m^2/g, lower than the parent Ce(IV)-UiO-66. When the BET area per mole is calculated (Table 2.1) the area is larger than that of Ce(IV)-UiO-66-Br but smaller than that of Ce(IV)-UiO-66-F_4 After activation and N_2 gas adsorption-desorption the phase purity of Ce(IV)-UiO-66-NH_2 is maintained when the PXRD diffractogram (Figure 2.8a) is compared to the material before activation and after SALE.

a) b)

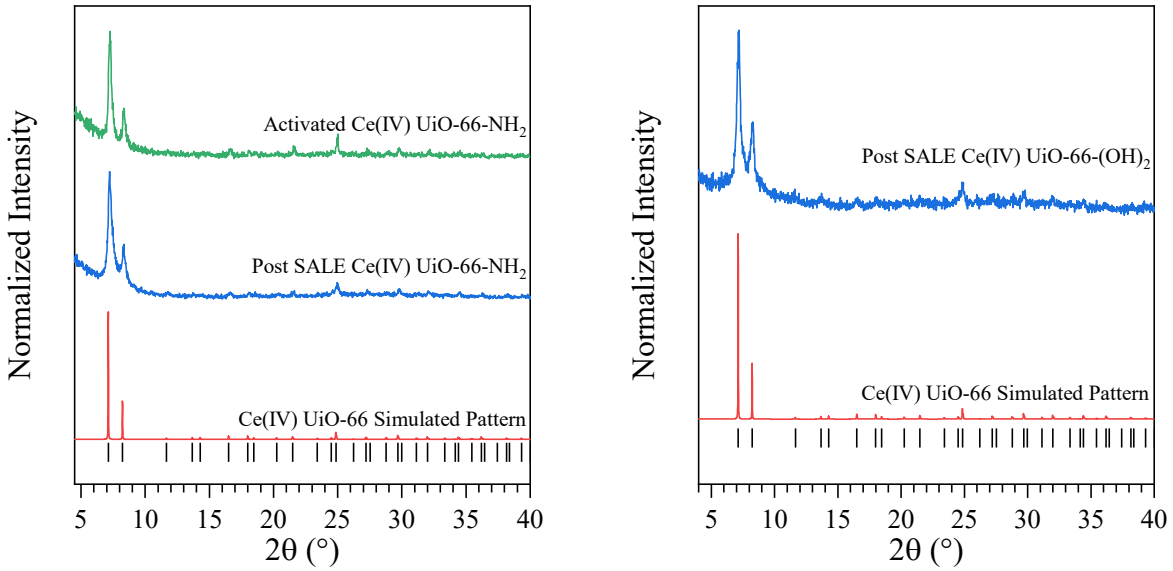

Figure 2.8: PXRD pattern of post SALE and activated Ce(IV)-UiO-66-NH_2 (a) and PXRD of post-SALE Ce(IV)-UiO-66-$(OH)_2$ (b).

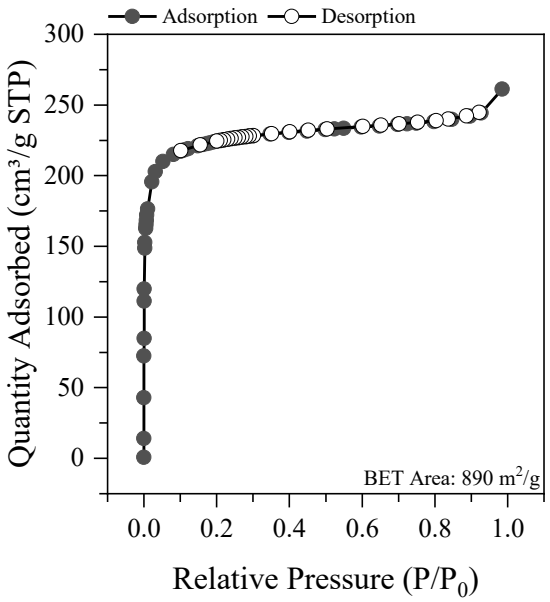

Figure 2.9: N_2 gas adsorption-desorption isotherm and BET area of Ce(IV)-UiO-66-NH_2.

The success of SALE in Ce(IV)-UiO-66 was determined by ^{1}H NMR spectroscopy. First, the chemical shifts associated with each proton were determined on each linker alone (Figures S.2.5, S.2.6, and S.2.7). For the aromatic H in BDC (Figure S.2.5) a chemical shift of 7.97 ppm is observed, similarly in NH_2BDC (Figure S.2.6) aromatic Hs appear at 7.97, 7.67, and 7.48 ppm. The ^{1}H NMR spectrum of Ce(IV)-UiO-66-NH_2 shown in Figure 2.10 indicates the presence of BDC and NH_2BDC in the MOF after SALE. In the case of the spectrum shown in Figure 2.10, there are 0.365 BDC per 1 NH_2BDC, or 2.74 NH_2BDC: 1 BDC. This quantization aligns with the average of SALE attempts performed. When performing SALE for a second time on the mixed linker sample generated from the first attempt, a linker ratio of 11 NH_2BDC:1 BDC was determined (Figure S.2.8).

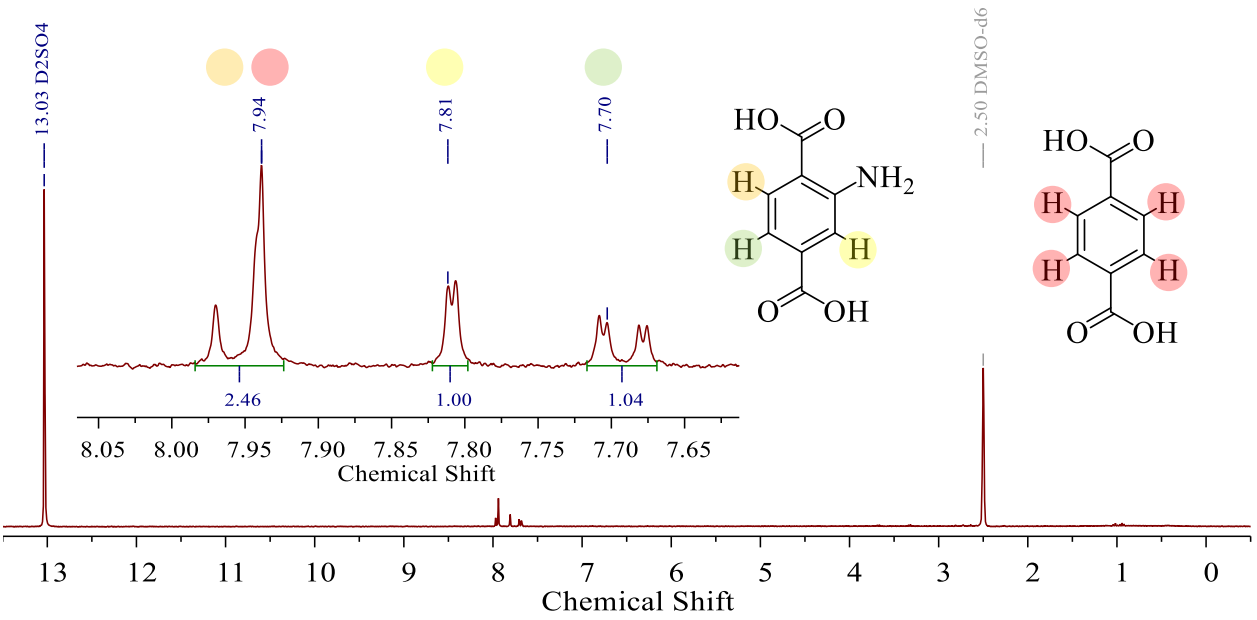

Figure 2.10: ^{1}H NMR spectrum of activated Ce(IV) UiO-66-NH_2 after SALE. The success of the SALE was calculated as 3 NH_2BDC: 1 BDC.

Similar to Ce(IV)-UiO-66-NH_2, the success of SALE for Ce(IV)-UiO-66-$(OH)_2$ was determined by ^{1}H NMR spectroscopy, however the peaks of the aromatic H in the BDC (Figure S.2.5) do not overlap with the aromatic H peaks in the DOBDC linker at 7.10 ppm (Figure S.2.7). In the case of the spectrum shown in Figure 2.11, the integration is normalized to the 2 protons of one DOBDC linker. The integral associated with BDC, when divided by 4 (due to the 4 protons per BDC) indicates the number of BDC linkers per 1 DOBDC linker. In Figure 2.11, this is calculated as 2.83 BDC per 1 DOBDC.

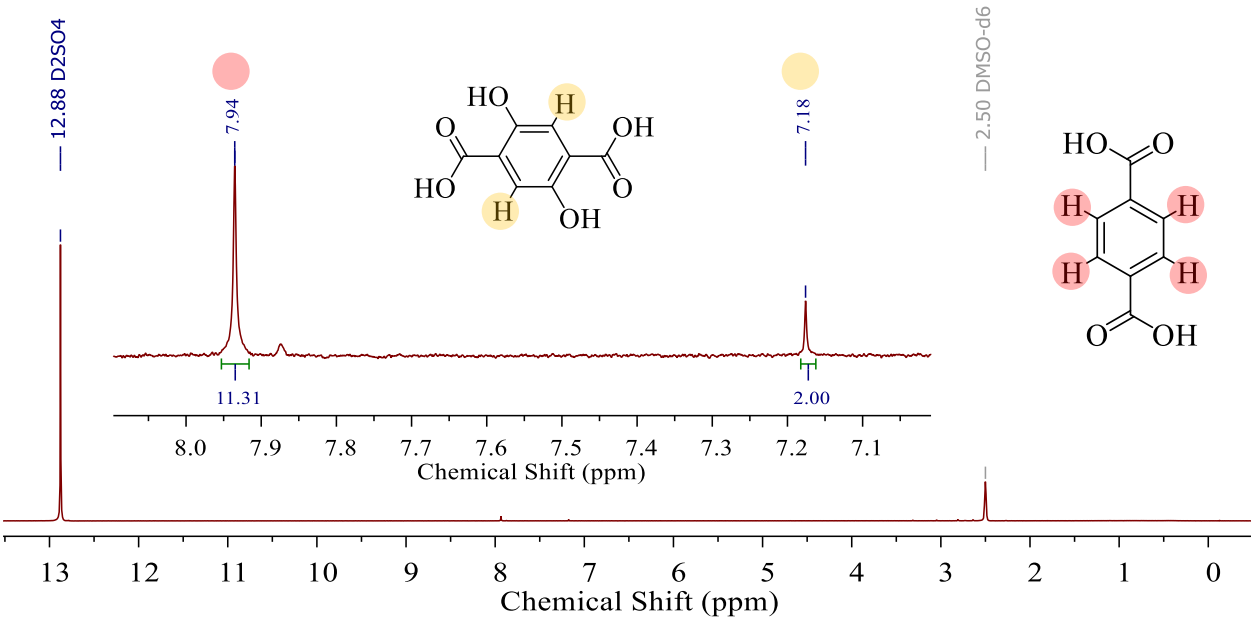

Figure 2.11: ^{1}H NMR spectrum of non-activated Ce(IV) UiO-66-(OH)$_2$ after SALE. The success of the SALE was calculated as 3 BDC: 1 DOBDC.

When comparing the success of two sequential SALE attempts, it is likely that SALE with NH$_2$BDC is more successful as it yields a more thermodynamically stable MOF. As SALE occurs due to the increased stability of exchanging some of the BDC linker for others, it is likely that the exchange of BDC for DOBDC is less thermodynamically stable. The decreased stability of the Ce(IV)-UiO-66-(OH)$_2$ has been shown upon vacuum activation,[124] while Ce(IV)-UiO-66-NH$_2$ maintains is crystallinity after vacuum activation (Figure 2.8a).

^{1}H NMR spectroscopy is not only used to determine the success of the SALE in Ce(IV)-UiO-66 MOFs, but also to confirm the success of the synthesis of the *de novo* synthesized MOFs. ^{1}H NMR spectra for digested samples of Ce(IV)-UiO-66, Ce(IV)-UiO-66-Br, Ce(IV)-UiO-66-F, and Ce(IV)-UiO-67-BPyDC are shown in Figures 2.12, 2.13, 2.14, and 2.15 and indicate successful assembly of the functionalized and parent MOFs. The ^{1}H NMR spectrum of Ce(IV)-UiO-66 (Figure 2.12) indicates only one type of H in the material at 7.95 (singlet) ppm. For Ce(IV)-UiO-66-Br, (Figure 2.13) three different types of aromatic Hs are observed at 8.15 (singlet), 8.03 (doublet), and 7.87 (doublet) ppm, all at relatively equivalent integrations indicating their equal quantities throughout the material. The additional peaks at 2.81 and 2.64 ppm are indicative of DMF leftover from the synthesis Analysis of the ^{1}H NMR spectrum of Ce(IV)-UiO-66-F (Figure

2.14) indicates the successful synthesis of the MOF, with aromatic Hs present with nearly equal integrals at 8.00 (triplet), 7.87 (doublet), and 7.76 (doublet). Presence of DMF leftover from the synthesis is indicated by the peaks at 2.81 and 2.64 ppm. DMF is present in the ^{1}H NMR spectrum of Ce(IV)-UiO-67-BPyDC (Figure 2.15) as well, which also confirms a successful synthesis. The minimal electronic difference between aromatic C and N cause the two Hs opposite the C-N aromatic bonding to overlap in the spectrum at ~8.65 ppm leading to an integral twice as large as that of the H immediately adjacent to the N which appears at 9.12 ppm. An ^{1}H NMR spectrum for Ce(IV)-UiO-66-F$_4$ was obtained (Figure S.2.9), and the absence of Hs confirms the presence of only the F$_4$BDC linker in the MOF.

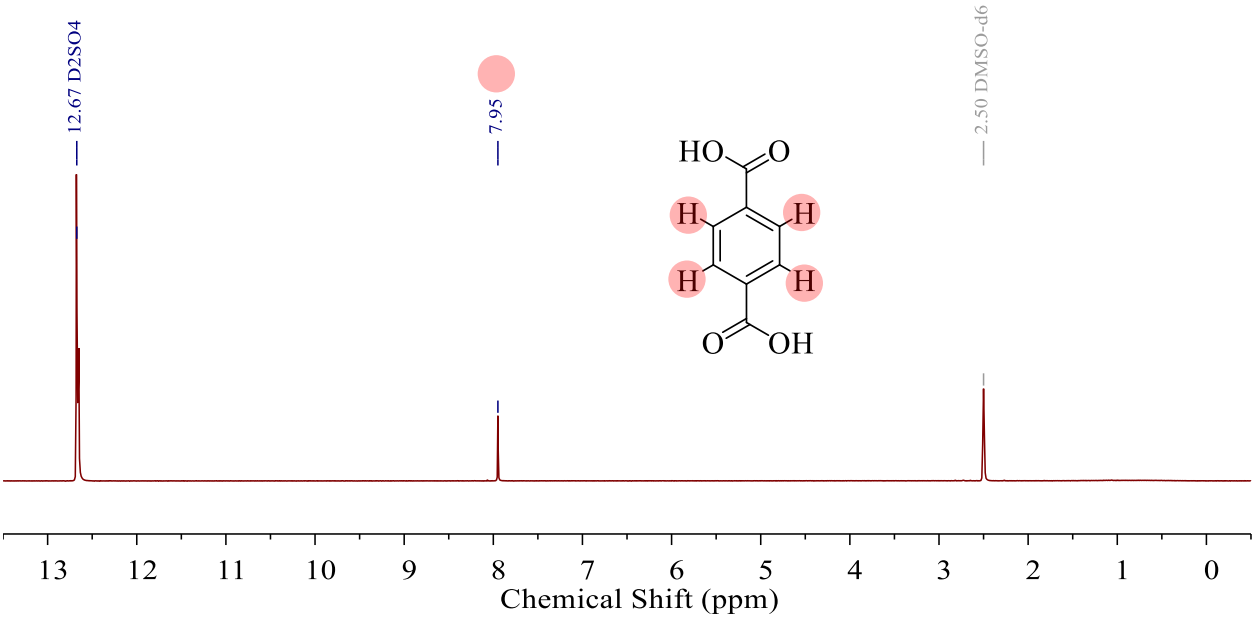

Figure 2.12: ^{1}H NMR spectrum of activated Ce(IV)-UiO-66, aromatic H at 7.95 ppm.

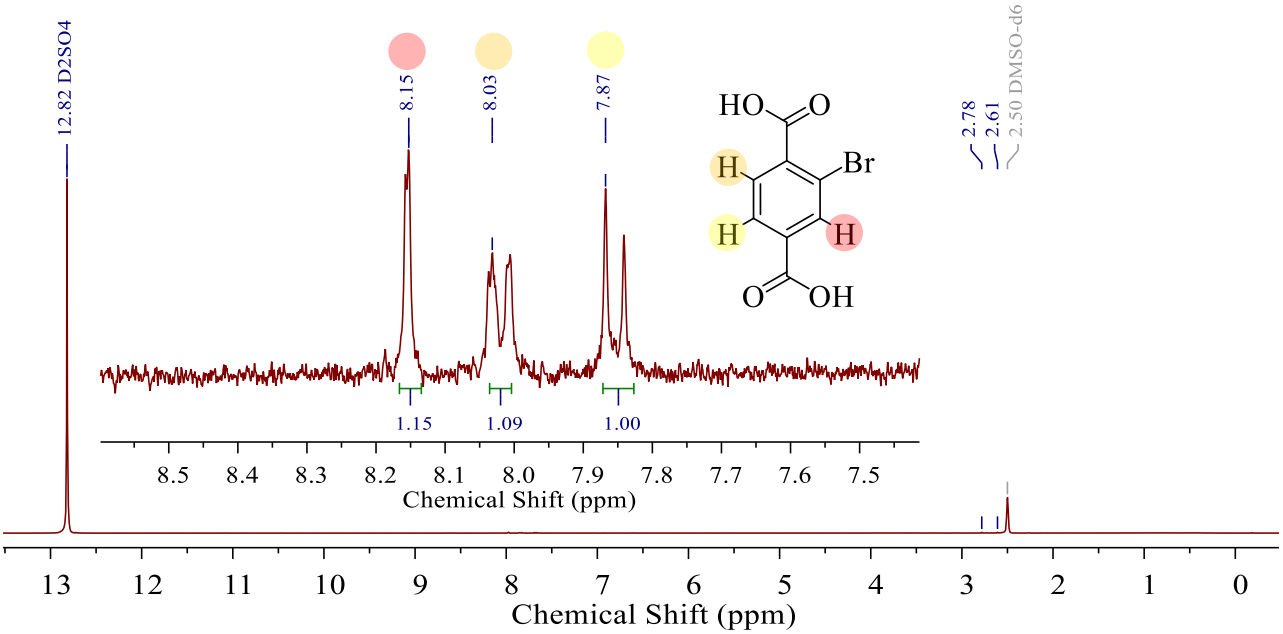

Figure 2.13: ^{1}H NMR spectrum of non-activated Ce(IV)-UiO-66-Br, aromatic H all integrating equivalently to ~1 at 8.15, 8.03, and 8.78 ppm, peaks present at 2.78 ppm and 2.61 ppm are indicative of remaining DMF present in the MOF.

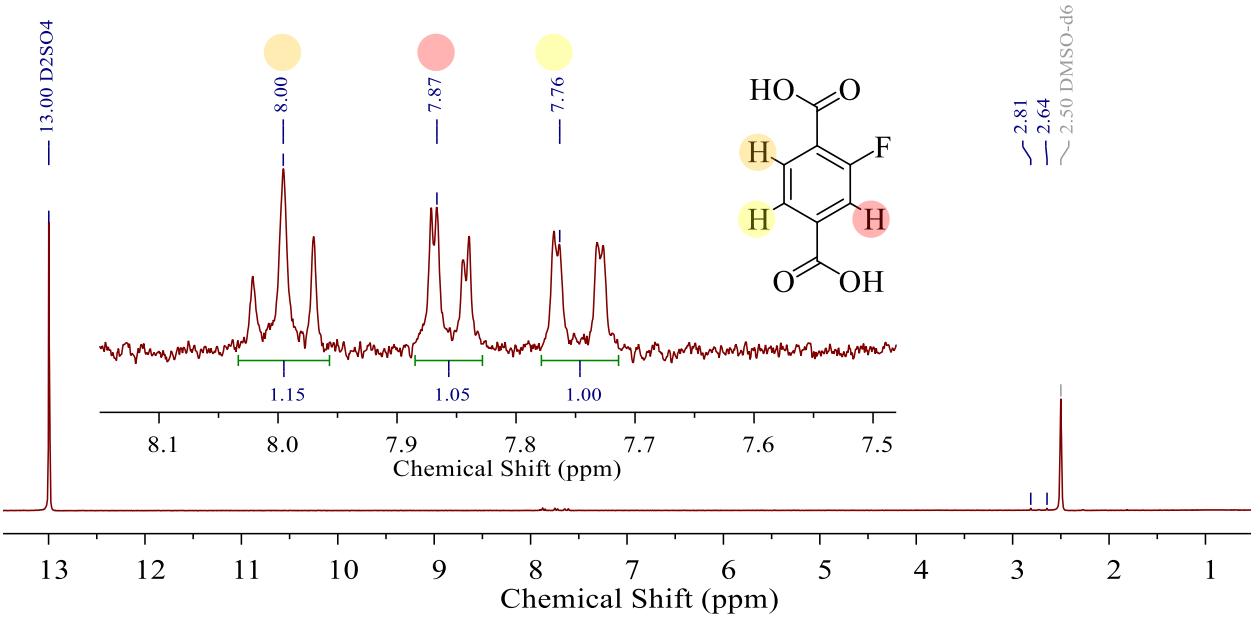

Figure 2.14: ^{1}H NMR spectrum of non-activated Ce(IV)-UiO-66-F, aromatic H are indicated at 8.00, 7.87, and 7.76 ppm. Peaks present at 2.81 ppm and 2.64 ppm are indicative of remaining DMF present in the MOF.

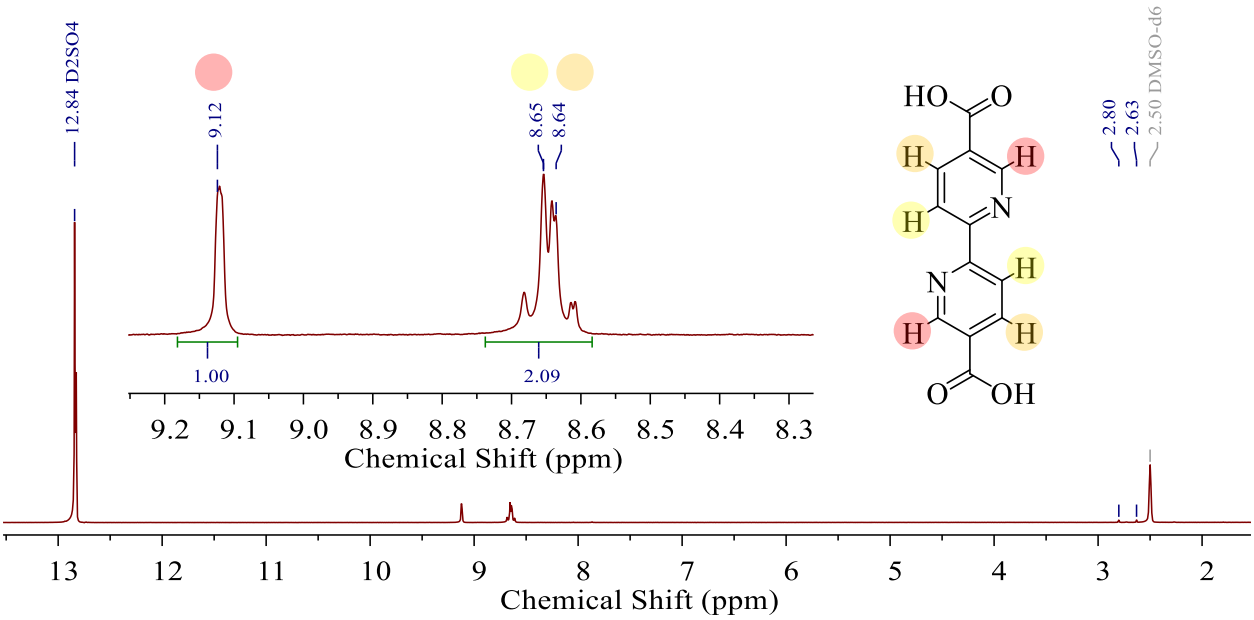

Figure 2.15: ^{1}H NMR spectrum of non-activated Ce(IV)-UiO-67-BPyDC, aromatic H from the BPyDC linker are indicated at 9.12, 8.65, and 8.64 ppm. Peaks present at 2.80 ppm and 2.63 ppm are indicative of remaining DMF present in the MOF.

Analysis of the IR active functional groups present in the MOFs was carried out by DRIFTS, shown in Figures 2.16, 2.17, 2.18, and 2.19. The stretch associated with O-H groups present in the hexanuclear cluster is shaded in blue for each MOF and appears at approximately 3 700 cm^{-1}. In the DRIFTS spectra of Ce(IV)-UiO-66 (Figure 2.16a), Ce(IV)-UiO-66-F (Figure 2.17a), Ce(IV)-UiO-66-F_4 (Figure 2.17b), Ce(IV)-UiO-66-NH_2 (Figure 2.18a), and Ce(IV)-UiO-67-BPyDC (Figure 2.19) this stretch is indicated by a single peak confirming the presence of only one type of O-H in the structure in the Ce(IV) clusters, the bridging μ_3-OH. While in Ce(IV)-UiO-66-Br (Figure 2.16b) and Ce(IV)-UiO-66-$(OH)_2$ (Figure 2.18b) the stretch is broader, indicating the presence of a variety of O-H moieties present in the MOFs such as bridging μ_3-OH and terminal –OH and –OH_2 ligands. This could be indicative of defects in the material or solvents present in the pores of the MOF.

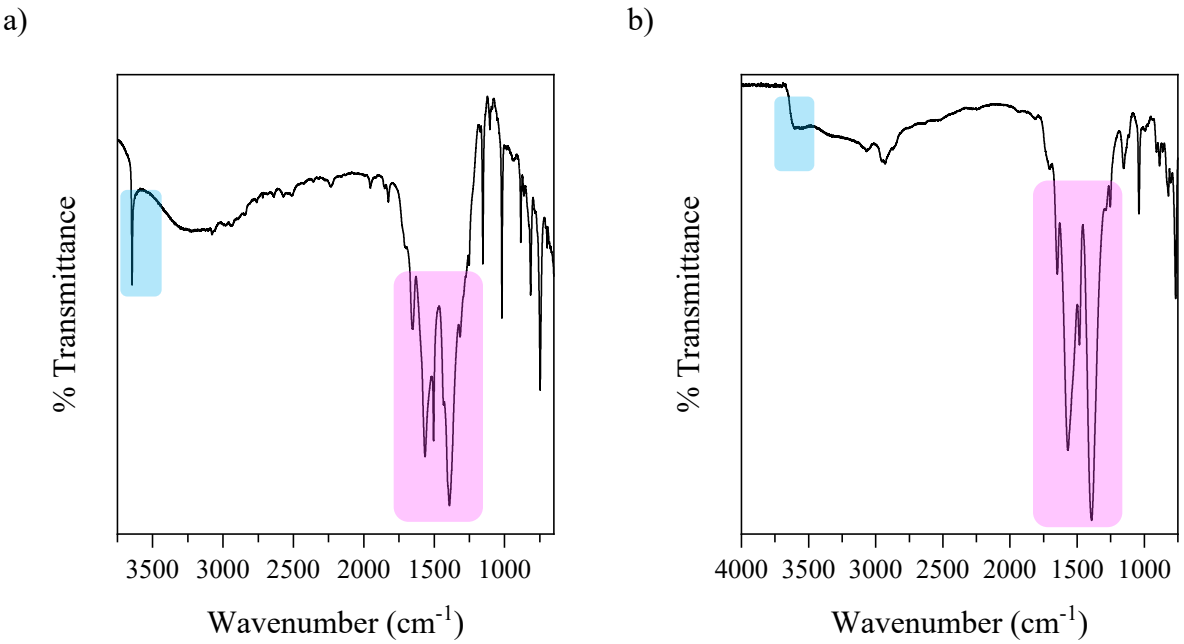

Figure 2.16: DRIFTS spectrum of activated Ce(IV)-UiO-66 (a) and activated Ce(IV)-UiO-66-Br (b). The light blue shading indicates the O-H bond stretch and pink indicates the C=O bonding.

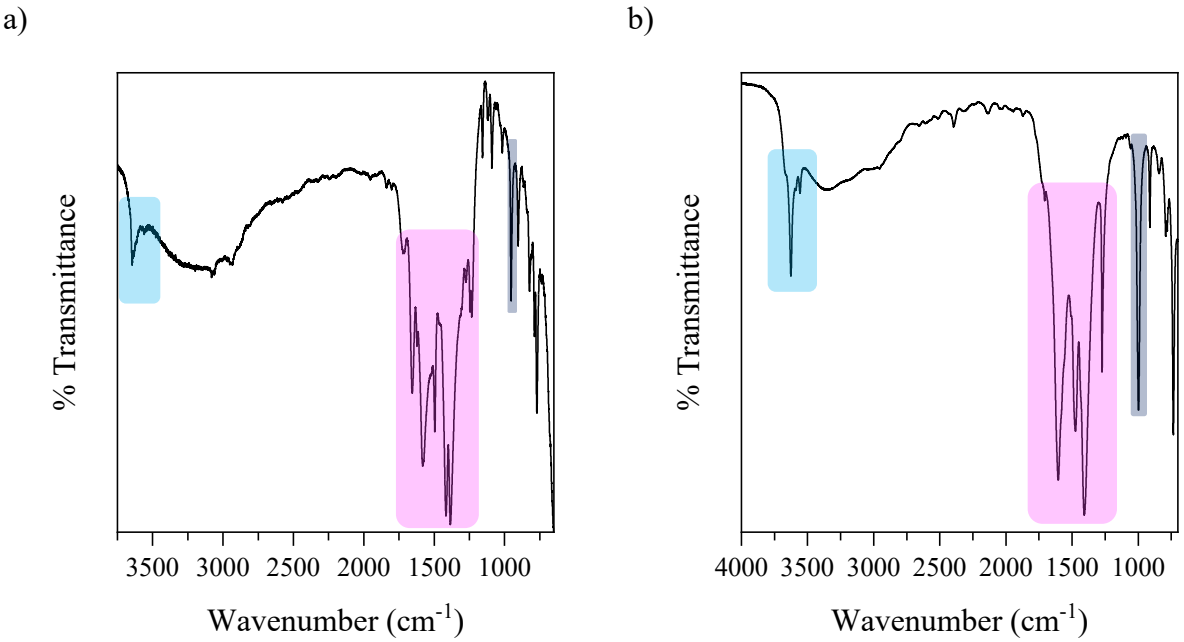

Figure 2.17: DRIFTS spectrum of activated Ce(IV)-UiO-66-F (a) and activated Ce(IV)-UiO-66-F_4 (b). The light blue shading indicates the stretch from the O-H bonds, pink indicates the C=O stretches, and the dark blue indicates the C-F stretch.

In addition to the O-H stretch, further stretches observed in all MOFs include C=O stretching at ~1600 cm^{-1}. These stretches are indicated in each spectrum (Figure 2.16, 2.17, 2.18 and 2.19) by pink shading. These stretches confirm the presence of carbonyl C=O bonds in the structures, this is expected due to the C=O bonding present in each linker. In the case of Ce(IV)-UiO-67-BPyDC (Figure 2.19) the presence of aromatic C=N bonds is indistinguishable from the multitude of stretches present from the C=O bonds. Additional IR active peaks are present in the DRIFTS spectrum of Ce(IV)-UiO-66-F (Figure 2.17a) and Ce(IV)-UiO-66-F_4 (Figure 2.17b), corresponding to the C-F bonds. The presence of a sharp stretch at ~1000 cm^{-1} indicates the presence of C-F bonds and these stretches are indicated by dark blue shading.

DRIFTS can also be used to confirm the success of SALE for the synthesis of Ce(IV)-UiO-66-NH_2 (Figure 2.18a). The presence of two stretches at ~3350 cm^{-1} is characteristic of the two N-H bonds in primary amines, indicated by purple shading. These stretches confirm the successful exchange of some BDC with NH_2BDC.

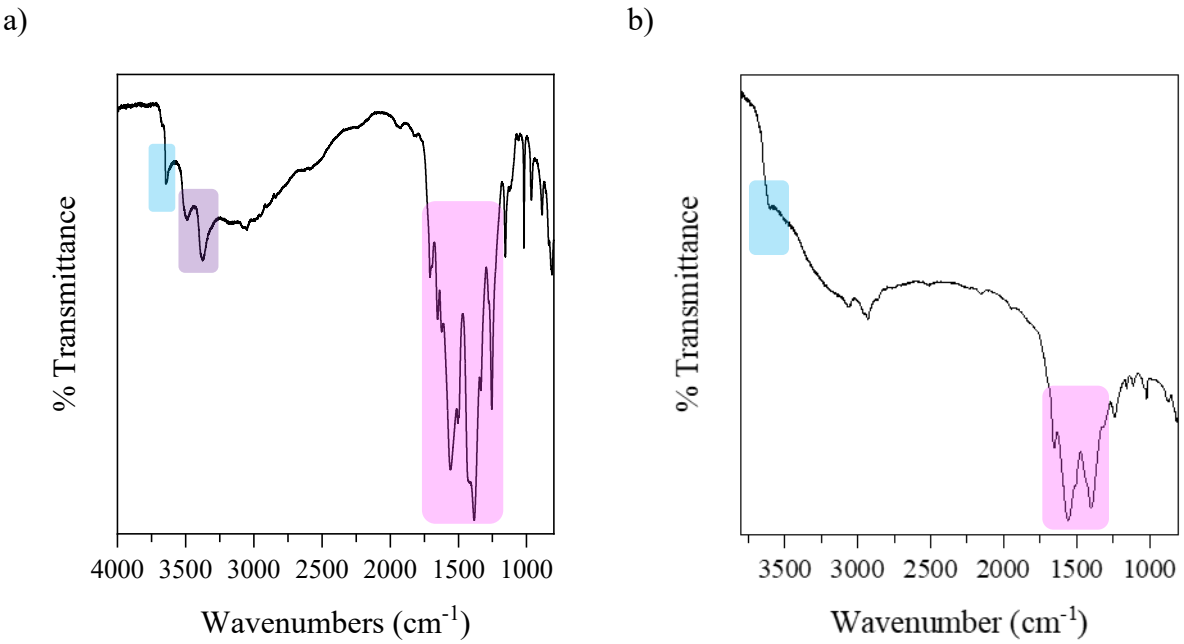

Figure 2.18: DRIFTS spectrum of activated Ce(IV)-UiO-66-NH_2 (a) and Ce(IV)-UiO-66-$(OH)_2$ (b). The light blue shading indicates the stretch from the O-H bonds, purple indicates the N-H stretching characteristic of 1º amines, and the pink indicates the C=O stretching.

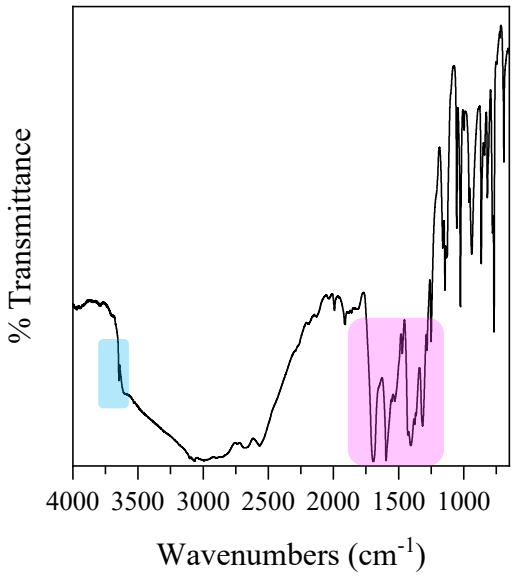

Figure 2.19: DRIFTS spectrum of activated Ce(IV)-UiO-67-BPyDC. The light blue shading indicates the stretch from the O-H bonds and the pink indicates the carbonyl C=O and aromatic C=N stretches.

To determine the thermal decomposition temperature and stability of the series of Ce(IV)-MOFs the materials were analyzed by thermogravimetric analysis (Figure 2.20, 2.21, and 2.22). The first decrease in mass occurs at 100 °C and is attributed to water in the material. As the temperature continues to increase the MOFs begin to degrade. This degradation is indicated by a large decrease in the mass of the material. The decomposition temperature was approximated from each TGA analysis and is summarized in Table 2.3. The thermal degradation temperature of each MOF indicates the strength of the bonding between the linker and the cluster and within the cluster itself. These results indicate that all of the functionalized MOFs are more thermally stable than the parent MOF, and Ce(IV)-UiO-67-BPyDC has the highest thermal stability with a degradation temperature of 310 °C.

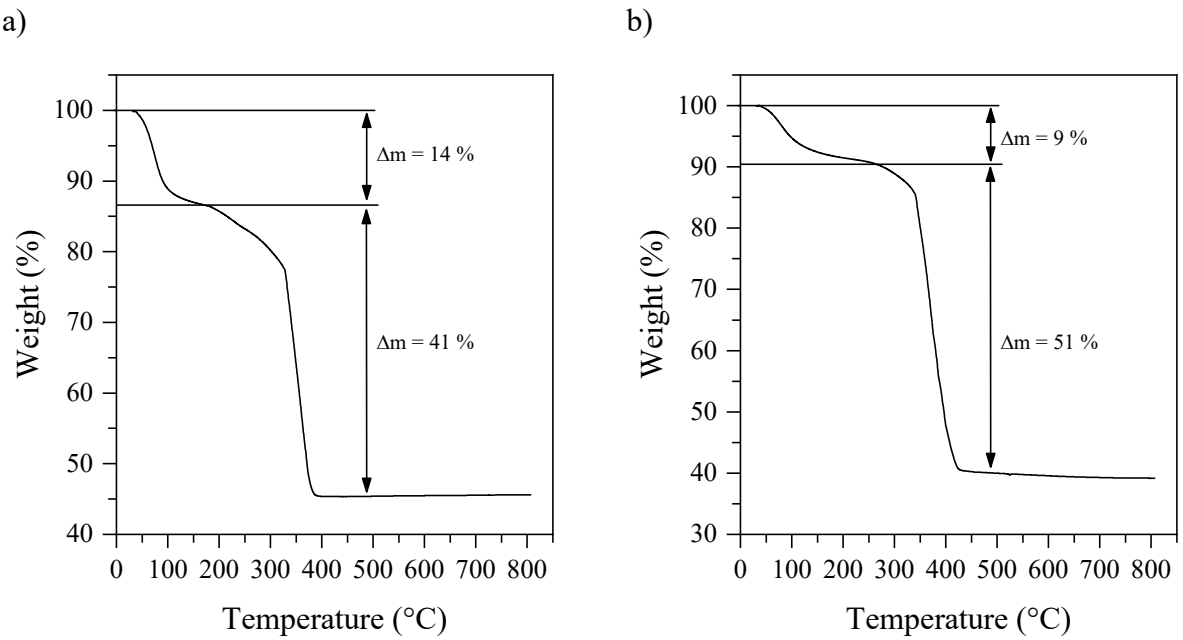

Figure 2.20: TGA of activated Ce(IV)-UiO-66 (a) and activated Ce(IV)-UiO-66-Br (b).

a) b)

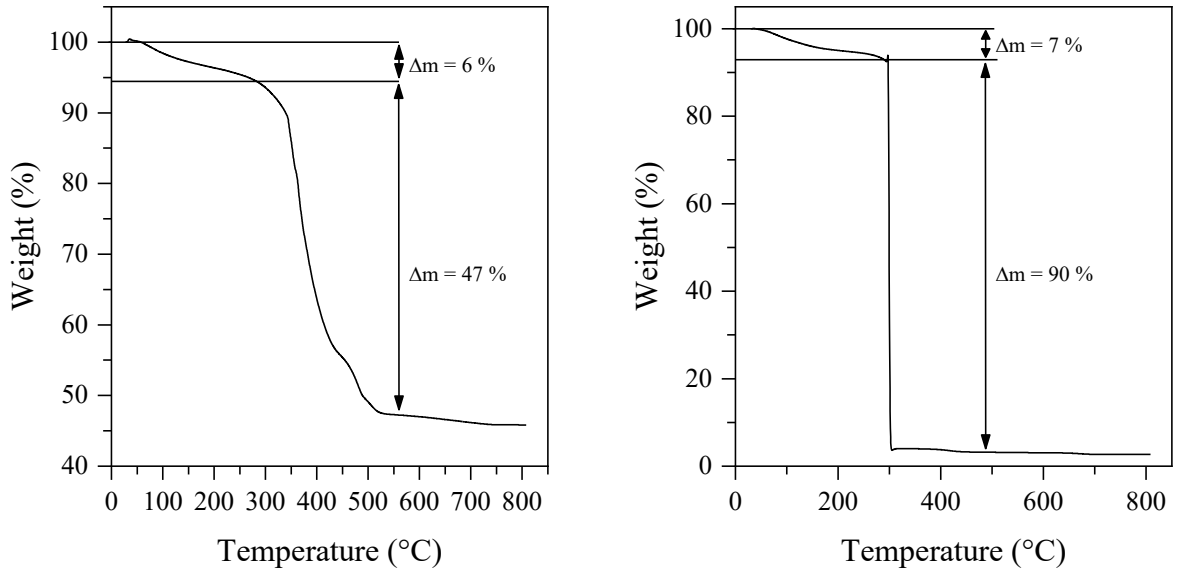

Figure 2.21: TGA of activated Ce(IV)-UiO-66-F (a) and activated Ce(IV)-UiO-66-F_4 (b).

a) b)

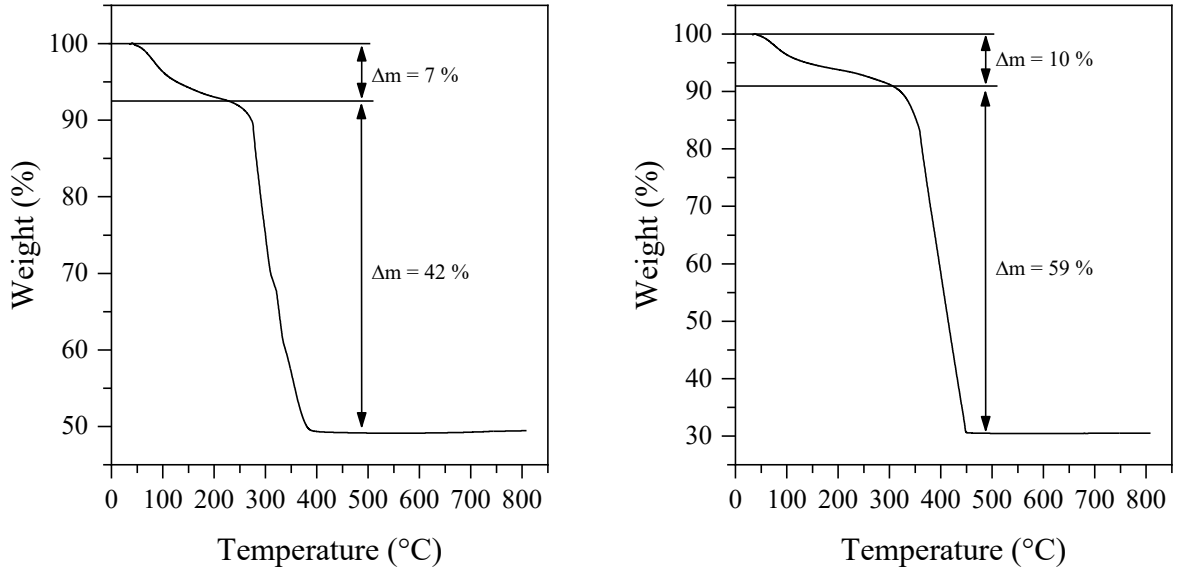

Figure 2.22: TGA of activated Ce(IV)-UiO-66-NH_2 (a) and activated Ce(IV)-UiO-67-BPyDC (b).

Table 2.3: Degradation temperatures for the series of Ce(IV)-UiO-66/67 analogues.

MOF	**Degradation Temperature (°C)**
Ce(IV)-UiO-66	200
Ce(IV)-UiO-66-Br	270
Ce(IV)-UiO-66-F	290
Ce(IV)-UiO-66-F_4	290
Ce(IV)-UiO-66-NH_2	230
Ce(IV)-UiO-67-BPyDC	310

Based on the characterization of the series of Ce(IV)-UiO-66 and Ce(IV)-UiO-67 analogues, we can determine that the MOFs were successfully synthesized and all materials maintain crystallinity after activation. The successful synthesis and characterization of all of these materials allows for accurate comparisons of the electrochemical characteristics of all the Ce(IV)-UiO-66 and Ce(IV)-UiO-67 analogues.

2.4. Electrochemical Results

The electrochemical properties of the Ce(IV)-UiO-66 and Ce(IV)-UiO-67 analogues were determined using cyclic voltammetry. After characterization the MOFs were prepared as described in section 2.2.6. Thin films were then connected to the biopotentiostat by the metal alligator clips wired to the instrument and scanned first in the anodic direction after an induction period at 0 V for 2-5 minutes. The induction period was performed to aid in the reduction of Ce(IV) to Ce(III) in the MOF with the hope of increasing the amount of Ce(III) on the electrode and thus increasing the current observed in the oxidation wave that occurs in the first segment of the scan. Due to the insulating nature of MOFs, the collection of CV data is quite challenging, as the electron transport required to measure the current increase that occurs with oxidation or reduction is not possible in an insulator. As such, it is expected that only a very small layer of the MOF, closest to the electrode surface, is electrochemically addressable. A summation and comparison of the reduction potentials of Ce(IV) in each MOF is described, characterized, and compared.

The voltammogram of Ce(IV)-UiO-66 (Figure 2.23a) was collected in 0.1 M Na_2SO_4 in water from a starting potential of 0.24 V, with a minimum of 0.23 V and a maximum of 1.44 V.

As the potential increases anodically the current increases and the voltage reaches to near the edge of the solvent window of the electrolyte (1.23 V at 25 °C).[196] A further increase in current is observed at ~ 1 V, which indicates the oxidation of Ce(III) to Ce(IV). While this small wave does indicate that oxidation is occurring, due to the overlap with the solvent window it is not possible to quantify the oxidation potential of the Ce(IV)-UiO-66. When the voltammogram then scans in the cathodic direction a clearly resolved reduction wave is observed at 0.62 V. The shape of this wave is not characteristic of a solution based voltammogram, indicating that the reduction is occurring in the solid MOF material, and thus the diffusion of ions throughout the solution as described by Nernst is not relevant. This oxidation and reduction pattern was confirmed in all 3 cycles performed (Figure S.2.11a).

The voltammogram of Ce(IV)-UiO-66-Br (Figure 2.23b) was collected in 0.1 M Na_2SO_4 in water from a starting potential of 0.50 V, with a minimum and maximum potential of 0.48 V and 1.24 V respectively. In the anodic sweep an oxidative wave is observed at 1.11 V, and in the cathodic sweep a reductive wave is observed at 0.87 V. The anodic sweep shows a Nernstian peak characteristic of diffusion associated with solution phase voltammograms, while the reductive peak is more characteristic of a solid state voltammograms. The observed reduction and oxidative potentials are confirmed in each of the three cycles of the CV, as shown in Figure S.2.11b. When compared to the non-functionalized Ce(IV)-UiO-66 there is a clear increase in the reduction potential, indicating more energy is required to undergo oxidation and reduction for the MOF with the bromine functionalized linker.

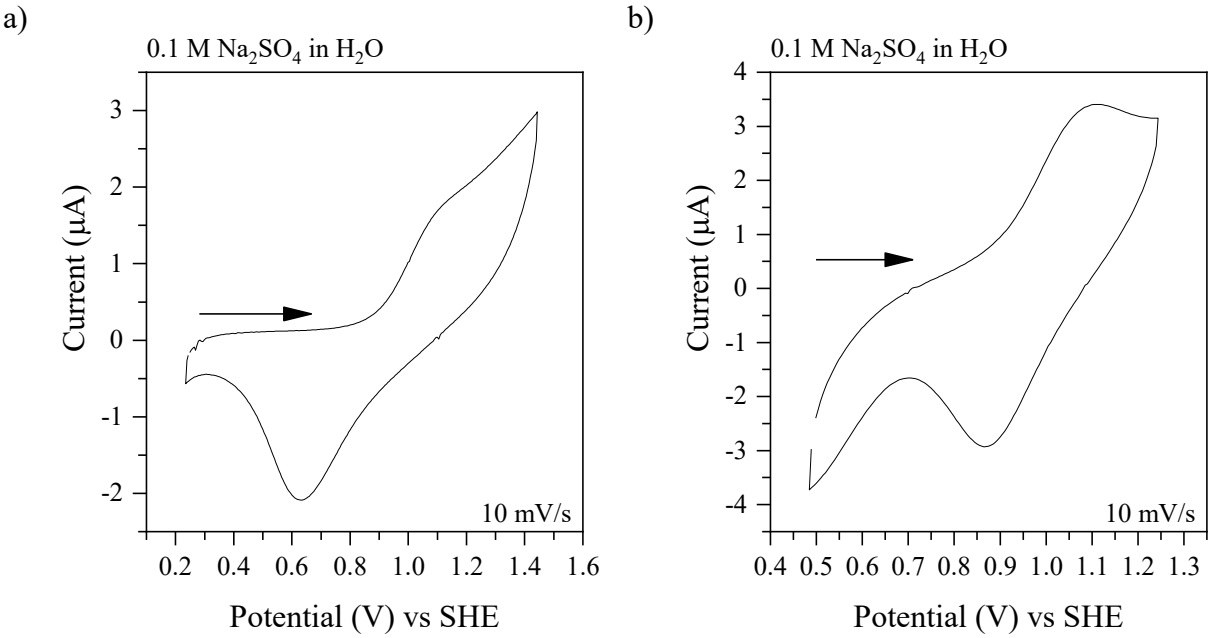

Figure 2.23: Cyclic voltammograms collected on dropcast samples of activated Ce(IV)-UiO-66 (a) and activated Ce(IV)-UiO-66-Br (b) on FTO.

The electrochemical characterization of Ce(IV)-UiO-66-F (Figure 2.24a) was performed in 0.1 M Na_2SO_4 in water starting from 0.24 V with a minimum and maximum of 0.23 V and 1.44 V. The voltammogram with all 3 cycles is shown in Figure S.2.12a. In both the anodic and cathodic sweeps of the voltammogram, an oxidation and reduction are observed, respectively. The oxidation of Ce(III) at 1.10 V is indicative of a solution based Nernstian ion diffusion, while the reductive peak at 0.85 V is indicative of a non-Nernstian solid state voltammogram. The appearance of the oxidative peak as a solution-based peak is concerning as it may indicate that the Ce ions are leaching out of the MOF into the solution. As such, a voltammogram with a clean electrode was recorded immediately after the voltammogram of Ce(IV)-UiO-66-F in the same electrolyte solution. The voltammogram collected, shown in Figure S.2.13 indicates that Ce is not leaching into the solution, as there is no reduction or oxidation occurring in the electrolyte after CV of Ce(IV)-UiO-66-F.

The voltammogram of Ce(IV)-UiO-66-F_4 (Figure 2.24b) was collected in 0.1 M Na_2SO_4 in water from a starting potential of 0.84 V, with a minimum and maximum potential of 0.83 V and 1.44 V. In the anodic sweep an oxidative peak occurs at 1.25 V, though is barely distinguishable as it accompanies a general increase in current as the potential approaches the edge

of the solvent window. As the CV is swept in the cathodic direction a reductive peak is observed at 1.00 V, the highest observed for any of the analogues. Due to the height of the peaks relative to the baseline, it is not possible to define whether the peak is indicative of a solution or solid-state electron transfer event. The oxidation and reduction peaks noted here are confirmed in the full CV showing all three cycles (Figure S.2.12b). For both the Ce(IV)-UiO-66-F and Ce(IV)-UiO-66-F_4 an increase in the energy required for reduction is observed when compared to Ce(IV)-UiO-66. The presence of four fluorine atoms in each linker in Ce(IV)-UiO-66-F_4 has the largest increase in reduction potential of any of the MOFs analyzed.

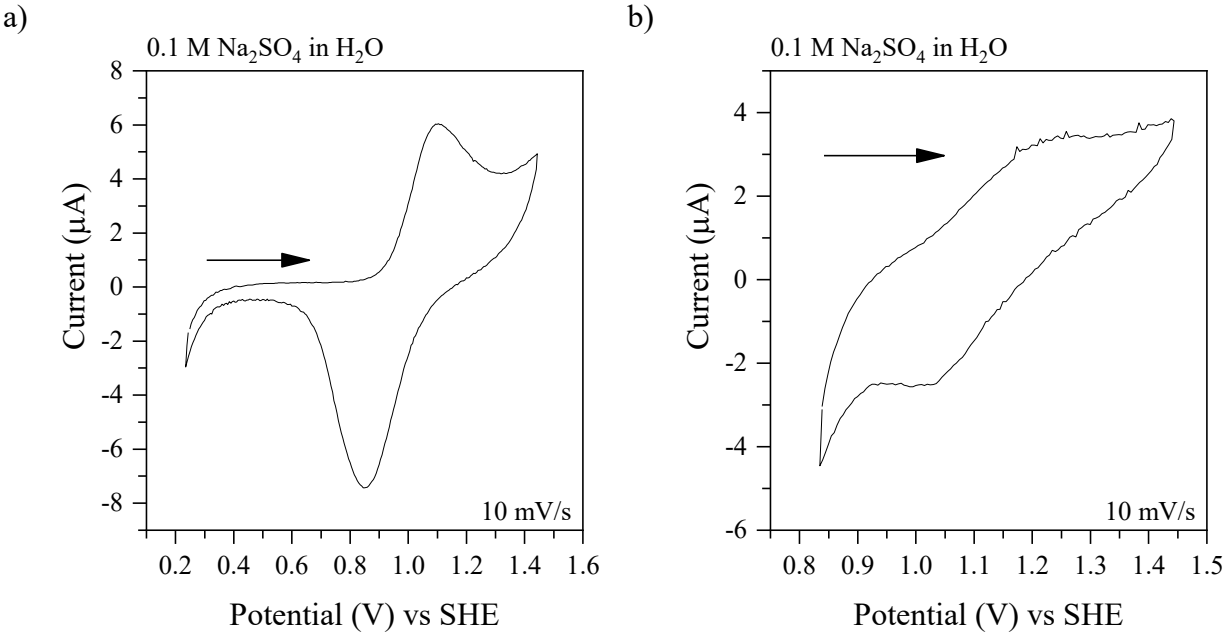

Figure 2.24: Cyclic voltammograms collected of drop cast activated Ce(IV)-UiO-66-F (a) and activated Ce(IV)-UiO-66-F_4 (b) onto FTO.

The CV of Ce(IV)-UiO-66-NH_2 (Figure 2.25a) was collected in 0.1 M $TBAPF_6$ in DCM from an initial potential of -0.07 V scanned anodically with a minimum and maximum of -0.32 V and 1.43 V. In the anodic scan an oxidative peak appears with a Nernstian diffusion after the maximum, with a maximum at 0.88 V. For the cathodic scan a reductive peak is observed at 0.52 V and appears to be a solution-based peak showing Nernstian diffusion after the minimum. Voltammograms including all three cycles confirmed the oxidation and reduction potentials and are shown in Figure S.2.14a.

The voltammogram of Ce(IV)-UiO-66-$(OH)_2$ (Figure 2.25b) was collected in 0.1 M $TBAPF_6$ in DCM from a starting potential of 0.07 V, with a minimum and maximum potential of 0.06 V and 1.47. In the anodic sweep the increase in current associated with an oxidation was observed at 1.10 V and appears to show a Nernstian diffusion decay after the maximum of the peak. In the cathodic sweep the reductive peak also indicates a solution-based reduction at 0.59 V. These events are confirmed in all three of the cycles (Figure S.2.14b). When the reduction potential for both Ce(IV)-UiO-66-NH_2 and Ce(IV)-UiO-66-$(OH)_2$ are compared to that of the non-functionalized Ce(IV)-UiO-66 both show a decrease in the energy required for reduction to occur, with the amino functionalized MOF indicating the lower reduction potential of all MOFs analyzed.

Both the voltammograms for Ce(IV)-UiO-66-NH_2 and Ce(IV)-UiO-66-$(OH)_2$ were collected using a 0.1 M $TBAPF_6$ in DCM electrolyte while the rest were analyzed in 0.1 M Na_2SO_4 in water. CV of Ce(IV)-UiO-66-NH_2 and Ce(IV)-UiO-66-$(OH)_2$ were attempted in 0.1 M Na_2SO_4 in water but no change in current was observed indicating no oxidation and reduction was occurring under the aqueous conditions. It is possible that the ability of these two functional groups to act as hydrogen bond donors and acceptors and thus form stabilizing interactions with the water may inhibit the movement of the ions through the MOF. This would make the current associated with the oxidation or reduction in these materials immeasurable.

a)

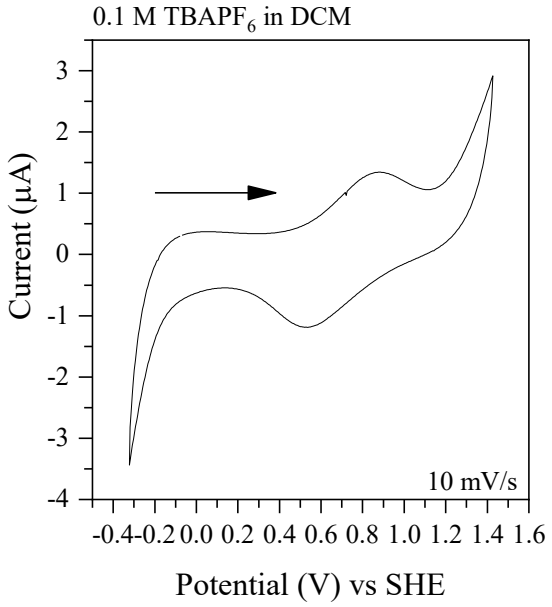

b)

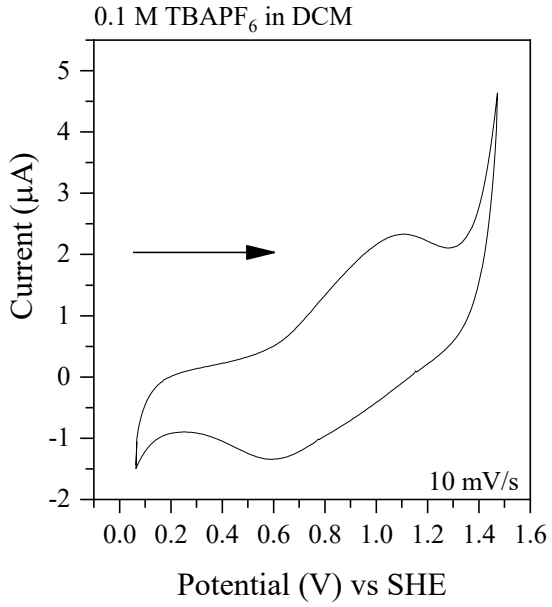

Figure 2.25: Cyclic voltammograms collected of drop cast activated Ce(IV)-UiO-66-NH_2 (a) and non-activated Ce(IV)-UiO-66-$(OH)_2$ (b) onto FTO.

The electrochemical analysis of Ce(IV)-UiO-67-BPyDC was performed by CV in 0.1 M Na_2SO_4 in water with an initial potential of 0.24 V with a minimum and maximum of 0.23 V and 1.24 V as shown in Figure 2.26. In the anodic direction an oxidative peak occurs at 0.98 V and appears to be a solution-based peak, in cathodic scans a non-Nernstian solid state reductive peak occurs at 0.81 V. Voltammograms including the full three cycles of the CV are included in Figure S.2.15.

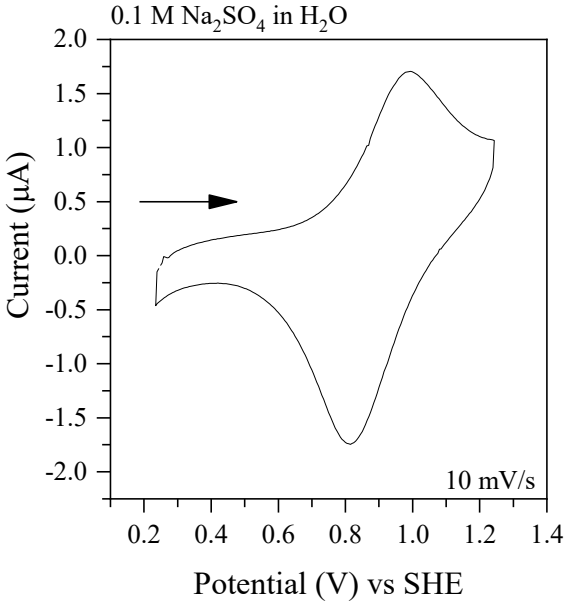

Figure 2.26: Cyclic voltammogram collected of drop cast samples of activated Ce(IV) UiO-67-BPyDC onto FTO.

Table 2.4: Reduction potentials of Ce(IV)-UiO-66 and Ce(IV)-UiO-67 analogues at 10 mV/s.

MOF	**Reduction Potential vs SHE (V)**	**Electrolyte**
Ce(IV)-UiO-66	0.62	0.1 M Na_2SO_4 in water
Ce(IV)-UiO-66-Br	0.87	0.1 M Na_2SO_4 in water

Ce(IV)-UiO-66-F	0.85	0.1 M Na_2SO_4 in water
Ce(IV)-UiO-66-F_4	1.00	0.1 M Na_2SO_4 in water
Ce(IV)-UiO-66-NH_2	0.52	0.1 M $TBAPF_6$ in DCM
Ce(IV)-UiO-66-$(OH)_2$	0.59	0.1 M $TBAPF_6$ in DCM
Ce(IV)-UiO-67-BPyDC	0.81	0.1 M Na_2SO_4 in water

While for all voltammogram presented an oxidative and reductive event occurred, in some samples the oxidative peak could not be quantified accurately. Thus, the potentials associated with the cathodic events are compared (Table 2.4). The absence of clear quantifiable oxidative peaks is not entirely unexpected as the material is synthesized with Ce(IV) and not Ce(III), thus reduction of Ce(IV) is required to occur during the induction period at the beginning of the CV experiment and before scanning in the anodic direction. Analysis of the reduction potentials of the Ce(IV)-UiO-66 and Ce(IV)-UiO-67 analogues indicates that the presence of electron withdrawing groups such as those in Ce(IV)-UiO-66-Br, Ce(IV)-UiO-66-F, and Ce(IV)-UiO-66-F_4 increase the reduction potential of the MOF. The increase in reduction potential indicates an increase in energy required for a redox event to occur. The opposite effect is observed for MOFs synthesized with linkers containing electron donating groups, Ce(IV)-UiO-66-NH_2 and Ce(IV)-UiO-66-$(OH)_2$, with the presence of two electron donating groups decreasing the reduction potential most. In the case of Ce(IV)-UiO-67-BPyDC the longer linker and aromatic N increase the energy required for reduction and oxidation to occur.

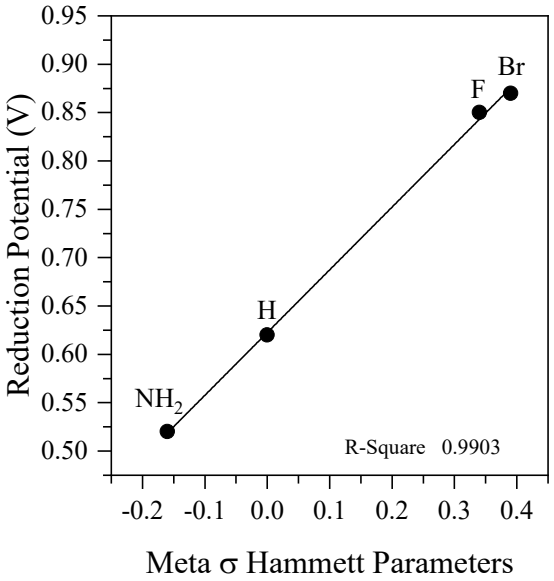

Figure 2.27: The linear relationship between the meta σ Hammett parameters and the measured reduction potential for the four monosubstituted Ce(IV)-UiO-66 derivatives.[197]

$$\log\left(\frac{K_a}{K}\right) = \sigma_a \rho$$

Equation 2.1: The simplified Hammett equation, where K_a is the equilibrium constant of the substituted benzene derivative, K is the equilibrium constant of the unsubstituted derivative, σ_a is the Hammett parameter for the give substituent, and ρ is the reaction constant for a given type of reaction.[198,199]

Comparing the measured reduction potentials for the MOFs comprised of monosubstituted linkers with the meta σ Hammett parameters for each functional group shows a linear trend, Figure 2.27.[197] The Hammett equation (Equation 2.1), was devised by Louis P. Hammett in 1937 to compare the effects of mono or para substitution of benzene derivatives with benzene and their effects on reaction equilibrium.[198,199] The meta σ parameters were used for comparison as the substituents used in the MOFs are meta to a carboxylate group, and the meta parameters allow for the isolation of the effects of the substituent group without introducing complications from steric effects, that would be required for analysis of ortho substituted groups. The linear relationship between the reduction potentials and the meta σ parameters confirms the observed effect that the

electron withdrawing or donating groups has on the reduction potentials for the MOFs composed of monosubstituted linkers or BDC.

2.5. Conclusion

All of the MOFs included in this series: Ce(IV)-UiO-66, Ce(IV)-UiO-66-Br, Ce(IV)-UiO-66-F, Ce(IV)-UiO-66-F_4, Ce(IV)-UiO-66-NH_2, Ce(IV)-UiO-66-$(OH)_2$, and Ce(IV)-UiO-67-BPyDC were successfully synthesized and characterized by PXRD, N_2 gas adsorption-desorption isotherms, ^{1}H NMR spectroscopy, DRIFTS, and TGA; with the exception of Ce(IV)-UiO-66-$(OH)_2$ which does not maintain crystallinity after vacuum activation.[122] After successful synthesis and characterization, the materials were characterized using CV. The voltammograms for the Ce(IV)-MOFs indicate quasireversible behavior for Ce(III/IV) present in the hexanuclear clusters nodes. The optimal conditions for CV for each material were determined, and the electrochemical results indicate a decrease in the energy required for oxidation and reduction in materials containing electron donating groups, Ce(IV)-UiO-66-NH_2 and Ce(IV)-UiO-66-$(OH)_2$. The presence of an aromatic N and an increase in the linker length or the presence of electron withdrawing groups in Ce(IV)-UiO-67-BPyDC, Ce(IV)-UiO-66-F, Ce(IV)-UiO-66-F_4, and Ce(IV)-UiO-66-Br, increase the amount of energy required for a redox electron transfer. Unfortunately, the conditions used to collect quantifiable voltammograms for Ce(IV)-UiO-66-NH_2 and Ce(IV)-UiO-66-$(OH)_2$ involve the use of a different electrolyte system then the rest of the MOFs and while all are measured relative to the SHE, the confirmation of the effects caused by the electron withdrawing groups, cannot be stated unequivocally do to this difference. No difference in voltammograms was observed between activated and not activated MOFs.

Chapter 3

Synthesis of Rare-Earth Cluster-Based Metal–Organic Frameworks using a Tetratopic Tetrathiafulvane Linker

3.1. Introduction

MOFs containing the TTF motif have been studied for a variety of potential applications including catalysis and applications where increasing the electrical conductivity of MOFs is required.[134,135] TTF is a particularly notable electron donor, and Ce(IV) has been studied extensively as an oxidation catalyst,[43] thus synthesis of a MOF that contains both Ce(IV) and TTF could be particularly useful for increasing conductivity via the redox hoping pathway (section 1.5) and subsequent catalysis.

Most MOFs that have been synthesized containing the TTFTBA linker are 2D (Figure 1.10), with structures that maximize the amount of π-π stacking between linkers, leading to increases in the conductivity of the MOFs via the through-space pathway (section 1.5). By comparison, very few 3D MOFs have been synthesized using the TTFTBA linker, and there are no TTFTBA MOFs reported with Ce(III/IV). The 3D MOFs that have been synthesized with the TTFTBA linker and rare-earth ions in the +3 oxidation state include those with **shp** topology (Figure 3.1), as synthesized by Su *et al.* (section 1.8.2) comprised of Y(III), Sm(III), Gd(III), Tb(III), Dy(III), Ho(III), or Er(III).[138] Another 3D MOF synthesized with TTFTBA is comprised of In(III) nodes and forms the **pts** topology.[200] This MOF was observed to be a flexible MOF in that it can transform structure while maintaining stability and integrity.[200] The structural transformation is based on the redox activity and the associated change to a planar configuration of the TTF motif.[200] Herein, unsuccessful attempts to synthesize Ce(IV) and Ce(III)-MOFs with the TTFTBA linker are discussed, and the successful synthesis of novel TTFTBA MOFs comprised of Lu(III) and Yb(III) nodes are reported.

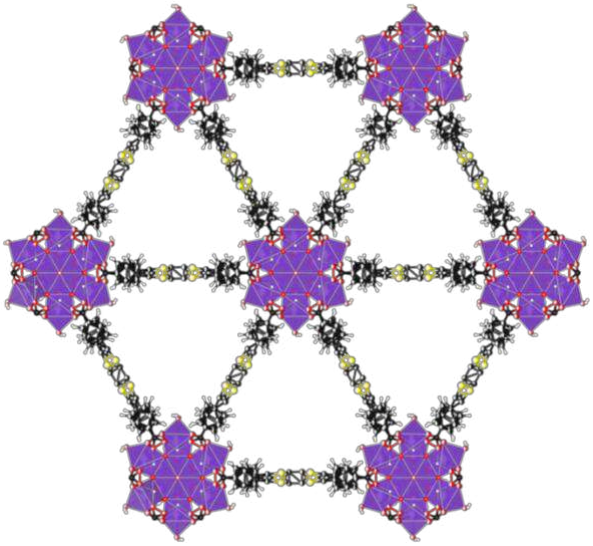

Figure 3.1: The Tb(III)-TTFTBA MOF with **shp** topology reported by Su *et al.*[138] The purple polygons are representative of the nonanuclear Tb(III)-cluster nodes, the black spheres are C, the white spheres are H, the yellow spheres are S, and the red spheres are O. The spheres with multiple colors and the multiple S, C, O, Tb, and H atoms are due to the disorder of the structure when solved from the SCXRD.

The synthesis of MOFs often requires the use of modulators (section 1.9.1), and in the case of RE(III) cluster-based MOFs fluorinated modulators are often used to generate and stabilize the RE(III)-cluster nodes *in situ*.[201] Unlike the cluster based MOFs, synthesis of MOFs composed of RE(III) chains is performed using strong acids such as nitric acid or sulfuric acid or using strong bases such as NaOH.[202–204] Cluster-based MOFs composed of Ce(IV) are more comparable to Zr(IV) MOFs due to there common oxidation state. The synthesis of many Ce(IV) cluster-based MOFs can often be performed without the use of a modulator or using formic or acetic acid, but not requiring a fluorinated modulator like RE(III) cluster-based MOFs.[99,128,151] Synthesis of MOFs composed of Ce(III) cluster nodes has not been accomplished *de novo*, only post synthetic reduction of the Ce(IV)-MOF-808 has yielded a Ce(III) hexanuclear cluster, indicating the difficulty of synthesizing a cluster-based Ce(III)-MOF.[115,116]

The synthesis and unsuccessful attempts at synthesis of 3D TTFTBA MOFs is presented herein with the RE metals Ce(III), Ce(IV), Yb(III), and Lu(III). All precipitates obtained are characterized by PXRD and compared to simulated patterns of reported 2D and 3D TTFTBA

MOFs. The novel Lu(III)-TTFTBA MOF with **shp** topology is further characterized by N_2 gas adsorption-desorption isotherms with BET calculations, DRIFTS, ^{1}H NMR spectroscopy, and ICP-MS.

3.2. Experimental Procedures

3.2.1. General Materials and Methods

All solvents and reagents were used without additional purification: N,N-dimethylformamide (DMF; C_3H_7NO, Fisher Chemical, ≥99.8%), 1,4-dioxane ($C_4H_8O_2$, Fisher Chemical, 99%), acetone (C_3H_6O, Fisher Chemical, 99.5%), tetrahydrofuran (THF; C_4H_8O, Fisher Chemical), methanol (CH_4O, Fisher Chemical, 99.8%), ethanol (C_2H_6O, Greenfield Global, 99%), ethyl acetate ($C_4H_8O_2$, Sigma Aldrich, ≥99.5%), dichloromethane (CH_2Cl_2, Sigma Aldrich, ≥99.5%), chloroform ($CHCl_3$, Fisher Chemical, 99.5%), deuterated chloroform ($CDCl_3$, Cambridge Isotope Laboratories, 99.8%), deuterated sulfuric acid (D_2SO_4, Sigma Aldrich, 96-98%), deuterated dimethyl sulfoxide (DMSO-d_6; C_2H_6OS, Cambridge Isotope Laboratories, 99.9%), acetic acid ($C_2H_4O_2$, Fisher Chemical, 99.7%), nitric acid (HNO_3, Fisher Chemical, 68-70 w/w%), trifluoroacetic acid (TFA; $C_2HF_3O_2$, Sigma Aldrich, 98%), hydrochloric acid (HCl, Fisher Chemical, 36 w/w%), 2-fluorobenzoic acid (FBA; $C_7H_5O_2F$, AmBeed, 98%), lutetium nitrate hydrate ($Lu(NO_3)_3 \cdot x(H_2O)$, Alfa Aesar, 99.99%), diammonium cerium(IV) nitrate ($(NH_4)_2Ce(NO_3)_6$, Fisher Chemical, 99.5%), cerium(III) nitrate hexahydrate ($Ce(NO_3)_3 \cdot 6(H_2O)$, Alfa Aesar, 99.5%), ytterbium(III) nitrate hydrate ($Yb(NO_3)_3 \cdot x(H_2O)$, Alfa Aesar, 99.99%), palladium(II) acetate ($Pd(CH_3CO_2)_2$, Sigma Aldrich, 99.9%), tri-tert-butlyphosphonium tetrafluoroborate ($C_{12}H_{28}PBF_4$, AmBeed, 98%), cesium carbonate (Cs_2CO_3, Sigma Aldrich, 99%), sodium chloride (NaCl, Fisher Chemical), potassium hydroxide (KOH, Fisher Chemical, ≥85%), tetrathiafulvalene ($C_6H_4S_4$, AmBeed, 98.00%), ethyl 4-bromobenzoate ($C_9H_9BrO_2$, AmBeed, 98%), silica (Silicycle, 40-63 μm), tetrabutylammonium hexafluorophosphate ($TBAPF_6$; $C_{16}H_{36}F_6NP$, Fisher Chemical, 98%), sodium sulfate (Na_2SO_4, Fisher Chemical, >99%).

PXRD data were collected using a Bruker D2 Phaser or a Bruker D8 Advance both equipped with a CuKα X-ray source (λ = 1.54 Å) and a nickel filter, or a Rigaku MiniFlex 600. Powder materials were prepared via dropcasting from methanol or neat onto a sample holder.

Nitrogen adsorption-desorption isotherm data were collected at 77 K using a Micromeritics Tristar II Plus surface area and porosity analyzer. Samples were vacuum activated for the time and temperature specified in the experimental procedure (Sections 3.2.3.3) using a Micromeritics Smart VacPrep with a hybrid turbo vacuum pump.

DRIFTS spectra were collected using a Thermo Scientific Nicolet 6700 FT-IR with an MCT detector with a resolution of 1 cm^{-1} from 4000-800 cm^{-1}. Samples were diluted in the IR inactive KBr.

H^1 NMR spectra were recorded using a 300 MHz Bruker spectrometer with shifts referenced to the residual solvent peaks. MOFs were digested using approximately 4 drops of deuterated sulfuric acid in 0.4 mL of DMSO-d_6.

ICP-MS data was collected using an Agilent 7500 series by the Concordia Center for Biological Applications of Mass Spectrometry (CBAMS).

3.2.2. Synthesis of TTFTBA

Tetrathiafulvalene-3,4,5,6-tetrakis(4-benzoic acid) (TTFTBA) was synthesized according to literature methods with modifications (Scheme 3.1).[134,205]

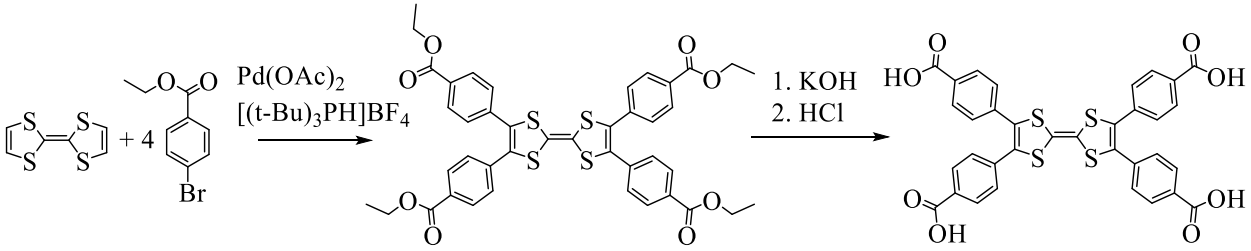

Scheme 3.1: The reaction scheme for the synthesis of the TTFTBA linker.

Palladium(II) acetate (0.40 mmol, 90 mg), tri-tert-butlyphosphonium tetrafluoroborate (0.12 mmol, 35 mg), and cesium carbonate (2.6 mmol, 850 mg) were added to degassed dioxane (120 mmol, 10 mL). The mixture was refluxed for 30 minutes under N_2 before tetrathiafulvalene (0.57 mmol, 116 mg) and ethyl 4-bromobenzoate (5.6 mmol, 920 μL) were added. This mixture was refluxed for 24-72 hours under N_2. The mixture was then concentrated using a rotary evaporator and extracted with dichloromethane or chloroform 3 times. The mixture was then washed with brine (~95 g of NaCl dissolved in 300 mL of water) and dried using sodium sulfate.

The mixture was then reconcentrated using a rotary evaporator and the sample was purified by column chromatography using silica gel with ethyl acetate as the mobile phase. The fraction containing tetrathiafulvalene-3,4,5,6-tetrakis(ethyl-4-benzoate) was determined by thin layer chromatography on an aluminum backed silica plate using 1:1 ethyl acetate:DCM as the mobile phase. The fractions were rotary evaporated to dryness. The dark red solid product, tetrathiafulvalene-3,4,5,6-tetrakis(ethyl-4-benzoate) was confirmed by ^{1}H NMR spectroscopy with the aromatic Hs at 7.57 and 7.90 ppm, and the alkane Hs from the ethyl group at 1.39 and 4.36 ppm (Figure S.3.1).

Tetrathiafulvalene-3,4,5,6-tetrakis(ethyl-4-benzoate) was dissolved in a 1:1:1 solution of THF:methanol:water (2.5 mol, 45 mL total) and degassed with N_2 for 30 minutes. To this, potassium hydroxide (20 mmol, 1.1 g) was added and the reaction was refluxed under N_2 for 12-72 hours. The mixture was then dried by rotary evaporation and an orange solid was obtained, potassium tetrathiafulvalene-3,4,5,6-tetrakis(4-benzoate). The solid was then dissolved in water and with stirring hydrochloric acid was added to reach a pH of 2. As the HCl was added, a lilac precipitate formed and was separated by vacuum filtration and was rinsed thoroughly with water. The purple tetrathiafulvalene-3,4,5,6-tetrakis(4-benzoic acid) (TTFTBA) was then confirmed by electrospray ionization mass spectrometry in positive mode (Figure S.3.2b) with the linker present at 684.0035 m/z and ^{1}H NMR spectroscopy with the aromatic Hs at 7.61 and 7.94 ppm (Figure S.3.3). The cumulative yield was 77%.

3.2.3. TTFTBA MOF Synthesis

A variety of MOF synthesis attempts were conducted using the redox active TTFTBA linker. These syntheses were performed using four different RE metal ions, including Ce(III), Ce(IV), Lu(III), and Yb(III). PXRD patterns collected from products obtained in all synthesis attempts were compared to simulated patterns of previously reported MOFs including the Zr(IV) based ACM-10 and 11;[206] RE(III) based MUV-5;[207] the RE(III) based Re(III)-TTFTBA MOF with **shp** topology,[138] and a RE based RE(III)-TTFTBA chain MOF.[208] Synthetic methods attempted were derived from literature methods for RE-CU-10,[23] RE(III) -TTFTBA MOF with **shp** topology,[138] and a RE(III)-TTFTBA chain MOF[208] with and without modifications. Each synthetic method hereafter is categorized by the literature article where the method was first described. The

initial attempt with each literature method, as well as a table indicating modifications made to the literature method is included.

3.2.3.1. Su et al. shp TTFTBA MOF Synthesis and Modifications

Su *et. al.* published the synthesis of a series of RE(III)-MOFs with the **shp** topology and cluster-based nodes using Y(III), Sm(III), Gd(III), Tb(III), Dy(III), Ho(III), and Er(III).[138] Their published synthetic method was used herein in synthetic attempts with Ce(III) an Ce(IV) ions.

Diammonium cerium(IV) nitrate or cerium(III) nitrate hexahydrate (0.03 mmol; 16 mg Ce(IV) precursor or 13 mg Ce(III) precursor) was dissolved and sonicated in DMF (13 mmol, 1.0 mL). Separately TTFTBA (0.02 mmol, 14 mg) was dissolved and sonicated in DMF (13 mmol, 1.0 mL). These samples were then combined in a 4, 6, or 8 dram to which TFA (1.4 mmol, 110 µL) was added before being placed in the oven at 120 °C for 72 hours. A variety of different ratios between metal and modulator and solvent were tested using this method (Table 3.1). The precipitate was separated by centrifugation and solvent exchange was performed with DMF (3 mL) 3x and acetone (3 mL) 3x before being air dried and characterized by PXRD.

The identifiers named in Table 3.1 are how the methods will be identified when discussed in sections 3.3 and 3.4.

Table 3.1: Reagents used for synthetic attempts of Ce(III) and Ce(IV)-based MOFs with the TTFTBA linker based on the Su *et al.* **shp** MOF method.[138]

Ions	**Identifier**	**Metal precursor (mg)**	**DMF**		**TFA**	
			moles/ mole metal	**volume (mL)**	**moles/ mole metal**	**volume (µL)**
Ce(III)	M3.1.1	13 (0.03 mmol)	1 000	2.3	20	46
Ce(III)	M3.1.2	13 (0.03 mmol)	1 000	2.3	10	23
Ce(IV)	M3.1.3	16 (0.03 mmol)	1 000	2.3	10	22
Ce(IV)	M3.1.4	16 (0.03 mmol)	2 000	4.5	10	22
Ce(IV)	M3.1.5	16 (0.03 mmol)	1 000	2.3	20	45

3.2.3.2. Su *et. al.* TTFTBA Chain-based MOF Synthesis and Modifications

Su *et. al.* published the synthesis of a series of MOFs comprised of RE(III)-chain nodes using Tb(III), Dy(III), Ho(III), and Er(III).[208] Their published synthetic method was used herein in synthetic attempts with Ce(III) an Ce(IV) ions.

Diammonium cerium(IV) nitrate or cerium(III) nitrate hexahydrate (0.03 mmol; 16 mg Ce(IV) precursor or 13 mg Ce(III) precursor) was dissolved and sonicated in DMF (14 mmol, 1.1 mL) and water (28 mmol, 0.50 mL). Separately TTFTBA (0.02 mmol, 14 mg) was dissolved and sonicated in DMF (14 mmol, 1.1 mL). These solutions were combined in a 4 or 6 dram vial then TFA (0.6 mmol, 46 μL) and chlorobenzene (8 mmol, 810 μL) were added. These vials were then placed in the oven for 72 hours at 60° C. After, the samples were analyzed by optical microscopy and the precipitate was separated by centrifugation and solvent exchange was performed with DMF (3 mL) 3x and acetone (3 mL) 3x before being air dried and characterized by PXRD.

The identifiers M3.2.1 and M3.2.2 for the Ce(III) and Ce(IV) method respectively will be used for the identification of these methods when discussed in sections 3.3 and 3.4.

3.2.3.3. Quezada-Novoa *et. al.* shp RE MOF

Quezada-Novoa *et. al.* published the synthesis of a series of RE(III)-MOFs with **shp** topology and cluster-based nodes using Tb(III) and Y(III) and the linker 1,3,6,8-tetrakis(4-benzoic acid)pyrene, a MOF named RE-CU-10.[23] The published synthetic method was used herein in synthetic attempts with Ce(III), Ce(IV), Yb(III), and Lu(III) ions. The pyrene-based linker used in the synthesis of CU-10 has a similar geometry to the TTFTBA linker. Modifications to this method include the addition of different or multiple modulators; different mole ratios between linker, modulator(s), and metal ion. Modifications to the mole ratio are indicated in Table 3.2. All reactions were performed at 120 °C for at least 72 hours.

Diammonium cerium(IV) nitrate, cerium(III) nitrate hexahydrate, lutetium(III) nitrate hydrate, or ytterbium(III) nitrate hydrate (0.1 mmol; 55 mg of Ce(IV) precursor, 43 mg of Ce(III) precursor, 47 mg of Lu(III) precursor, and 47 mg of Yb(III) precursor); TTFTBA (0.02 mmol, 14 mg); and FBA (14 mmol, 2.0 g) were dissolved and sonicated in DMF (90 mmol, 7.0 mL) in a 6 or 8 dram vial. To this mixture acetic acid (30 mmol, 1.7 mL) was added. This sample was then placed in the oven at 120° C for 72 hours. After, the sample was analyzed by optical microscopy

and the precipitate was separated from the reaction solvent by centrifugation. The precipitate was separated by centrifugation and solvent exchange was performed with DMF (3 mL) 3x, and acetone (3 mL) 3x before being air dried and characterized by PXRD and vacuum activated at 80 °C for 16 hours before the N_2 gas adsorption-desorption isotherm was collected. Activation procedures were determined based on those used for the reported RE(III)-TTFTBA **shp** MOFs.[138]

The identifiers named in Table 3.2 are how the methods will be identified when discussed in sections 3.3 and 3.4.

Table 3.2: The reagents and amounts used for synthetic attempts based on the Quezada-Novoa *et al* **shp** MOF method.[23]

Ions	**Identifier**	**Metal precursor (mg)**	**FBA**		**Acetic acid**		**TFA**	
			moles/ mole metal	**mass (mg)**	**moles/ mole metal**	**volume (µL)**	**moles/ mole metal**	**volume (µL)**
Ce(III)	M3.3.1	43 (0.1 mmol)	100	1 400	200	1 100	0	0
Ce(III)	M3.3.2	43 (0.1 mmol)	200	2 800	200	1 100	0	0
Ce(III)	M3.3.3	43 (0.1 mmol)	60	830	200	1 100	0	0
Ce(III)	M3.3.4	43 (0.1 mmol)	30	420	200	1 100	0	0
Ce(III)	M3.3.5	43 (0.1 mmol)	100	1 400	400	2 300	0	0
Ce(III)	M3.3.6	43 (0.1 mmol)	100	1 400	100	570	0	0
Ce(III)	M3.3.7	43 (0.1 mmol)	100	1 400	40	230	0	0
Ce(III)	M3.3.8	43 (0.1 mmol)	100	1 400	200	1 100	0	0
Ce(III)	M3.3.9	43 (0.1 mmol)	100	1 400	0	0	70	530
Ce(IV)	M3.3.10	55 (0.1 mmol)	100	1 400	0	0	80	610
Ce(IV)	M3.3.11	55 (0.1 mmol)	100	1 400	200	1 100	0	0

Table 3.3: Reagents used for the synthesis of Lu(III) and Yb(III) MOFs with the TTFTBA linker and **shp** topology.

Ions	**Precursor (mg)**	**TTFTBA (mg)**	**DMF (mL)**	**FBA (mg)**	**Acetic Acid (µL)**	**Nitric Acid (µL)**	**TFA (µL)**	**Water (µL)**
Lu(III)	56 (0.1 mmol)	21 (0.03 mmol)	11	2 300	0	190	120	0
Yb(III)	58 (0.1 mmol)	21 (0.03 mmol)	5.7	1 400	1.2	230	0	470

The Quezada-Novoa *et. al.* method was modified to successfully synthesize MOFs using Lu(III) and Yb(III) that are isostructural to the **shp** MOF synthesized by Su *et. al.* The synthetic parameters are indicated in Table 3.3.

3.3. Results and Discussion

The PXRD patterns for the method variations (Table 3.1) to the published method by Su *et al.* are shown in Figure 3.3.[138] From these diffractograms, none of the experimental patterns align with the simulated pattern of the target MOF. The modifications to the reported method that were explored were using both Ce(III) (M3.1.1 and M3.1.2) and Ce(IV) (M3.1.3, M3.1.4, and M3.1.5) precursor. In addition, the mole ratio between the metal and the TFA and DMF were also varied, none of which yielded synthesis of the **shp** TTFTBA MOF with Ce(III) or Ce(IV).

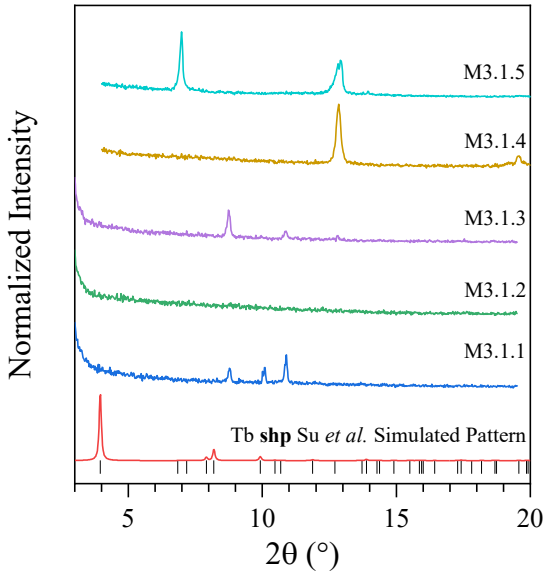

Figure 3.3: PXRD pattern of the materials synthesized using methods reported in Table 3.1.

The next synthesis attempts were based on the method reported by Su *et al.* for the synthesis of MOFs containing RE(III)-chain nodes.[208] These MOFs were reported with Tb(III), Dy(III), Ho(III), and Er(III). This method was tested using Ce(III) (M3.2.1) and Ce(IV) (M3.2.2) and PXRD patterns were collected. The collected PXRD patterns shown in Figure 3.4 when compared with the simulated pattern indicate that the synthesis was not successful with either Ce(III) (M3.2.1) or Ce(IV) (M3.2.2). Interestingly the two methods using different metal precursors yielded the same diffraction pattern, indicating that the precipitate synthesized either does not contain the metal ions at all or that the material can be composed of ither Ce(III) or Ce(IV).

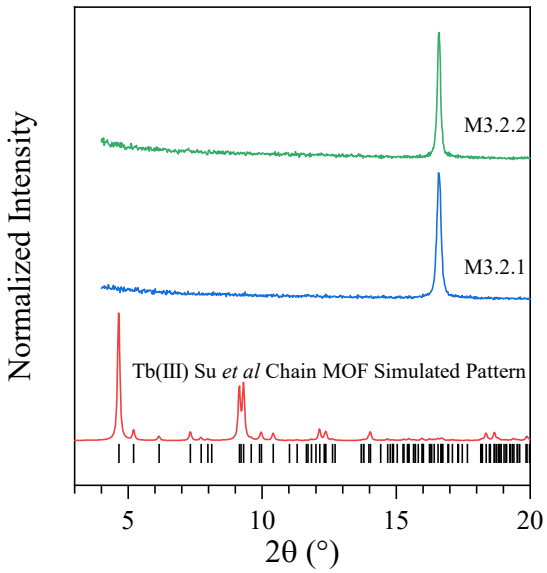

Figure 3.4: PXRD pattern of the materials synthesized using methods reported in section 3.2.3.2 using Ce(III) (a) and Ce(IV) (b).

The third synthetic method explored and modified using Ce(III) and Ce(IV) was published by Quezada-Novoa *et. al.* This modified synthetic method uses the modulator 2-FBA, TFA, and acetic acid in various molar ratios compared to the metal precursor (Table 3.2). The first 9 attempts using Ce(III) (M3.3.1-M3.3.9) gave precipitate that was analyzed by PXRD and the diffraction patterns are shown in Figure 3.5. Upon comparing the collected diffractograms (Figure 3.5) to the simulated pattern for the RE(III)-TTFTBA **shp** MOF all 9 attempts (Table 3.2) indicate that the **shp** MOF was not synthesized. M3.3.1-M3.3.4 used the same amount of acetic acid with no TFA while modifying the amount of 2-FBA used. Interestingly, the method with the highest mole ratio of 2-FBA (M3.3.2) to Ce(III) yielded a different material with a larger unit cell than those methods with less 2-FBA. The next methods used, M3.3.5-M3.3.8, explored the effect of changing the mole ratio of Ce(III) to acetic acid with no TFA and a constant amount of 2-FBA. The two methods M3.3.6 and M3.3.8 used 100 and 200 moles of acetic acid per mole of Ce(III) respectively. Both methods lead to materials with the largest unit cells when compared to M3.3.7 and M3.3.5 the lowest and highest amounts of acetic acid respectively. The reaction containing the lowest amount of acetic acid (M3.3.7) yielded a non-crystalline precipitate (from 3-20° 2θ). While the highest amount of acetic acid (M.3.3.5) amount yielded the same crystalline product observed from many

of the methods with a constant amount of acetic acid and various amounts of 2-FBA (M3.3.1, M3.3.3, and M3.3.4). For synthesis attempts using M3.3.9, acetic acid was removed from the synthesis and TFA was used. This method (M3.3.9) yielded a sample with a smaller unit cell, indicated by the lowest angle reflection occurring at 18° 2θ.

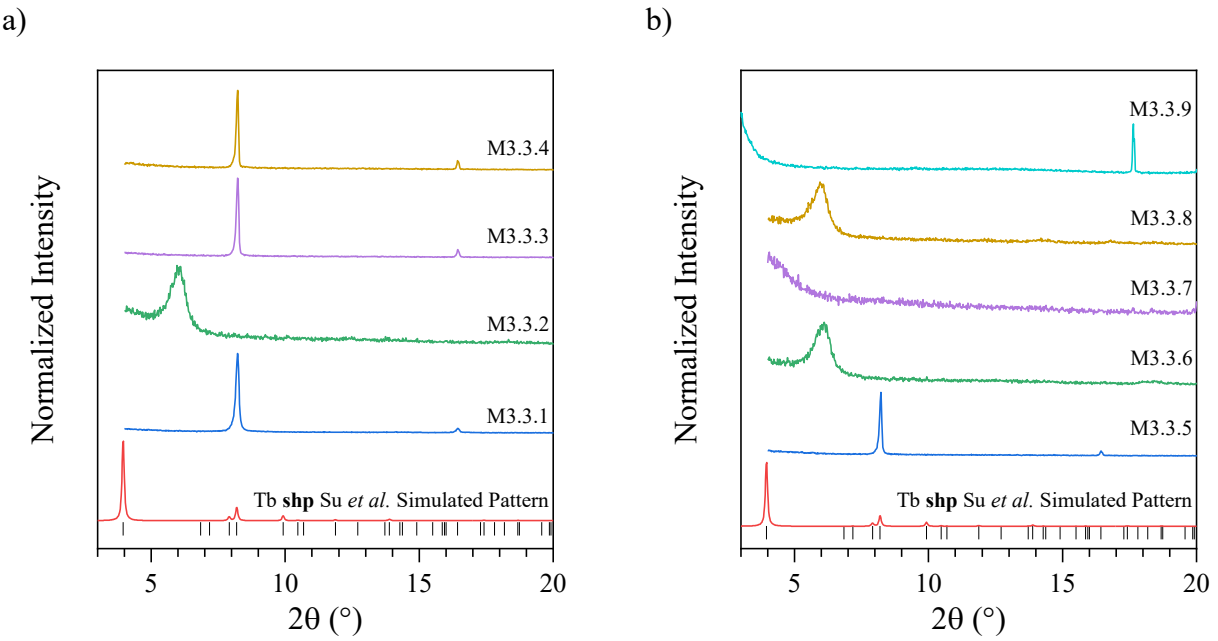

Figure 3.5: PXRD pattern of the materials synthesized using methods reported in Table 3.2 using Ce(III).

Synthesis attempts using Ce(IV) with the Quezada-Novoa e*t al.* method were also analyzed by PXRD (Figure 3.6). Two different modifications (Table 3.2) to the reported method were used with the Ce(IV) precursor, the first, M3.3.10, used the modulators TFA and 2-FBA with 2-FBA being used in the same mole ratio to precursor as M3.3.5-M3.3.9.The precipitate from the method (M3.3.10) indicates that a **shp** TTFTBA MOF was not synthesized. The same was determined for the second modified method, M3.3.11. This method when compared to the simulated pattern is inconclusive as the diffractogram was not collected to low enough 2θ to compare the largest peak in the simulated MOF with the material, and the other peaks present do tend to align with the simulated pattern. However, it was concluded that the synthesis of an **shp** MOF with TTFTBA and Ce was unsuccessful.

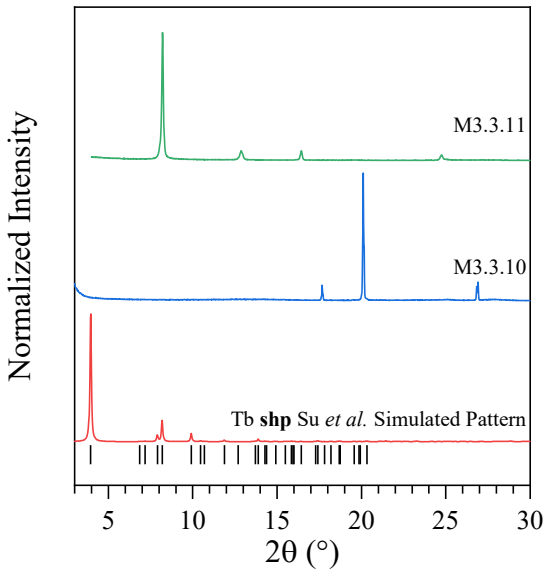

Figure 3.6: PXRD pattern of the materials synthesized using methods reported in Table 3.2 using Ce(IV) .

Due to the lack of success synthesizing Ce(III) and Ce(IV)-based MOFs with the TTFTBA linker, the next goal was to synthesize novel RE(III)-MOFs with the TTFTBA linker to study the redox active properties of the MOFs with redox active linkers only. The Quezada-Novoa *et al.* method was used for the synthesis of an **shp** TTFTBA MOF with Lu(III) and Yb(III). These synthetic methods shown in Table 3.3 used the modulators, 2-FBA, nitric acid, and TFA for the Lu(III) MOF, and 2-FBA, acetic acid, and nitric acid for the Yb(III) MOF. When comparing the product obtained from these synthetic methods by PXRD to the simulated pattern in Figure 3.7, the synthesis was determined to be a success, as the experimental diffractograms match the simulated pattern. The simulated Tb(III)-TTFTBA **shp** MOF pattern matches more closely to the material obtained with Yb(III), then to the Lu(III), possibly because of the slightly closer ionic radius of Yb(III) (1.010 Å) to Tb(III) (1.090 Å) relative to Lu(III) (0.995 Å).[209]

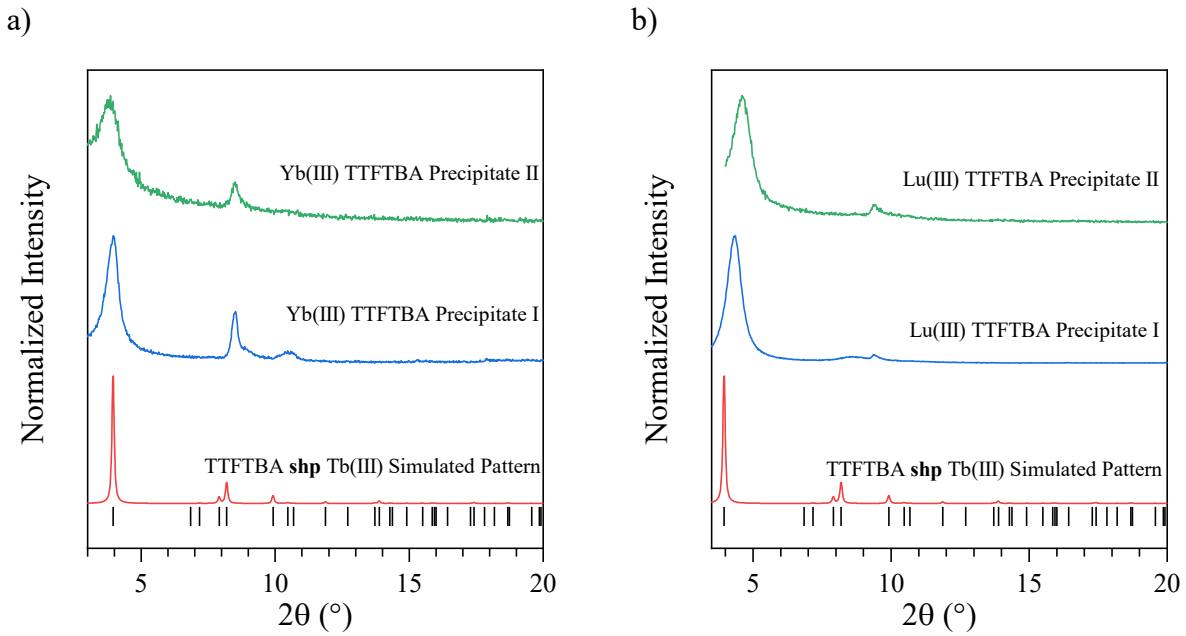

Figure 3.7: PXRD pattern of the materials synthesized using methods reported in Table 3.3 using Yb(III) (a) and Lu(III) (b).

Due to extremely low yields of the Yb(III) material, it was not fully characterized indicating that further synthetic method development is required. The Lu(III) material was characterized by N_2 gas adsorption-desorption analysis giving a BET area of 18 m^2/g (Figure 3.8). This material gives a Type II isotherm, indicating that it is either macroporous or nonporous.[173] The low BET area of 18 m^2/g calculated from this isotherm indicates that the activation procedure (section 3.2.3.3) was either not successful at removing the remaining solvent, side products, and modulators from the MOF pores, or that the activation procedure caused the MOF to collapse. The PXRD collected after N_2 gas adsorption-desorption analysis (Figure 3.9) suggests that the MOF did not collapse upon activation.

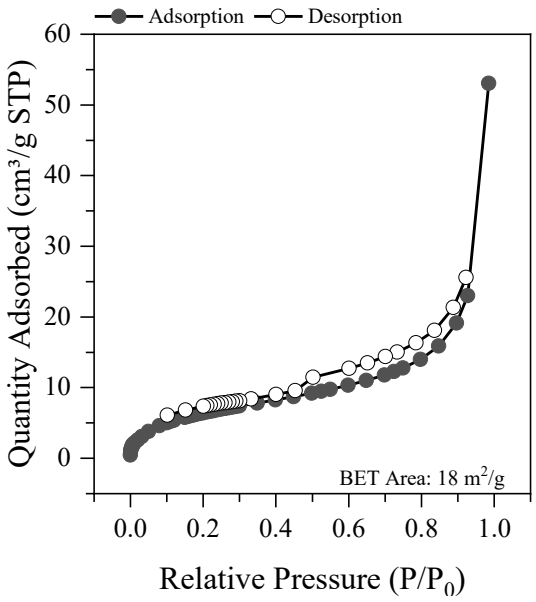

Figure 3.8: N_2 gas adsorption and desorption isotherm and BET area of Lu(III) TTFTBA precipitate.

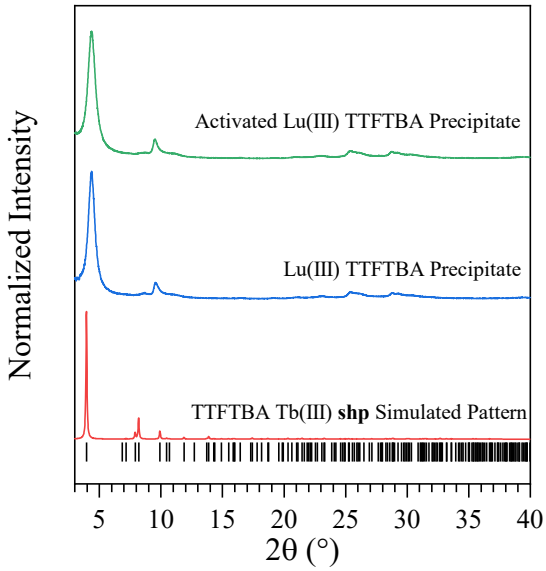

Figure 3.9: The PXRD pattern collected of the Lu(III) and TTFTBA precipitate before and after activation.

.

The material was also characterized by ICP-MS (Table 3.4) to determine the amount of Lu in the material compared to organic components. The chemical formula for a nonanuclear RE(III) **shp** MOF was assumed based on the formula determined by SCXRD as reported by Su *et al.*: $Lu_9(\mu_3\text{-}OH)_{13}(\mu_3\text{-}O)(H_2O)_9(TTFTB)_3$, where TTFTB is the conjugate base of TTFTBA (tetrathiafulvalene-3,4,5,6-tetrakis(4-benzoate).[138] This yielded a molar mass for the Lu(III)-TTFTBA **shp** MOF of 3 908 g/mol. The ICP-MS results indicate that there are 9.4 moles of Lu per mole of MOF. This is further affirmation that the Lu(III)-TTFTBA **shp** MOF has been synthesized.

Table 3.4: ICP-MS results and calculations of the amount of moles of Lu per mole of precipitate.

Mass of Precipitate Analyzed (mg)	**Moles of MOF**	**Volume of Dilution (mL)**	**Experimental Concentration of Lu in Precipitate (ppm)**	**Moles of Lu**	**Moles of Lu per mole of MOF**
3.2	8.2×10^{-7}	10	135.2	7.7×10^{-6}	9.4

Upon analysis of the Lu(III)-TTFTBA **shp** MOF by DRIFTS, shown in Figure 3.10, the presence of water is observed with characteristic wide stretch at ~3 700 cm^{-1}, shown in light blue. Further notable stretches include carbonyl C=O stretches of the linker at ~1 600 cm^{-1}, shown in green. DRIFTS analysis thus affirms the previous characterizations that the MOF has been successfully synthesized.

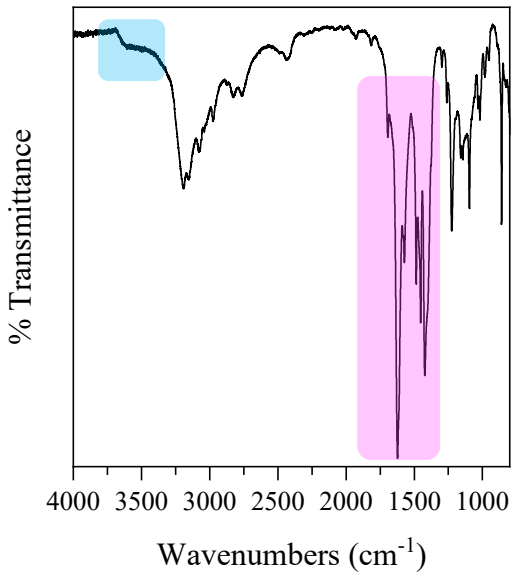

Figure 3.10: DRIFTS of the Lu(III) TTFTBA precipitate. The light blue shading indicates the O-H bond stretch and pink indicates the C=O bonding.

The ^{1}H NMR spectrum, shown in Figure 3.11, of the digested MOF was collected and indicates three different types of aromatic H present. Shown in Figure 3.11, the spectrum indicates two aromatic Hs at 7.75 and 7.53 ppm in slightly different electronic environments (yellow and green), and two aromatic Hs in identical electronic environments (red). This is as expected for this material and confirms the synthesis of the Lu(III)-TTFTBA **shp** MOF.

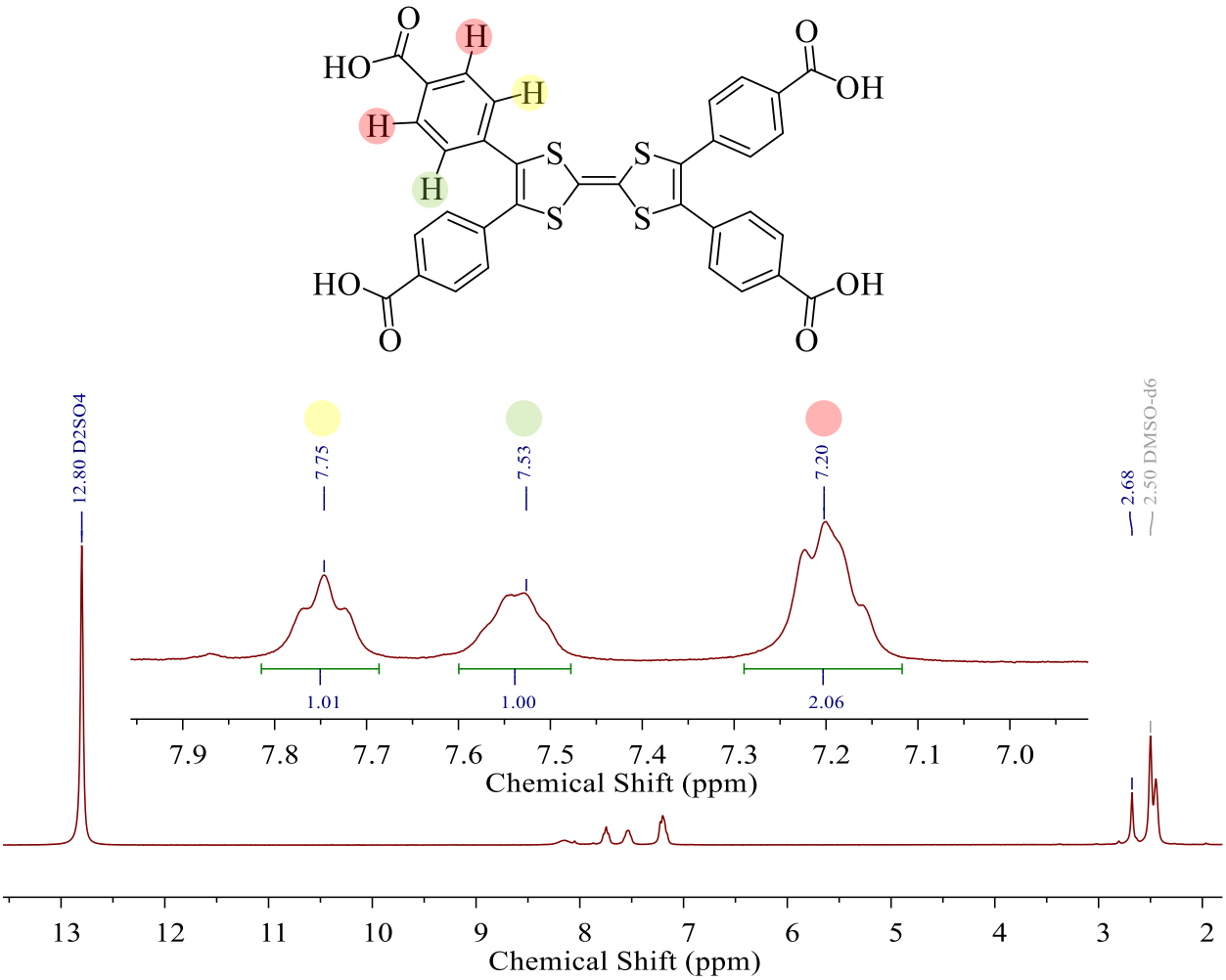

Figure 3.11: ^{1}H NMR spectrum of Lu(III) TTFTBA precipitate. Aromatic Hs are present at 7.75, 7.53, and 7.20 ppm.

3.4. Conclusion

The synthesis of a MOF with the redox active linker TTFTBA and the redox active Ce(III/IV) was explored from three different starting methods. First, a **shp** MOF method, reported by Su *et al.* was modified using either Ce(III) or Ce(IV) precursor and by adjusting the molar ratio of the TFA modulator and DMF. All these attempts were determined to be unsuccessful by PXRD.[138] The next method explored was by Su *et al.* for the synthesis of a chain based RE(III)-MOF. These methods were explored using both Ce(III) and Ce(IV) and were determined to be unsuccessful upon analysis of the precipitates PXRD. The third method explored was based on the

published method by Quezada-Novoa *et al.*[23] This method was tested with extensive modifications including using Ce(III) or Ce(IV) and by modifying the molar ratio of various modulators to metal. The modulators used include 2-FBA, acetic acid, and TFA. Some of these methods indicates that some structures with unit cells similar in scale to a 3D MOF may have been synthesized, but none of the precipitates were the **shp** TTFTBA MOF. Thus, to make a MOF with redox active nodes and linkers further extensive optimization is required.

The synthesis of 3D cluster-based RE(III)-MOFs using TTFTBA was successful when using a modified version of the method published by Quezada-Novoa *et al*. The synthesis of an **shp** MOF with the TTFTBA linker and Yb(III) or Lu(III) nonanuclear clusters was confirmed by PXRD. The Lu(III)-TTFTBA **shp** MOF was characterized by N_2 gas adsorption-desorption isotherms with BET calculations, DRIFTS, ICP-MS, and ^{1}H NMR spectroscopy.

Chapter 4
Conclusions and Future Work

4.1. General Conclusions

The synthesis of a variety of redox active RE cluster-based MOFs was completed. The fundamental electrochemical characteristics of these MOFs was determined and studied.

The analysis of a series of Ce(IV)-UiO-66/67 MOFs composed of various functionalized and nonfunctionalized linkers including BDC, BrBDC, FBDC, F_4BDC, NH_2BDC, DOBDC, and BPyDC. For the first time, the electrochemical effects of the various functionalities of the linkers on the redox active Ce(IV) clusters was explored by CV. The MOFs were synthesized and characterized by PXRD, N_2 gas adsorption-desorption isotherms with BET calculations, DRIFTS, and ^{1}H NMR spectroscopy; before being dropcast onto films allowing voltammograms to be collected. Optimization of parameters for electrochemical analysis was completed and the reduction potentials were analyzed and compared. Fundamentally, the relationship between the functional groups and the reduction potential indicates a decreased reduction potential from Ce(IV) when there are electron donating groups present in the linkers, while the presence of electron withdrawing groups increases the reduction potential.

Further synthesis of redox active MOFs was explored using the redox active linker: TTFTBA. The TTFTBA linker was first synthesized and characterized by ^{1}H NMR spectroscopy and ESI-MS. Synthetic methods from literature were then used extensively to attempt the synthesis of a MOF containing redox active Ce(III/IV) clusters as well as the redox active TTFTBA linker. Additionally, the synthesis of MOFs utilizing the TTFTBA linker and other RE(III) metals, including Yb(III) and Lu(III) was performed and confirmed by PXRD. Of these two new MOFs, the Lu(III)-TTFTBA **shp** MOF was fully characterized by PXRD, N_2 gas adsorption-desorption isotherms with BET calculations, DRIFTS, ICP-MS, and ^{1}H NMR spectroscopy.

4.2. Future Work

In order to completely understand the electrochemical effects that various functionalities have on the Ce(IV) clusters of Ce(IV)-UiO-66 it would be of interest to expand the series that is

being studied. Most obviously these include functionalizing the BDC with a nitro, azide, sulfhydryl, or chloro group; or adding alkane structures such as methyl or ethyl groups. The further expansion of these linkers and the effect on the reduction potentials of the materials would allow for further tailoring of MOFs for specific catalytic or electrochemical applications. Further electrochemical analysis of these materials aimed toward specific applications could include the incorporation of the MOF into battery test cells.

With regards to the synthesis of MOFs containing redox active Ce(III/IV) clusters and the redox active TTFTBA linker, further synthetic attempts are warranted. Ideally synthetic attempts that yield the growth of crystals larger then 100 μm which would allow for characterization by SCXRD. Theoretically, by increasing the density of redox events that can occur in the same area of MOF, the conductivity of the MOF may increase via the redox hopping pathway.

Furthermore, the full characterization of the newly synthesized Yb(III) **shp** TTFTBA MOF should be completed and single crystals of both the Yb(III) and Lu(III) MOFs should be grown and characterized definitively by SCXRD. Additionally, expanding the **shp** TTFTBA MOF series to include the not yet synthesized clusters composed of Sc(III), La(III), Eu(III), Tm(III), Nd(III), or Pr(III) should be completed. The electrochemical properties of these materials should be determined by CV, and then the potentials applications of the materials studied.

References

(1) Watts, I. *J. Hum. Evol.* **2010**, *59* (3–4), 392–411.

(2) Wadley, L.; Hodgskiss, T.; Grant, M. *Proc. Natl. Acad. Sci.* **2009**, *106* (24), 9590–9594.

(3) Rasmussen, S. C. In *ACS Symposium Series*; Rasmussen, S. C., Ed.; American Chemical Society: Washington, DC, 2015; Vol. 1211, pp 1–15.

(4) Doeff, M. M.; Clément, R. J.; Canepa, P. *Chem. Mater.* **2022**, *34* (2), 463–467.

(5) Howarth, A. J.; Peters, A. W.; Vermeulen, N. A.; Wang, T. C.; Hupp, J. T.; Farha, O. K. *Chem. Mater.* **2017**, *29* (1), 26–39.

(6) Meek, S. T.; Greathouse, J. A.; Allendorf, M. D. *Adv. Mater.* **2011**, *23* (2), 249–267.

(7) Kinoshita, Y.; Matsubara I.; Higushi T.; Saito Y.; *Bull. Chem. Soc. Jpn.* **1959,** 32 (11), 1221-1226.

(8) Tomic, E. A. *J. Appl. Polym. Sci.* **1965**, *9* (11), 3745–3752.

(9) Yaghi, O. M.; Li, H. *J. Am. Chem. Soc.* **1995**, *117* (41), 10401–10402.

(10) Batten, S. R.; Champness, N. R.; Chen, X.-M.; Garcia-Martinez, J.; Kitagawa, S.; Öhrström, L.; O'Keeffe, M.; Paik Suh, M.; Reedijk, J. *Pure Appl. Chem.* **2013**, *85* (8), 1715–1724.

(11) CSD MOF Collection. https://www.ccdc.cam.ac.uk/Community/csd-community/csd-mof-collection/.

(12) Moghadam, P. Z.; Li, A.; Wiggin, S. B.; Tao, A.; Maloney, A. G. P.; Wood, P. A.; Ward, S. C.; Fairen-Jimenez, D. *Chem. Mater.* **2017**, *29* (7), 2618–2625.

(13) Korolev, V. V.; Nevolin, Y. M.; Manz, T. A.; Protsenko, P. V. *J. Chem. Inf. Model.* **2021**, *61* (12), 5774–5784.

(14) Han, X.; Wu, T.; Gu, L.; Tian, D. *New J. Chem.* **2022**, *46* (8), 3747–3753.

(15) Dermanaki Farahani, S.; Zolgharnein, J. *Inorg. Chem. Commun.* **2022**, *140*, 109388.

(16) Alezi, D.; Belmabkhout, Y.; Suyetin, M.; Bhatt, P. M.; Weseliński, Ł. J.; Solovyeva, V.; Adil, K.; Spanopoulos, I.; Trikalitis, P. N.; Emwas, A.-H.; Eddaoudi, M. *J. Am. Chem. Soc.* **2015**, *137* (41), 13308–13318.

(17) Orellana-Tavra, C.; Köppen, M.; Li, A.; Stock, N.; Fairen-Jimenez, D. *ACS Appl. Mater. Interfaces.* **2020**, *12* (5), 5633–5641.

(18) Vaesen, S.; Guillerm, V.; Yang, Q.; Wiersum, A. D.; Marszalek, B.; Gil, B.; Vimont, A.; Daturi, M.; Devic, T.; Llewellyn, P. L.; Serre, C.; Maurin, G.; De Weireld, G. *Chem. Commun.* **2013**, *49* (86), 10082.

(19) Cavka, J. H.; Jakobsen, S.; Olsbye, U.; Guillou, N.; Lamberti, C.; Bordiga, S.; Lillerud, K. P. *J. Am. Chem. Soc.* **2008**, *130* (42), 13850–13851.

(20) Wang, B.; Ma, Y.; Xu, W.; Tang, K. *Langmuir.* **2022**, *38* (29), 8954–8963.

(21) Katz, M. J.; Howarth, A. J.; Moghadam, P. Z.; DeCoste, J. B.; Snurr, R. Q.; Hupp, J. T.; Farha, O. K. *Dalton Trans.* **2016**, *45* (10), 4150–4153.

(22) Donnarumma, P. R.; Frojmovic, S.; Marino, P.; Bicalho, H. A.; Titi, H. M.; Howarth, A. J. *Chem. Commun.* **2021**, *57* (50), 6121–6124.

(23) Quezada-Novoa, V.; Titi, H. M.; Sarjeant, A. A.; Howarth, A. J. *Chem. Mater.* **2021**, *33* (11), 4163–4169.

(24) Ayhan, O.; Malaestean, I. L.; Ellern, A.; van Leusen, J.; Baca, S. G.; Kögerler, P. *Cryst. Growth Des.* **2014**, *14* (7), 3541–3548.

(25) Hong, X.-J.; Song, C.-L.; Yang, Y.; Tan, H.-C.; Li, G.-H.; Cai, Y.-P.; Wang, H. *ACS Nano.* **2019**, 13 (2), 1923-1931

(26) Guo, Z.; Xu, H.; Su, S.; Cai, J.; Dang, S.; Xiang, S.; Qian, G.; Zhang, H.; O'Keeffe, M.; Chen, B. *Chem. Commun.* **2011**, *47* (19), 5551–5553.

(27) Zhu, W.-H.; Zeng, M.; Wang, J.; Li, C.-Y.; Tian, L.-H.; Yin, J.-C.; Liu, Y.-K. *Dalton Trans.* **2016**, *45* (25), 10141–10145.

(28) Lu, W.; Wei, Z.; Gu, Z.-Y.; Liu, T.-F.; Park, J.; Park, J.; Tian, J.; Zhang, M.; Zhang, Q.; Gentle III, T.; Bosch, M.; Zhou, H.-C. *Chem Soc Rev.* **2014**, *43* (16), 5561–5593.

(29) Yaghi., O. M.; O'Keefe, M.; Ockwig, N. W.; Chae, H. K.; Eddaoudi, M.; Kim; J. *Nature*. **2003**, 423, 705-714

(30) O'Keeffe, M. *Chem. Soc. Rev.* **2009**, *38* (5), 1215.

(31) Kalmutzki, M. J.; Hanikel, N.; Yaghi, O. M. *Sci. Adv.* **2018**, *4* (10), eaat9180.

(32) O'Keeffe, M.; Peskov, M. A.; Ramsden, S. J.; Yaghi, O. M. *Acc. Chem. Res.* **2008**, *41* (12), 1782–1789.

(33) Kim, D.; Liu, X.; Lah, M. S. *Inorg. Chem. Front.* **2015**, *2* (4), 336–360.

(34) Öhrström, L. *Crystals.* **2015**, *5* (1), 154–162.

(35) Hönicke, I. M.; Senkovska, I.; Bon, V.; Baburin, I. A.; Bönisch, N.; Raschke, S.; Evans, J. D.; Kaskel, S. *Angew. Chem. Int. Ed.* **2018**, *57* (42), 13780–13783.

(36) Li, P.; Vermeulen, N. A.; Malliakas, C. D.; Gómez-Gualdrón, D. A.; Howarth, A. J.; Mehdi, B. L.; Dohnalkova, A.; Browning, N. D.; O'Keeffe, M.; Farha, O. K. *Science.* **2017**, *356* (6338), 624–627.

(37) Snurr, R. Q. *Matter.* **2019**, *1* (1), 26–27.

(38) Moghadam, P. Z.; Rogge, S. M. J.; Li, A.; Chow, C.-M.; Wieme, J.; Moharrami, N.; Aragones-Anglada, M.; Conduit, G.; Gomez-Gualdron, D. A.; Van Speybroeck, V.; Fairen-Jimenez, D. *Matter.* **2019**, *1* (1), 219–234.

(39) Kang, I. J.; Khan, N. A.; Haque, E.; Jhung, S. H. *Chem. – Eur. J.* **2011**, *17* (23), 6437–6442.

(40) Winarta, J.; Shan, B.; Mcintyre, S. M.; Ye, L.; Wang, C.; Liu, J.; Mu, B. *Cryst. Growth Des.* **2020**, *20* (2), 1347–1362.

(41) Morozan, A.; Jaouen, F. *Energy Environ. Sci.* **2012**, *5* (11), 9269.

(42) Baumann, A. E.; Burns, D. A.; Liu, B.; Thoi, V. S. *Commun. Chem.* **2019**, *2* (1), 86.

(43) Xie, L. S.; Skorupskii, G.; Dincă, M. *Chem. Rev.* **2020**, *120* (16), 8536–8580.

(44) Dincă, M.; Léonard, F. *MRS Bull.* **2016**, *41* (11), 854–857.

(45) Housecroft, C. E.; Sharpe, A. G. 4th ed.; Pearson: Harlow, England ; New York, 2012.

(46) Miessler, G. L.; Fischer, P. J.; Tarr, D. A. Fifth edition.; Pearson: Boston, 2014.

(47) Zahadiya, H.; Wijesundera, R. P.; Hettiarachchi, C. V.; Perera, I. R. *ChemistrySelect.* **2021**, *6* (3), 425–429.

(48) Dhara, B.; Nagarkar, S. S.; Kumar, J.; Kumar, V.; Jha, P. K.; Ghosh, S. K.; Nair, S.; Ballav, N. *J. Phys. Chem. Lett.* **2016**, *7* (15), 2945–2950.

(49) Sun, L.; Miyakai, T.; Seki, S.; Dincă, M. *J. Am. Chem. Soc.* **2013**, *135* (22), 8185–8188.

(50) Sun, L.; Hendon, C. H.; Minier, M. A.; Walsh, A.; Dincă, M. *J. Am. Chem. Soc.* **2015**, *137* (19), 6164–6167.

(51) Sun, L.; Hendon, C. H.; Park, S. S.; Tulchinsky, Y.; Wan, R.; Wang, F.; Walsh, A.; Dincă, M. *Chem. Sci.* **2017**, *8* (6), 4450–4457.

(52) Heintz, R. A.; Zhao, H.; Ouyang, X.; Grandinetti, G.; Cowen, J.; Dunbar, K. R. *Inorg. Chem.* **1999**, *38* (1), 144–156.

(53) Park, S. S.; Hontz, E. R.; Sun, L.; Hendon, C. H.; Walsh, A.; Van Voorhis, T.; Dincă, M. *J. Am. Chem. Soc.* **2015**, *137* (5), 1774–1777.

(54) Sheberla, D.; Sun, L.; Blood-Forsythe, M. A.; Er, S.; Wade, C. R.; Brozek, C. K.; Aspuru-Guzik, A.; Dincă, M. *J. Am. Chem. Soc.* **2014**, *136* (25), 8859–8862.

(55) Darago, L. E.; Aubrey, M. L.; Yu, C. J.; Gonzalez, M. I.; Long, J. R. *J. Am. Chem. Soc.* **2015**, *137* (50), 15703–15711.

(56) Ziebel, M. E.; Darago, L. E.; Long, J. R. *J. Am. Chem. Soc.* **2018**, *140* (8), 3040–3051.

(57) Campbell, M. G.; Liu, S. F.; Swager, T. M.; Dincă, M. *J. Am. Chem. Soc.* **2015**, *137* (43), 13780–13783.

(58) Skorupskii, G.; Trump, B. A.; Kasel, T. W.; Brown, C. M.; Hendon, C. H.; Dincă, M. *Nat. Chem.* **2020**, *12* (2), 131–136.

(59) Aubrey, M. L.; Kapelewski, M. T.; Melville, J. F.; Oktawiec, J.; Presti, D.; Gagliardi, L.; Long, J. R. *J. Am. Chem. Soc.* **2019**, *141* (12), 5005–5013.

(60) Goswami, S.; Hod, I.; Duan, J. D.; Kung, C.-W.; Rimoldi, M.; Malliakas, C. D.; Palmer, R. H.; Farha, O. K.; Hupp, J. T. *J. Am. Chem. Soc.* **2019**, *141* (44), 17696–17702.

(61) Maity, D. K.; Dey, A.; Ghosh, S.; Halder, A.; Ray, P. P.; Ghoshal, D. *Inorg. Chem.* **2018**, *57* (1), 251–263.

(62) Wudl, F.; Smith, G. M.; Hufnagel, E. J. *J. Chem. Soc. Chem. Commun.* **1970**, No. 21, 1453.

(63) Piro, N. A.; Robinson, J. R.; Walsh, P. J.; Schelter, E. J. *Coord. Chem. Rev.* **2014**, *260*, 21–36.

(64) Yin, Z.; Wang, Q.-X.; Zeng, M.-H. *J. Am. Chem. Soc.* **2012**, *134* (10), 4857–4863.

(65) Zhang, X.; da Silva, I.; Fazzi, R.; Sheveleva, A. M.; Han, X.; Spencer, B. F.; Sapchenko, S. A.; Tuna, F.; McInnes, E. J. L.; Li, M.; Yang, S.; Schröder, M. *Inorg. Chem.* **2019**, *58* (20), 14145–14150.

(66) Wang, H.-Y.; Su, J.; Ma, J.-P.; Yu, F.; Leong, C. F.; D'Alessandro, D. M.; Kurmoo, M.; Zuo, J.-L. *Inorg. Chem.* **2019**, *58* (13), 8657–8664.

(67) Chen, X.; Wang, Z.; Hassan, Z. M.; Lin, P.; Zhang, K.; Baumgart, H.; Redel, E. *ECS J. Solid State Sci. Technol.* **2017**, *6* (4), P150–P153.

(68) Kung, C.-W.; Platero-Prats, A. E.; Drout, R. J.; Kang, J.; Wang, T. C.; Audu, C. O.; Hersam, M. C.; Chapman, K. W.; Farha, O. K.; Hupp, J. T. *ACS Appl. Mater. Interfaces.* **2018**, *10* (36), 30532–30540.

(69) Jin, Z.; Yan, J.; Huang, X.; Xu, W.; Yang, S.; Zhu, D.; Wang, J. *Nano Energy.* **2017**, *40*, 376–381.

(70) Jiang, H.; Liu, X.-C.; Wu, Y.; Shu, Y.; Gong, X.; Ke, F.-S.; Deng, H. *Angew. Chem. Int. Ed.* **2018**, *57* (15), 3916–3921.

(71) Bernales, V.; Ortuño, M. A.; Truhlar, D. G.; Cramer, C. J.; Gagliardi, L. *ACS Cent. Sci.* **2018**, *4* (1), 5–19.

(72) Rimoldi, M.; Howarth, A. J.; DeStefano, M. R.; Lin, L.; Goswami, S.; Li, P.; Hupp, J. T.; Farha, O. K. *ACS Catal.* **2017**, *7* (2), 997–1014.

(73) Liu, X.; Liu, B.; Li, G.; Liu, Y. *J. Mater. Chem. A.* **2018**, *6* (35), 17177–17185.

(74) Shustova, N. B.; McCarthy, B. D.; Dincă, M. *J. Am. Chem. Soc.* **2011**, *133* (50), 20126–20129.

(75) Mallakpour, S.; Nikkhoo, E.; Hussain, C. M. *Coord. Chem. Rev.* **2022**, *451*, 214262.

(76) Liu, X.; Wang, S.; Wang, A.; Wang, Z.; Chen, J.; Zeng, Q.; Chen, P.; Liu, W.; Li, Z.; Zhang, L. *J. Mater. Chem. A.* **2019**, *7* (42), 24515–24523.

(77) Su, Y.; Wang, W.; Wang, W.; Wang, A.; Huang, Y.; Guan, Y. *J. Electrochem. Soc.* **2022**, *169* (3), 030528.

(78) Shang, W.; Chen, Y.; Han, J.; Ouyang, P.; Fang, C.; Du, J. *ACS Appl. Energy Mater.* **2020**, *3* (12), 12351–12359.

(79) Deng, L.; Cai, C.; Huang, Y.; Fu, Y. *Microporous Mesoporous Mater.* **2022**, *329*, 111544.

(80) Song, X.; Zhang, Y.; Sun, P.; Gao, J.; Shi, F. *Chem. – Eur. J.* **2020**, *26* (25), 5654–5661.

(81) Zhao, R.; Liang, Z.; Zou, R.; Xu, Q. *Joule.* **2018**, *2* (11), 2235–2259.

(82) Xu, Y.; Li, Q.; Xue, H.; Pang, H. *Coord. Chem. Rev.* **2018**, *376*, 292–318.

(83) Li, B.; Liu, J.; Nie, Z.; Wang, W.; Reed, D.; Liu, J.; McGrail, P.; Sprenkle, V. *Nano Lett.* **2016**, *16* (7), 4335–4340.

(84) Wang, Z.; Wang, B.; Yang, Y.; Cui, Y.; Wang, Z.; Chen, B.; Qian, G. *ACS Appl. Mater. Interfaces.* **2015**, *7* (37), 20999–21004.

(85) Chen, Y.; Zhang, L.; Pan, H.; Zhang, J.; Xiang, S.; Cheng, Z.; Zhang, Z. *J. Mater. Chem. A* **2021**, *9* (47), 26929–26938.

(86) Liu, B.; Thoi, V. S. *Chem. Commun.* **2022**, *58* (25), 4005–4015.

(87) Weng, Y.-G.; Ren, Z.-H.; Zhang, Z.-R.; Shao, J.; Zhu, Q.-Y.; Dai, J. *Inorg. Chem.* **2021**, *60* (22), 17074–17082.

(88) Qi, F.; Sun, Z.; Fan, X.; Wang, Z.; Shi, Y.; Hu, G.; Li, F. *Adv. Energy Mater.* **2021**, *11* (20), 2100387.

(89) Rana, M.; Kim, J.; Peng, L.; Qiu, H.; Kaiser, R.; Ran, L.; Hossain, Md. S. A.; Luo, B.; Gentle, I.; Wang, L.; Knibbe, R.; Yamauchi, Y. *Nanoscale.* **2021**, *13* (25), 11086–11092.

(90) Li, Y.-A.; Zhao, C.-W.; Zhu, N.-X.; Liu, Q.-K.; Chen, G.-J.; Liu, J.-B.; Zhao, X.-D.; Ma, J.-P.; Zhang, S.; Dong, Y.-B. *Chem. Commun.* **2015**, *51* (100), 17672–17675.

(91) Li, B.; Lu, X.; Tian, Y.; Li, D. *Angew. Chem. Int. Ed.* **2022**, *61* (31), e202206755.

(92) Yang, C.; Chen, K.; Chen, M.; Hu, X.; Huan, S.-Y.; Chen, L.; Song, G.; Zhang, X.-B. *Anal. Chem.* **2019**, *91* (4), 2727–2733.

(93) Fang, S.-Y.; Gong, J.-L.; Tang, L.; Cao, W.-C.; Li, J.; Tan, Z.-K.; Wang, Y.-W.; Wang, W.-B. *ACS Appl. Mater. Interfaces.* **2022**, *14* (34), 38990–39003.

(94) Lim, J. H.; Goh, K.; Ng, D. Y. F.; Jiang, X.; Chuah, C. Y.; Chew, J. W.; Wang, R. *Chem. Eng. J.* **2022**, *450*, 137963.

(95) Lorusso, G.; Sharples, J. W.; Palacios, E.; Roubeau, O.; Brechin, E. K.; Sessoli, R.; Rossin, A.; Tuna, F.; McInnes, E. J. L.; Collison, D.; Evangelisti, M. *Adv. Mater.* **2013**, *25* (33), 4653–4656.

(96) Luo, H.-B.; Ren, Q.; Wang, P.; Zhang, J.; Wang, L.; Ren, X.-M. *ACS Appl. Mater. Interfaces.* **2019**, *11* (9), 9164–9171.

(97) Sadakiyo, M.; Kitagawa, H. *Dalton Trans.* **2021**, *50* (16), 5385–5397.

(98) Hu, J.-J.; Li, Y.-G.; Wen, H.-R.; Liu, S.-J.; Peng, Y.; Liu, C.-M. *Dalton Trans.* **2021**, *50* (41), 14714–14723.

(99) Zhang, Y.; Chen, H.; Pan, Y.; Zeng, X.; Jiang, X.; Long, Z.; Hou, X. *Chem. Commun.* **2019**, *55* (93), 13959–13962.

(100) Faust, T. *Nat. Chem.* **2016**, *8* (11), 990–991.

(101) Caro, J. *Chem. Ing. Tech.* **2018**, *90* (11), 1759–1768.

(102) Žák, Z.; Unfried, P.; Giester, G. *J. Alloys Compd.* **1994**, *205* (1–2), 235–242.

(103) Chen, Z.; Hanna, S. L.; Redfern, L. R.; Alezi, D.; Islamoglu, T.; Farha, O. K. *Coord. Chem. Rev.* **2019**, *386*, 32–49.

(104) Yuan, S.; Lu, W.; Chen, Y.-P.; Zhang, Q.; Liu, T.-F.; Feng, D.; Wang, X.; Qin, J.; Zhou, H.-C. *J. Am. Chem. Soc.* **2015**, 137 (9), 3177-3180

(105) Xie, L.-H.; Liu, X.-M.; He, T.; Li, J.-R. *Chem* **2018**, *4* (8), 1911–1927.

(106) Wang, H.; Dong, X.; Lin, J.; Teat, S. J.; Jensen, S.; Cure, J.; Alexandrov, E. V.; Xia, Q.; Tan, K.; Wang, Q.; Olson, D. H.; Proserpio, D. M.; Chabal, Y. J.; Thonhauser, T.; Sun, J.; Han, Y.; Li, J. *Nat. Commun.* **2018**, *9* (1), 1745.

(107) Gao, W.; Wu, H.; Leng, K.; Sun, Y.; Ma, S. *Angew. Chem. Int. Ed.* **2016**, *55* (18), 5472–5476.

(108) Copeman, C.; Bicalho, H. A.; Terban, M. W.; Troya, D.; Etter, M.; Frattini, P. L.; Wells, D. W.; Howarth, A. J. ChemRxiv. **2022**. Preprint

(109) Lammert, M.; Wharmby, M. T.; Smolders, S.; Bueken, B.; Lieb, A.; Lomachenko, K. A.; Vos, D. D.; Stock, N. *Chem. Commun.* **2015**, *51* (63), 12578–12581.

(110) Schoenecker, P. M.; Carson, C. G.; Jasuja, H.; Flemming, C. J. J.; Walton, K. S. *Ind. Eng. Chem. Res.* **2012**, *51* (18), 6513–6519.

(111) Katz, M. J.; Brown, Z. J.; Colón, Y. J.; Siu, P. W.; Scheidt, K. A.; Snurr, R. Q.; Hupp, J. T.; Farha, O. K. *Chem. Commun.* **2013**, *49* (82), 9449.

(112) Tahmouresilerd, B.; Moody, M.; Agogo, L.; F. Cozzolino, A. *Dalton Trans.* **2019**, *48* (19), 6445–6454.

(113) Hedrick, J. B. *J. Rare Earths.* **1997**, 61, 1-6

(114) Sridharan, V.; Menéndez, J. C. *Chem. Rev.* **2010**, *110* (6), 3805–3849.

(115) Ji, P.; Sawano, T.; Lin, Z.; Urban, A.; Boures, D.; Lin, W. *J. Am. Chem. Soc.* **2016**, *138* (45), 14860–14863.

(116) Jacobsen, J.; Ienco, A.; D'Amato, R.; Costantino, F.; Stock, N. *Dalton Trans.* **2020**, *49* (46), 16551–16586.

(117) Trickett, C. A.; Gagnon, K. J.; Lee, S.; Gándara, F.; Bürgi, H.-B.; Yaghi, O. M. *Angew. Chem. Int. Ed.* **2015**, *54* (38), 11162–11167.

(118) Hu, Z.; Peng, Y.; Kang, Z.; Qian, Y.; Zhao, D. *Inorg. Chem.* **2015**, *54* (10), 4862–4868.

(119) Biswas, S.; Zhang, J.; Li, Z.; Liu, Y.-Y.; Grzywa, M.; Sun, L.; Volkmer, D.; Van Der Voort, P. *Dalton Trans.* **2013**, *42* (13), 4730.

(120) Sava Gallis, D. F.; Vogel, D. J.; Vincent, G. A.; Rimsza, J. M.; Nenoff, T. M. *ACS Appl. Mater. Interfaces.* **2019**, *11* (46), 43270–43277.

(121) Sava Gallis, D. F.; Rohwer, L. E. S.; Rodriguez, M. A.; Barnhart-Dailey, M. C.; Butler, K. S.; Luk, T. S.; Timlin, J. A.; Chapman, K. W. *ACS Appl. Mater. Interfaces.* **2017**, *9* (27), 22268–22277.

(122) Ghasempour, H.; Habibi, B.; Zarekarizi, F.; Morsali, A.; Hu, M.-L. *Inorg. Chem.* **2022**, *61* (41), 16221–16227.

(123) Campanelli, M.; Del Giacco, T.; De Angelis, F.; Mosconi, E.; Taddei, M.; Marmottini, F.; D'Amato, R.; Costantino, F. *ACS Appl. Mater. Interfaces.* **2019**, *11* (48), 45031–45037.

(124) Son, F. A.; Atilgan, A.; Idrees, K. B.; Islamoglu, T.; Farha, O. K. *Inorg. Chem. Front.* **2020**, *7* (4), 984–990.

(125) Buragohain, A.; Biswas, S. *CrystEngComm.* **2016**, *18* (23), 4374–4381.

(126) Dalapati, R.; Sakthivel, B.; Dhakshinamoorthy, A.; Buragohain, A.; Bhunia, A.; Janiak, C.; Biswas, S. *CrystEngComm.* **2016**, *18* (40), 7855–7864.

(127) Waitschat, S.; Fröhlich, D.; Reinsch, H.; Terraschke, H.; Lomachenko, K. A.; Lamberti, C.; Kummer, H.; Helling, T.; Baumgartner, M.; Henninger, S.; Stock, N. *Dalton Trans.* **2018**, *47* (4), 1062–1070.

(128) D'Amato, R.; Donnadio, A.; Carta, M.; Sangregorio, C.; Tiana, D.; Vivani, R.; Taddei, M.; Costantino, F. *ACS Sustain. Chem. Eng.* **2019**, *7* (1), 394–402.

(129) Vahabi, A. H.; Norouzi, F.; Sheibani, E.; Rahimi-Nasrabadi, M. *Coord. Chem. Rev.* **2021**, *445*, 214050.

(130) Liu, C.; Eliseeva, S. V.; Luo, T.-Y.; Muldoon, P. F.; Petoud, S.; Rosi, N. L. *Chem. Sci.* **2018**, *9* (42), 8099–8102.

(131) Lammert, M.; Glißmann, C.; Reinsch, H.; Stock, N. *Cryst. Growth Des.* **2017**, *17* (3), 1125–1131.

(132) Martín, N. *Chem. Commun.* **2013**, *49* (63), 7025.

(133) Wudl, F.; Wobschall, D.; Hufnagel, E. J. *J. Am. Chem. Soc.* **1972**, *94* (2), 670–672.

(134) Narayan, T. C.; Miyakai, T.; Seki, S.; Dincă, M. *J. Am. Chem. Soc.* **2012**, *134* (31), 12932–12935.

(135) Su, J.; Yuan, S.; Wang, T.; Lollar, C. T.; Zuo, J.-L.; Zhang, J.; Zhou, H.-C. *Chem. Sci.* **2020**, *11* (7), 1918–1925.

(136) Xie, L. S.; Alexandrov, E. V.; Skorupskii, G.; Proserpio, D. M.; Dincă, M. *Chem. Sci.* **2019**, *10* (37), 8558–8565.

(137) Xie, L. S.; Dincă, M. *Isr. J. Chem.* **2018**, *58* (9–10), 1119–1122.

(138) Su, J.; Yuan, S.; Li, J.; Wang, H.; Ge, J.; Drake, H. F.; Leong, C. F.; Yu, F.; D'Alessandro, D. M.; Kurmoo, M.; Zuo, J.; Zhou, H. *Chem. – Eur. J.* **2021**, *27* (2), 622–627.

(139) Meilikhov, M.; Yusenko, K.; Fischer, R. A. *Dalton Trans.* **2010**, *39* (45), 10990.

(140) M. D'Alessandro, D. *Chem. Commun.* **2016**, *52* (58), 8957–8971.

(141) Halls, J. E.; Ahn, S. D.; Jiang, D.; Keenan, L. L.; Burrows, A. D.; Marken, F. *J. Electroanal. Chem.* **2013**, *689*, 168–175.

(142) Halls, J. E.; Cummings, C. Y.; Ellis, J.; Keenan, L. L.; Jiang, D.; Burrows, A. D.; Marken, F. *Mol. Cryst. Liq. Cryst.* **2012**, *554* (1), 12–21.

(143) Wang, C.; Xie, Z.; deKrafft, K. E.; Lin, W. *J. Am. Chem. Soc.* **2011**, *133* (34), 13445–13454.

(144) Halls, J. E.; Jiang, D.; Burrows, A. D.; Kulandainathan, M. A.; Marken, F. In *Electrochemistry*; Wadhawan, J. D., Compton, R. G., Eds.; Royal Society of Chemistry: Cambridge, 2013; Vol. 12, pp 187–210.

(145) Leong, C. F.; Faust, T. B.; Turner, P.; Usov, P. M.; Kepert, C. J.; Babarao, R.; Thornton, A. W.; D'Alessandro, D. M. *Dalton Trans.* **2013**, *42* (27), 9831.

(146) Mulfort, K. L.; Hupp, J. T. *J. Am. Chem. Soc.* **2007**, *129* (31), 9604–9605.

(147) Bae, Y.-S.; Hauser, B. G.; Farha, O. K.; Hupp, J. T.; Snurr, R. Q. *Microporous Mesoporous Mater.* **2011**, *141* (1–3), 231–235.

(148) Patwardhan, S.; Schatz, G. C. *J. Phys. Chem. C.* **2015**, *119* (43), 24238–24247.

(149) McGonigal, P. R.; Deria, P.; Hod, I.; Moghadam, P. Z.; Avestro, A.-J.; Horwitz, N. E.; Gibbs-Hall, I. C.; Blackburn, A. K.; Chen, D.; Botros, Y. Y.; Wasielewski, M. R.; Snurr, R. Q.; Hupp, J. T.; Farha, O. K.; Stoddart, J. F. *Proc. Natl. Acad. Sci.* **2015**, *112* (36), 11161–11168.

(150) Xu, Y.; Yin, X.-B.; He, X.-W.; Zhang, Y.-K. *Biosens. Bioelectron.* **2015**, *68*, 197–203.

(151) Jacobsen, J.; Achenbach, B.; Reinsch, H.; Smolders, S.; Lange, F.-D.; Friedrichs, G.; De Vos, D.; Stock, N. *Dalton Trans.* **2019**, *48* (23), 8433–8441.

(152) Karadeniz, B.; Howarth, A. J.; Stolar, T.; Islamoglu, T.; Dejanović, I.; Tireli, M.; Wasson, M. C.; Moon, S.-Y.; Farha, O. K.; Friščić, T.; Užarević, K. *ACS Sustain. Chem. Eng.* **2018**, *6* (11), 15841–15849.

(153) Jacobsen, J.; Wegner, L.; Reinsch, H.; Stock, N. *Dalton Trans.* **2020**, *49* (32), 11396–11402.

(154) Huskić, I.; Arhangelskis, M.; Friščić, T. *Green Chem.* **2020**, *22* (13), 4364–4375.

(155) Brekalo, I.; Deliz, D. E.; Kane, C. M.; Friščić, T.; Holman, K. T. *Molecules.* **2020**, *25* (3), 633.

(156) Li, M.; Dincă, M.; *J. Am. Chem. Soc.* **2011**, 133 (33), 12926-12929.

(157) Al-Kutubi, H.; Gascon, J.; Sudhölter, E. J. R.; Rassaei, L. *ChemElectroChem.* **2015**, *2* (4), 462–474.

(158) Xue, D.-X.; Cairns, A. J.; Belmabkhout, Y.; Wojtas, L.; Liu, Y.; Alkordi, M. H.; Eddaoudi, M. *J. Am. Chem. Soc.* **2013**, *135* (20), 7660–7667.

(159) Chen, Y.; Zhang, S.; Chen, F.; Cao, S.; Cai, Y.; Li, S.; Ma, H.; Ma, X.; Li, P.; Huang, X.; Wang, B. *J. Mater. Chem. A.* **2018**, *6* (2), 342–348.

(160) Schaate, A.; Roy, P.; Godt, A.; Lippke, J.; Waltz, F.; Wiebcke, M.; Behrens, P. *Chem. - Eur. J.* **2011**, *17* (24), 6643–6651.

(161) Vermoortele, F.; Bueken, B.; Le Bars, G.; Van de Voorde, B.; Vandichel, M.; Houthoofd, K.; Vimont, A.; Daturi, M.; Waroquier, M.; Van Speybroeck, V.; Kirschhock, C.; De Vos, D. E. *J. Am. Chem. Soc.* **2013**, *135* (31), 11465–11468.

(162) Vizuet, J. P.; Mortensen, M. L.; Lewis, A. L.; Wunch, M. A.; Firouzi, H. R.; McCandless, G. T.; Balkus, K. J. *J. Am. Chem. Soc.* **2021**, *143* (43), 17995–18000.

(163) Garibay, S. J.; Iordanov, I.; Islamoglu, T.; DeCoste, J. B.; Farha, O. K. *CrystEngComm.* **2018**, *20* (44), 7066–7070.

(164) Karagiaridi, O.; Bury, W.; Mondloch, J. E.; Hupp, J. T.; Farha, O. K. *Angew. Chem. Int. Ed.* **2014**, *53* (18), 4530–4540.

(165) Kim, M.; Cahill, J. F.; Fei, H.; Prather, K. A.; Cohen, S. M. *J. Am. Chem. Soc.* **2012**, *134* (43), 18082–18088.

(166) Burnett, B. J.; Barron, P. M.; Hu, C.; Choe, W. *J. Am. Chem. Soc.* **2011**, *133* (26), 9984–9987.

(167) Jeong, S.; Kim, D.; Song, X.; Choi, M.; Park, N.; Lah, M. S. *Chem. Mater.* **2013**, *25* (7), 1047–1054.

(168) Takaishi, S.; DeMarco, E. J.; Pellin, M. J.; Farha, O. K.; Hupp, J. T. *Chem. Sci.* **2013**, *4* (4), 1509–1513.

(169) Li, H.; Eddaoudi, M.; Groy, T. L.; Yaghi, O. M. *J. Am. Chem. Soc.* **1998**, *120* (33), 8571–8572.

(170) Li, H.; Eddaoudi, M.; O'Keeffe, M.; Yaghi, O. M. *Nature.* **1999**, *402* (6759), 276–279.

(171) Mondloch, J. E.; Karagiaridi, O.; Farha, O. K.; Hupp, J. T. *CrystEngComm.* **2013**, *15* (45), 9258–9264.

(172) Nelson, A. P.; Farha, O. K.; Mulfort, K. L.; Hupp, J. T. *J. Am. Chem. Soc.* **2009**, *131* (2), 458–460.

(173) Thommes, M.; Kaneko, K.; Neimark, A. V.; Olivier, J. P.; Rodriguez-Reinoso, F.; Rouquerol, J.; Sing, K. S. W. *Pure Appl. Chem.* **2015**, *87* (9–10), 1051–1069.

(174) Brunauer, S.; Emmett, P. H.; Teller, E. *J. Am. Chem. Soc.* **1938**, *60* (2), 309–319.

(175) Langmuir, I. *J. Am. Chem. Soc.* **1918**, *40* (9), 1361–1403.

(176) Olivier, J. P. *Carbon.* **1998**, *36* (10), 1469–1472.

(177) Kupgan, G.; Liyana-Arachchi, T. P.; Colina, C. M. *Langmuir.* **2017**, *33* (42), 11138–11145.

(178) Sunaoshi, T.; Kaji, K.; Orai, Y.; Schamp, C. T.; Voelkl, E. *Microsc. Microanal.* **2016**, *22* (S3), 604–605.

(179) Wade, L. G. 8. ed., internat. ed.; Always learning; Pearson: Boston, Mass. Munich, 2013.

(180) Wang, T. C.; Vermeulen, N. A.; Kim, I. S.; Martinson, A. B. F.; Stoddart, J. F.; Hupp, J. T.; Farha, O. K. *Nat. Protoc.* **2016**, *11* (1), 149–162.

(181) Wilschefski, S. C.; Baxter, M. R. *Clin. Biochem. Rev.* **2019**, *40* (3), 115–133.

(182) Mnculwane, H. T. *Analytica.* **2022**, *3* (1), 135–143.

(183) Elgrishi, N.; Rountree, K. J.; McCarthy, B. D.; Rountree, E. S.; Eisenhart, T. T.; Dempsey, J. L. *J. Chem. Educ.* **2018**, *95* (2), 197–206.

(184) Harris, D. C. 8th ed.; W.H. Freeman and Co: New York, 2010.

(185) Rojas-Buzo, S.; Concepción, P.; Olloqui-Sariego, J. L.; Moliner, M.; Corma, A. *ACS Appl. Mater. Interfaces.* **2021**, *13* (26), 31021–31030.

(186) Shen, C.-H.; Chuang, C.-H.; Gu, Y.-J.; Ho, W. H.; Song, Y.-D.; Chen, Y.-C.; Wang, Y.-C.; Kung, C.-W. *ACS Appl. Mater. Interfaces.* **2021**, *13* (14), 16418–16426.

(187) Ramachandran, R.; Xuan, W.; Zhao, C.; Leng, X.; Sun, D.; Luo, D.; Wang, F. *RSC Adv.* **2018**, *8* (7), 3462–3469.

(188) Bard, A. J.; Faulkner, L. R. 2nd ed.; Wiley: New York, 2001.

(189) Kulesza, P. J.; Cox, J. A. *Electroanalysis* **1998**, *10* (2), 73–80.

(190) Fuller, M. P.; Griffiths, P. R. *Anal. Chem.* **1978**, *50* (13), 1906–1910.

(191) Smith, G. F.; Getz, C. A. *Ind. Eng. Chem. Anal. Ed.* **1938**, *10* (4), 191–195.

(192) Sofen, S. R.; Cooper, S. R.; Raymond, K. N. *Inorg. Chem.* **1979**, *18* (6), 1611–1616.

(193) Yang, J.; Chen, L.; Li, W.; Chen, G.; Wang, L.; Zhao, S. *J. Colloid Interface Sci.* **2020**, *573*, 55–61.

(194) Laha, S.; Luthy, R. G. *Environ. Sci. Technol.* **1990**, *24* (3), 363–373.

(195) Chen, Y.; Chen, H.; Tian, H. *Chem. Commun.* **2015**, *51* (57), 11508–11511.

(196) Kühnel, R.-S.; Reber, D.; Battaglia, C. *J. Electrochem. Soc.* **2020**, *167* (7), 070544.

(197) Hansch, C.; Rockwell, S. D.; Jow, P. Y. C.; Leo, A.; Steller, E. E. *J. Med. Chem.* **1977**, *20* (2), 304–306.

(198) Lewis, D. E. Oxford University Press: New York, 2016.

(199) Hammett, L. P. *J. Am. Chem. Soc.* **1937**, *59* (1), 96–103.

(200) Su, J.; Yuan, S.; Wang, H.-Y.; Huang, L.; Ge, J.-Y.; Joseph, E.; Qin, J.; Cagin, T.; Zuo, J.-L.; Zhou, H.-C. *Nat. Commun.* **2017**, *8* (1), 2008.

(201) Saraci, F.; Quezada-Novoa, V.; Rafael Donnarumma, P.; J. Howarth, A. *Chem. Soc. Rev.* **2020**, *49* (22), 7949–7977.

(202) Wong, N. E.; Ramaswamy, P.; Lee, A. S.; Gelfand, B. S.; Bladek, K. J.; Taylor, J. M.; Spasyuk, D. M.; Shimizu, G. K. H. *J. Am. Chem. Soc.* **2017**, *139* (41), 14676–14683.

(203) Sun, Y.-Q.; Zhang, J.; Chen, Y.-M.; Yang, G.-Y. *Angew. Chem. Int. Ed.* **2005**, *44* (36), 5814–5817.

(204) Devic, T.; Serre, C.; Audebrand, N.; Marrot, J.; Férey, G. *J. Am. Chem. Soc.* **2005**, *127* (37), 12788–12789.

(205) Mitamura, Y.; Yorimitsu, H.; Oshima, K.; Osuka, A. *Chem. Sci.* **2011**, *2* (10), 2017.

(206) Cadiau, A.; Xie, L. S.; Kolobov, N.; Shkurenko, A.; Qureshi, M.; Tchalala, M. R.; Park, S. S.; Bavykina, A.; Eddaoudi, M.; Dincă, M.; Hendon, C. H.; Gascon, J. *Chem. Mater.* **2020**, *32* (1), 97–104.

(207) Castells-Gil, J.; Mañas-Valero, S.; Vitórica-Yrezábal, I. J.; Ananias, D.; Rocha, J.; Santiago, R.; Bromley, S. T.; Baldoví, J. J.; Coronado, E.; Souto, M.; Mínguez Espallargas, G. *Chem. – Eur. J.* **2019**, *25* (54), 12636–12643.

(208) Su, J.; Hu, T.-H.; Murase, R.; Wang, H.-Y.; D'Alessandro, D. M.; Kurmoo, M.; Zuo, J.-L. *Inorg. Chem.* **2019**, *58* (6), 3698–3706.

(209) D'Angelo, P.; Zitolo, A.; Migliorati, V.; Chillemi, G.; Duvail, M.; Vitorge, P.; Abadie, S.; Spezia, R. *Inorg. Chem.* **2011**, *50* (10), 4572–4579.

Appendix

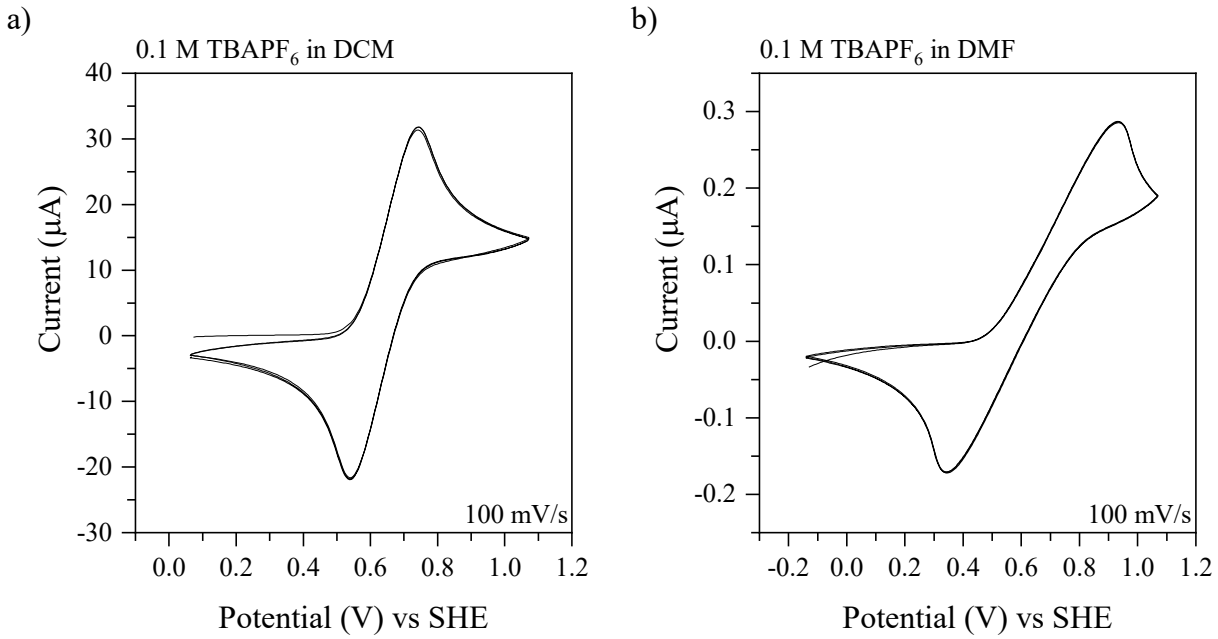

Figure S.2.1: Cyclic voltammogram of ferrocene in DCM (a) and DMF (b).

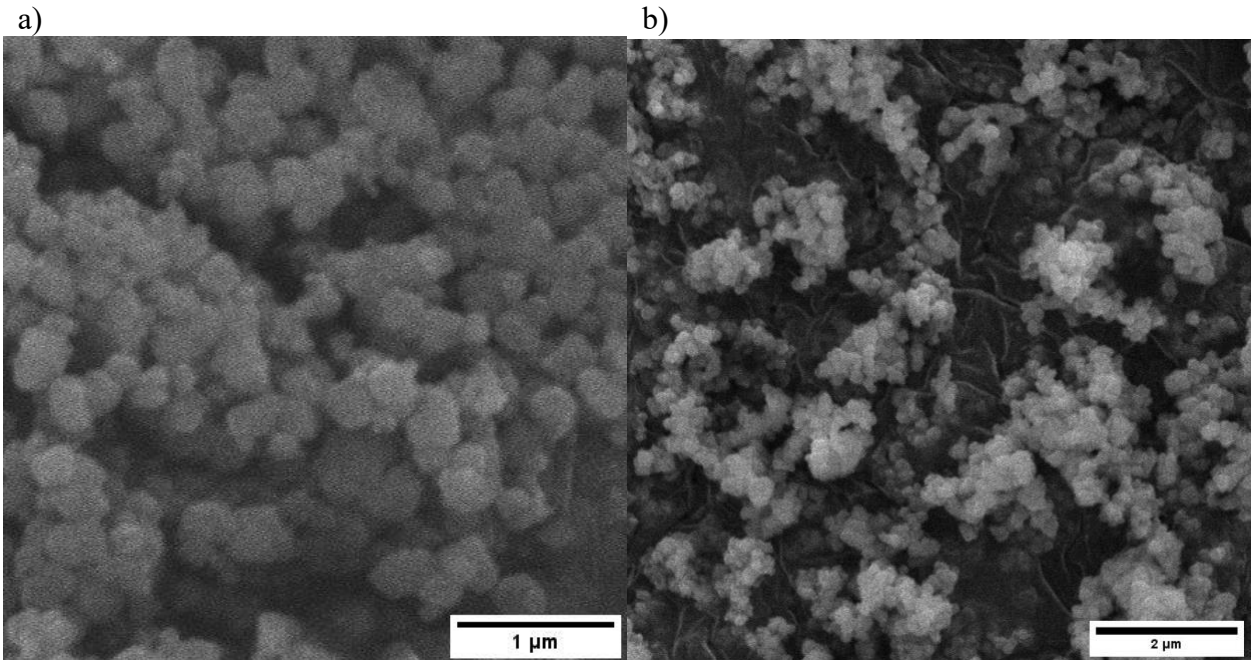

Figure S.2.2: SEM micrographs collected of Ce(IV)-UiO-66 (a) and Ce(IV)-UiO-66-Br (b).

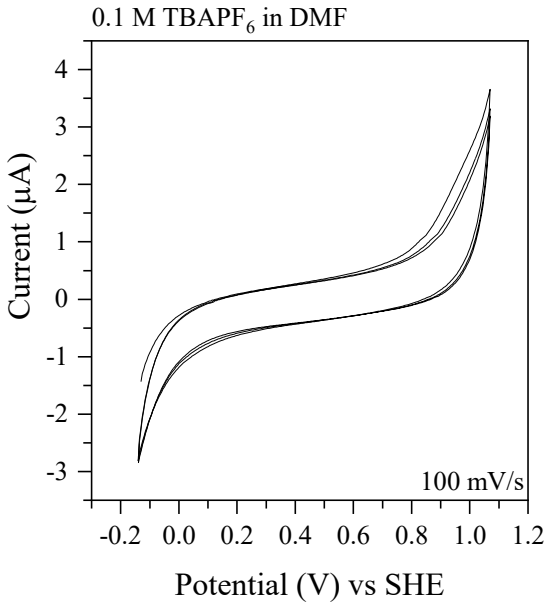

Figure S.2.3: Cyclic voltammogram of NH_2BDC collected in DMF solution.

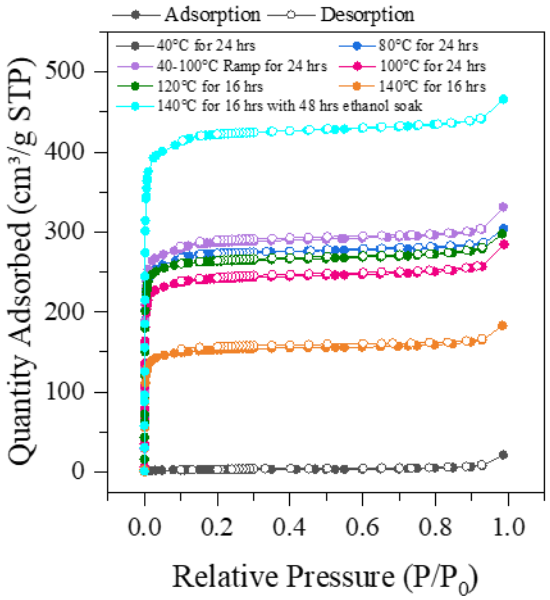

Figure S.2.4: N_2 gas adsorption-desorption isotherms determined from the vacuum activation experimentation of Ce(IV)-UiO-67-ByDC

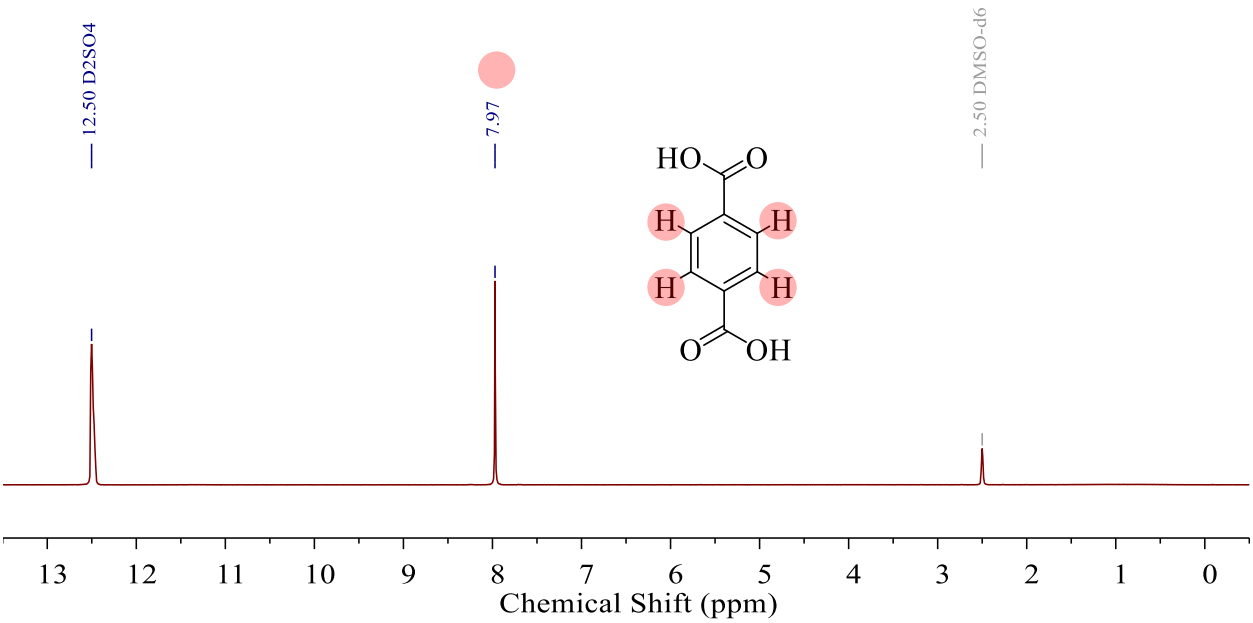

Figure S.2.5: ^{1}H NMR spectrum of BDC. Aromatic Hs appear at 7.97 ppm.

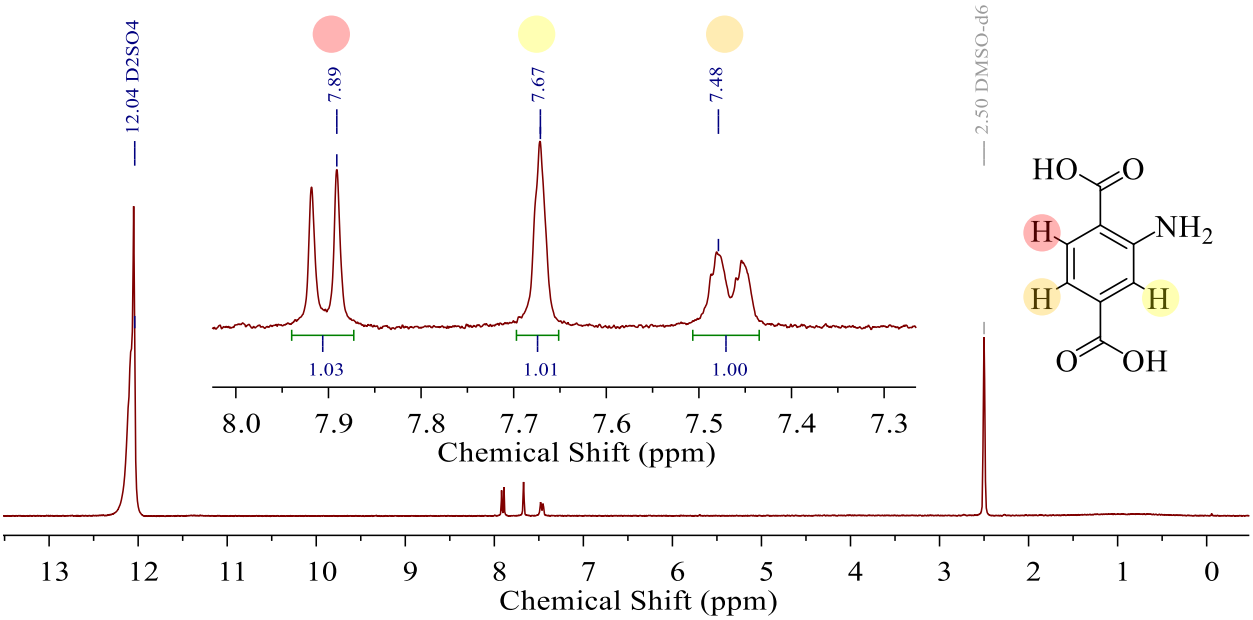

Figure S.2.6: ^{1}H NMR spectrum of NH_2BDC. Aromatic Hs appear at 7.97, 7.67, and 7.48 ppm.

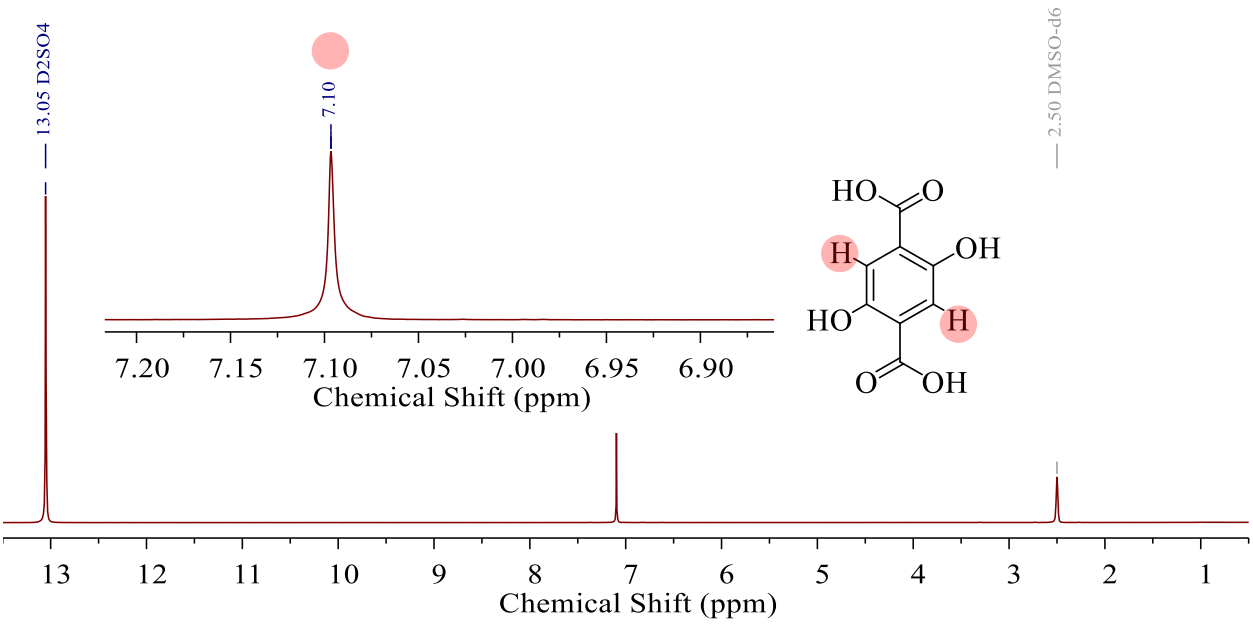

Figure S.2.7: ^{1}H NMR spectrum of DOBDC. Aromatic Hs appear at 7.10 ppm.

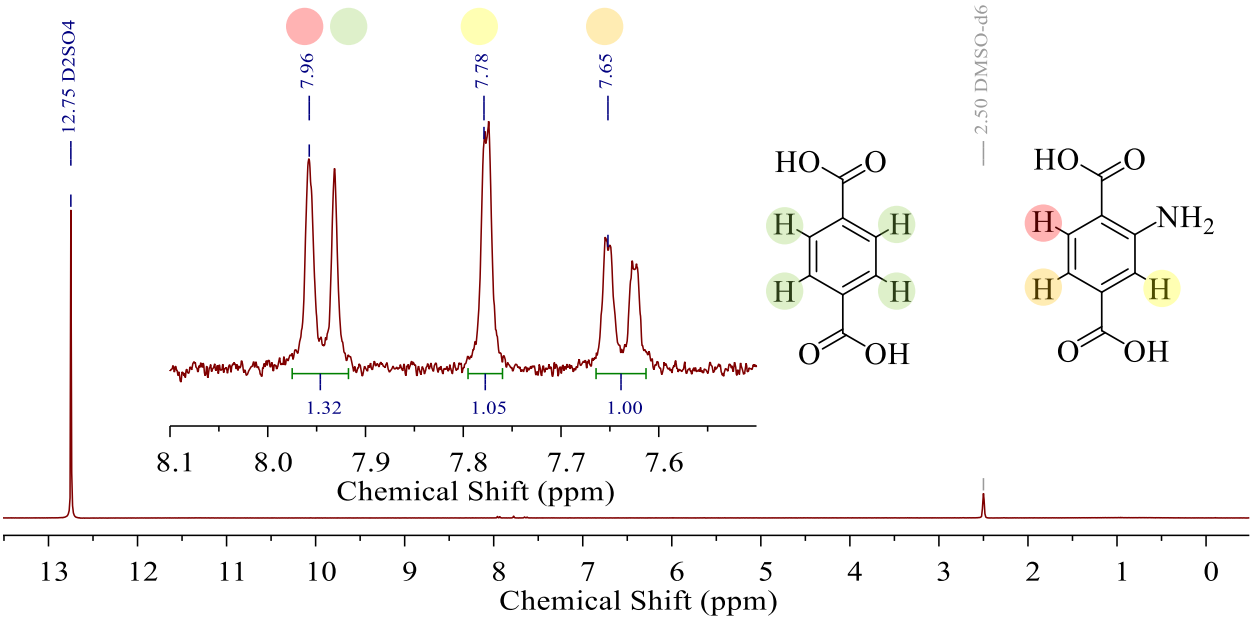

Figure S.2.8: ^{1}H NMR spectrum of Ce(IV)-UiO-66-NH_2 after two rounds of SALE. Quantization indicates 11 NH_2BDC: 1 BDC.

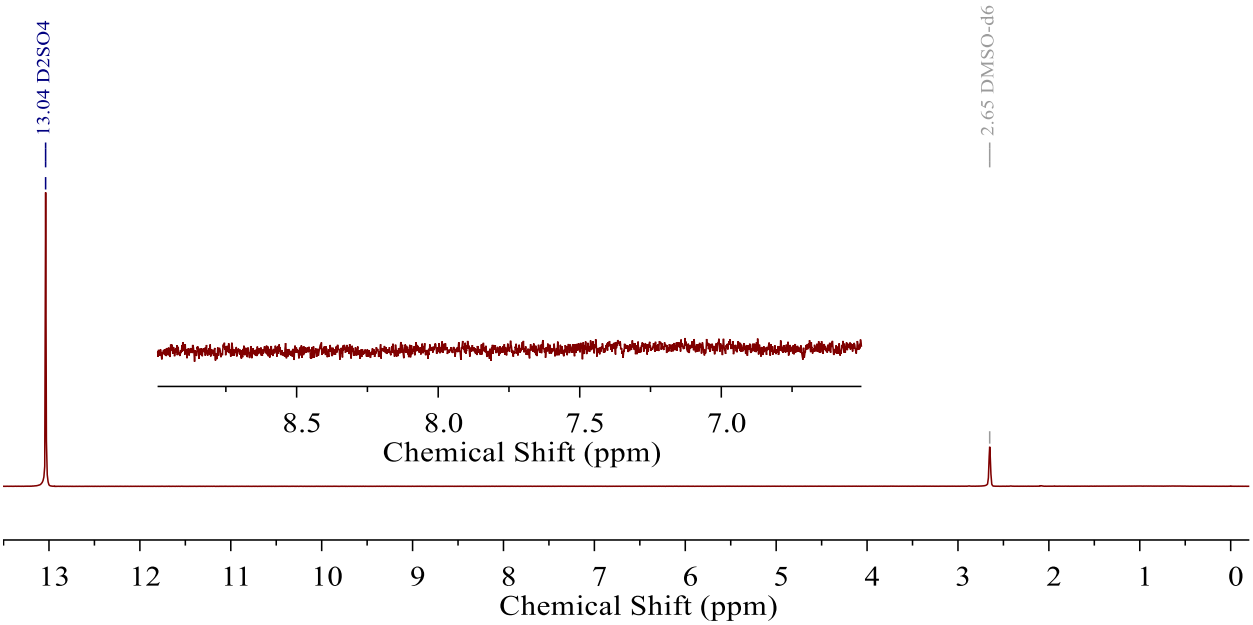

Figure S.2.9: ^{1}H NMR spectrum of Ce(IV)-UiO-66-F_4. The absence of peaks in the aromatic region from 6.5-9 ppm indicates only the F_4BDC linker is present.

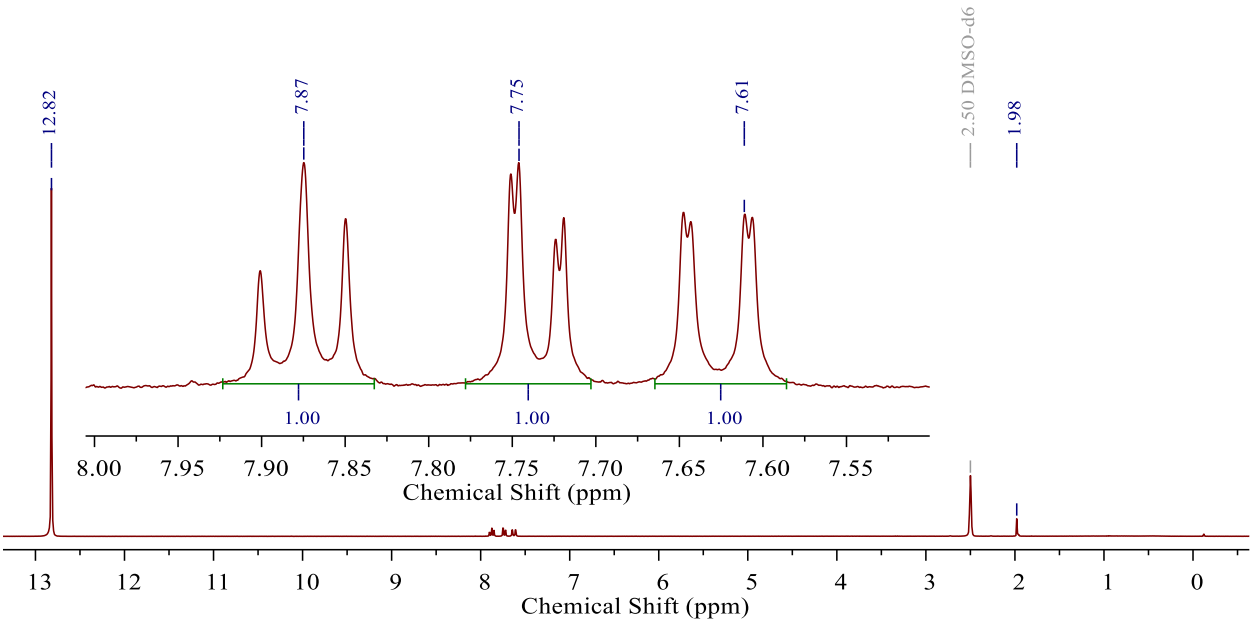

Figure S.2.10: ^{1}H NMR spectrum of FBDC.

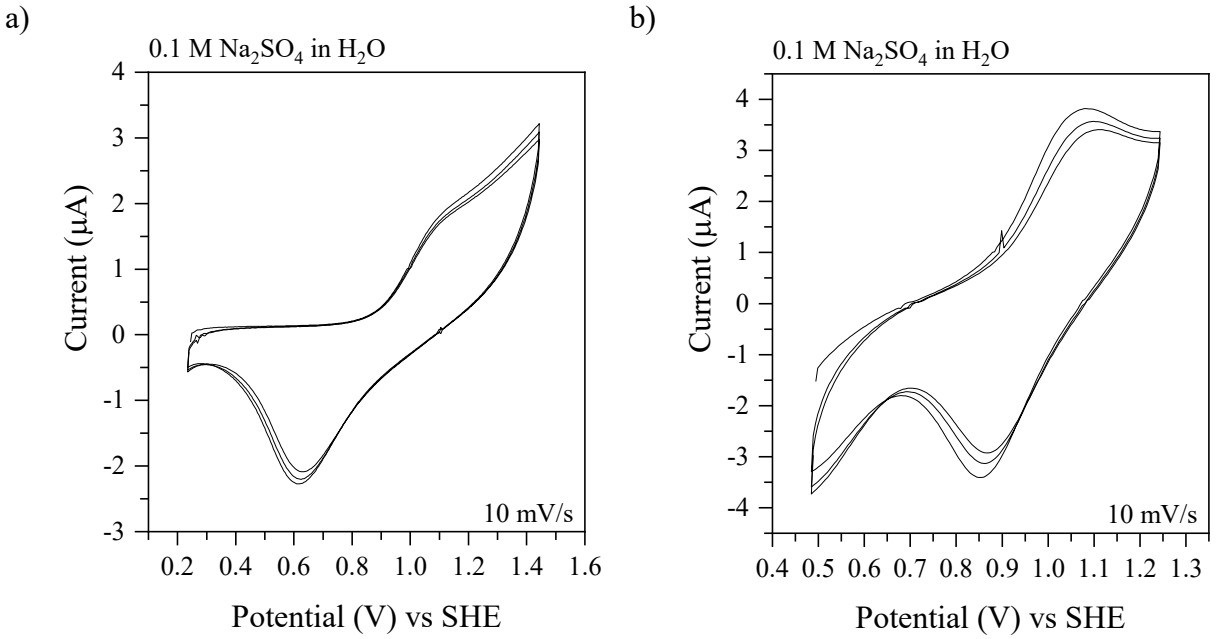

Figure S.2.11: Cyclic voltammograms collected of dropcast samples of Ce(IV)-UiO-66 (a) and Ce(IV)-UiO-66-Br (b) on FTO.

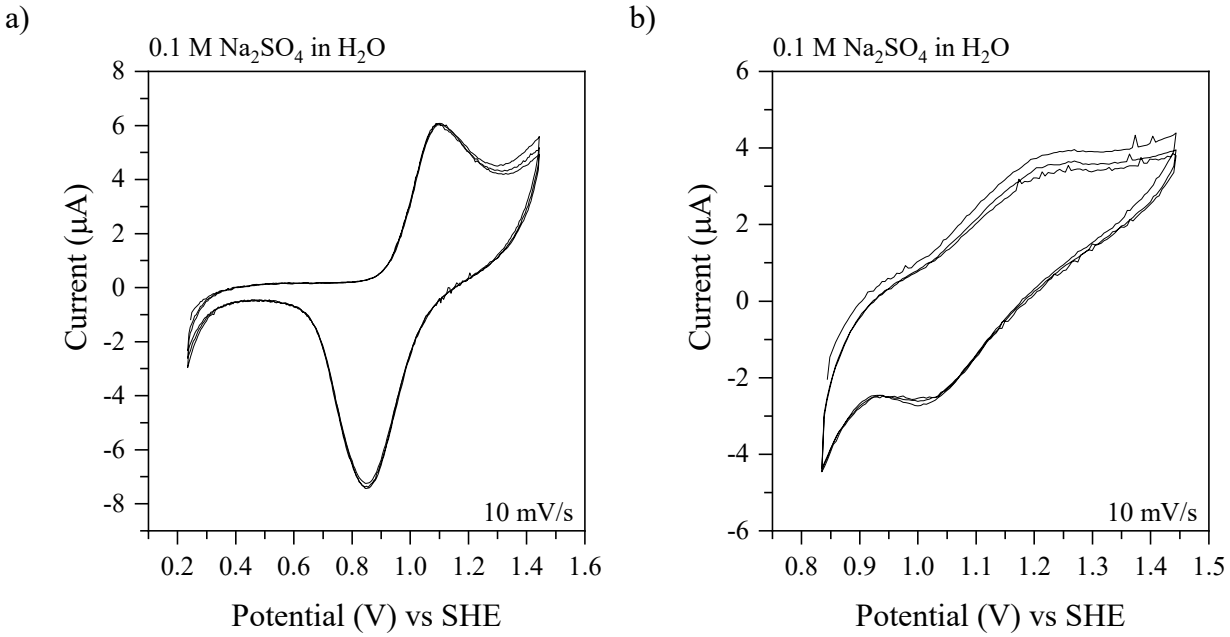

Figure S.2.12: Cyclic voltammograms collected of dropcast samples of Ce(IV)-UiO-66-F (a) and Ce(IV)-UiO-66-F_4 (b) on FTO.

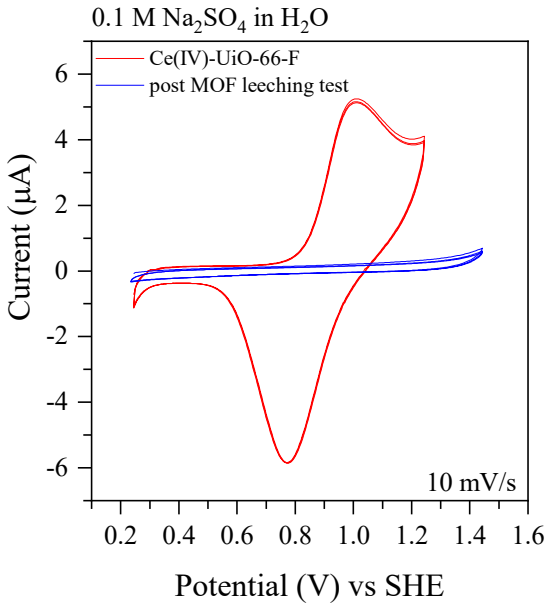

Figure S.2.13: Cyclic voltammogram collected of a dropcast sample of Ce(IV) UiO-66-F on FTO and of electrolyte solution after CV of Ce(IV)-UiO-66-F.

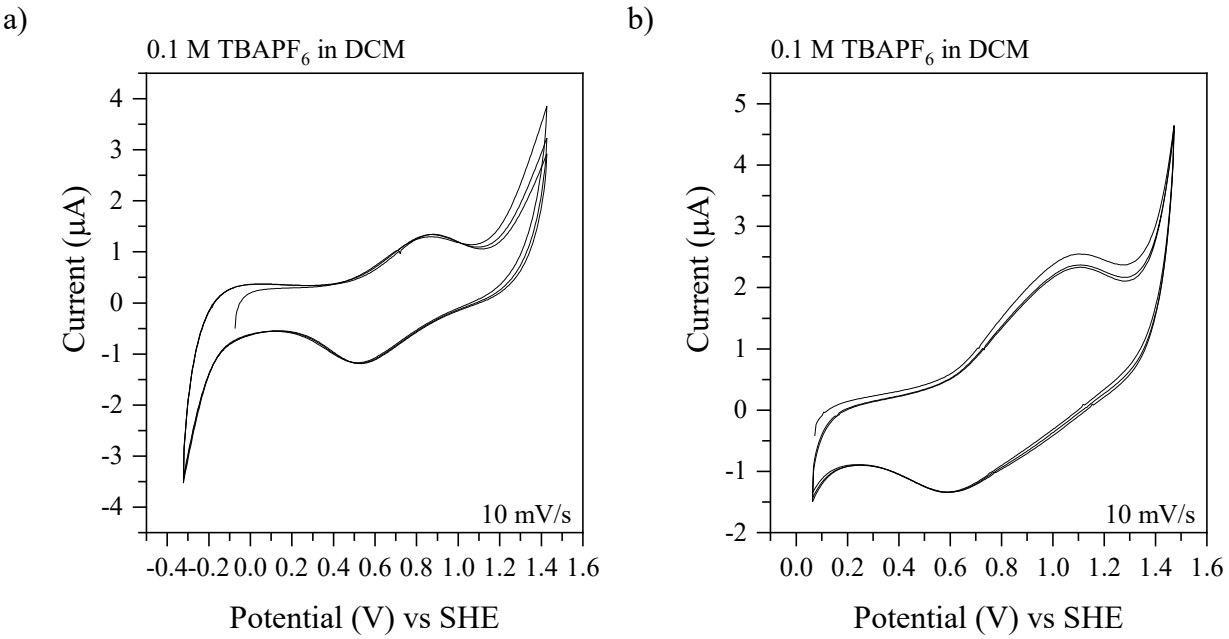

Figure S.2.14: Cyclic voltammograms collected of dropcast samples of Ce(IV)-UiO-66-NH_2 (a) and Ce(IV)-UiO-66-$(OH)_2$ (b) on FTO.

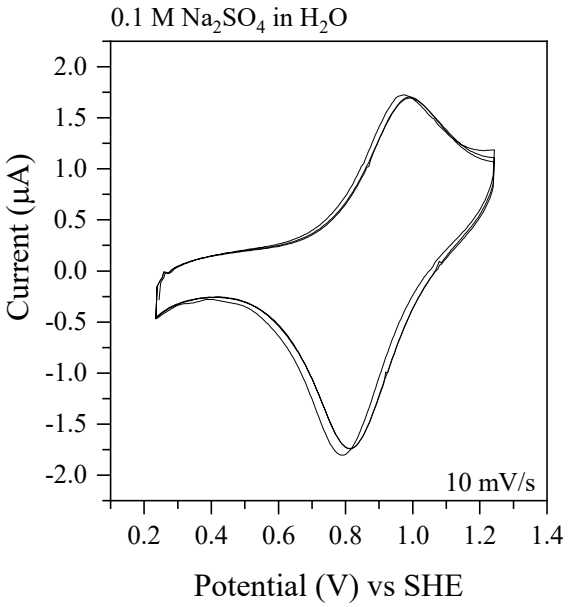

Figure S.2.15: Cyclic voltammogram collected of a dropcast sample of Ce(IV) UiO-67-BPyDC on FTO.

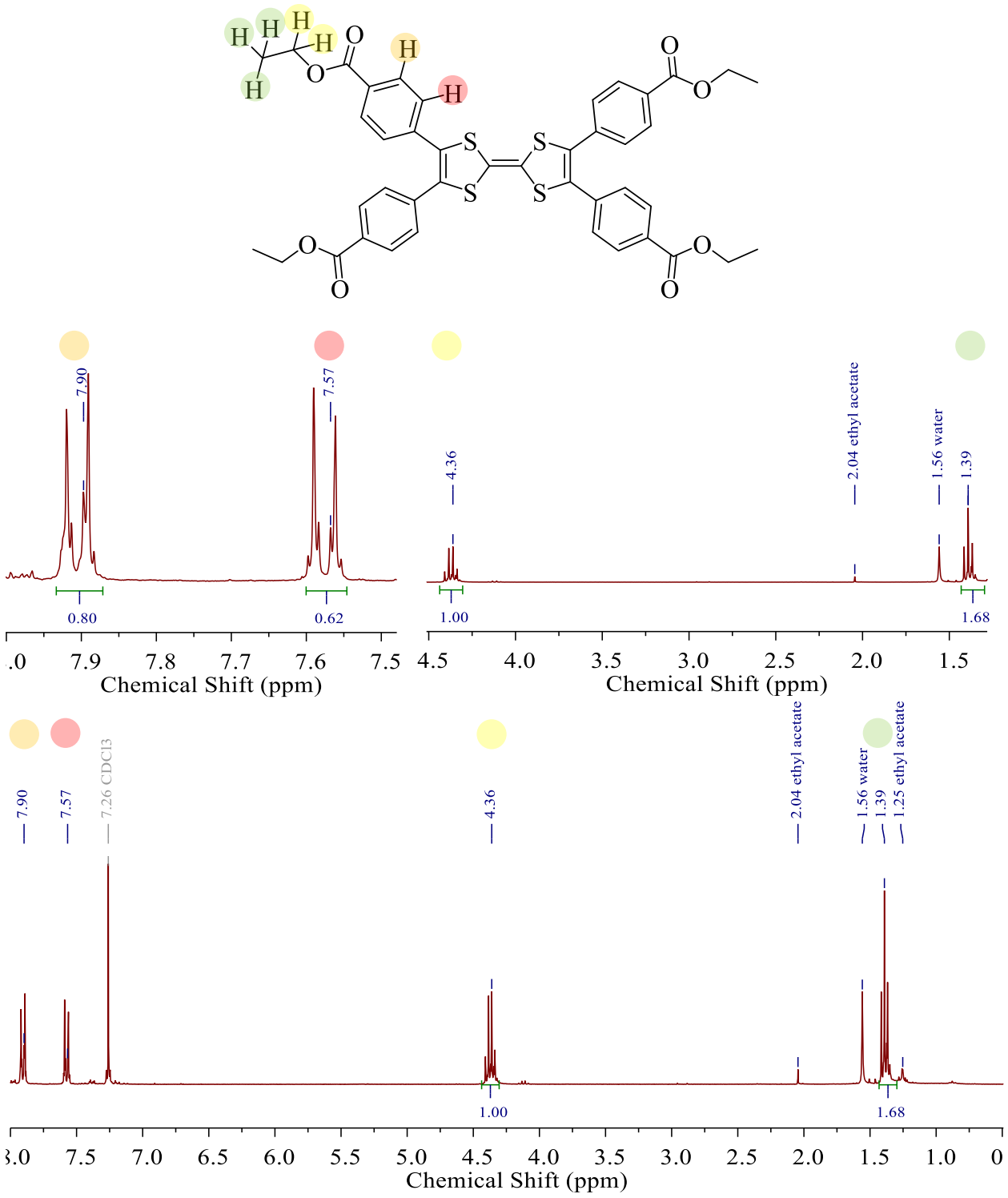

Figure S.3.1: ^{1}H NMR spectrum of tetrathiafulvalene-3,4,5,6-tetrakis(4-ethylbenzoate). Two types of hydrogens associated with the aromatic H on the benzene rings at 7.57 and 7.90 ppm, two type of proton from the ethyl ester group, the H bonded to the terminal C at 1.39 ppm, and

from the H bonded to the ester C at 4.36 ppm. Multiple contaminants from reaction solvents are present with ethyl acetate H at 1.25 and 2.04 ppm, and water H at 1.56 ppm.

a)

b)

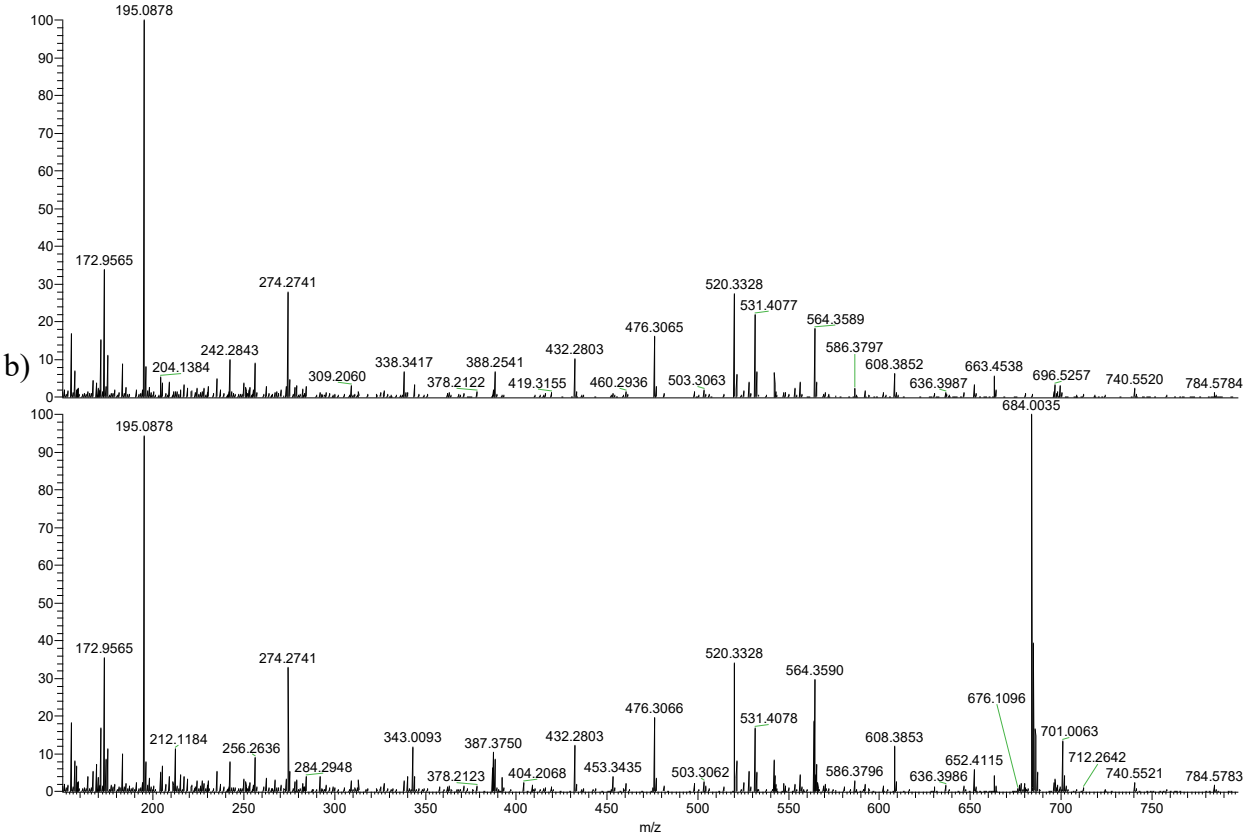

Figure S.3.2: Electrospray ionization mass spectrometry spectra for positive ions. The blank (a) compared to tetrathiafulvane-3,4,5,6-tetrakis(4-benzoic acid) (b). The peak at 684.0035 m/z in spectrum b is characteristic of TTFTBA.

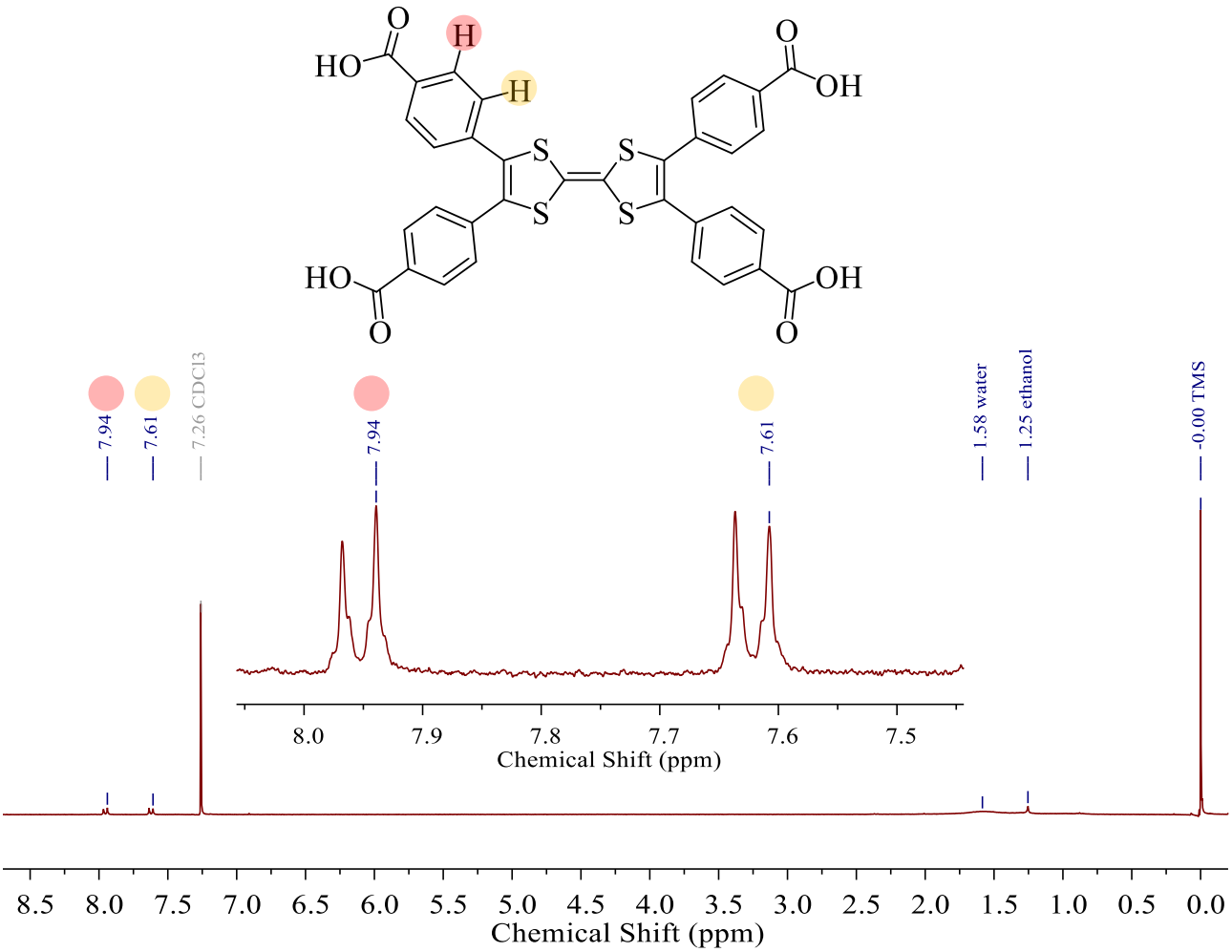

Figure S.3.3: ^{1}H NMR spectrum of tetrathiafulvalene-3,4,5,6-tetrakis(4-benzoic acid). Two types of hydrogens associated with the aromatic H on the benzene rings at ~7.61 and 7.94 ppm. Contaminants at 1.25 and 1.58 ppm correspond to water and ethanol respectively.

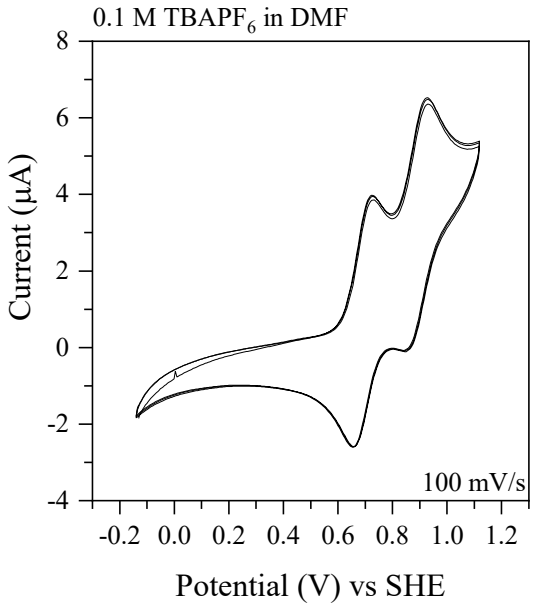

Figure S.3.4: Cyclic voltammogram collected of TTFTBA in DMF solution.